"Modelling and Control of Transients in Parabolic Trough Power Plants with Single-Phase Heat Transfer Fluids"

"Modellierung und Regelung transienten Verfahren in Parabolrinnenkraftwerke mit einphasigem Wärmeträgermedium"

Von der Fakultät für Maschinenwesen der Rheinisch-Westfälischen Technischen Hochschule Aachen zur Erlangung des akademischen Grades eines Doktors der Ingenieurwissenschaften genehmigte Dissertation

vorgelegt von

Kareem NOURELDIN

Berichter: Univ.-Prof. Dr.-Ing. Robert PITZ-PAAL
Prof. Alexander MITSOS, Ph.D.

Tag der mündlichen Prüfung: 03. Dezember, 2018

"I would not be concerned about a thinker even if he goes astray, because he would eventually revert to the judicious path. However, I would worry about someone who does not ponder even if he is on the right path, because he would be like a feather amid a wind storm."

–Muhammad Al-Ghazali

Abstract

Modelling and Control of Transients in Parabolic Trough Power Plants with Single-Phase Heat Transfer Fluids

by Kareem NOURELDIN

Optimizing solar field operation and control during transient processes, like passing clouds and solar field start-up, is key to improve the competitiveness of line-focus solar thermal power plants in comparison to other renewable energy technologies. Although simulation tools play a significant role in the design and optimization procedures, common solar field computational models cannot predict the behaviour of such a system exposed to high degrees of, both, temporal and spatial variability in the energy input. Some very detailed tools can only simulate parts of the system within acceptable time and computational power, and hence, they are not utilized as platforms to test new concepts under realistic operation conditions. On the other hand, tests in pilot or full-sized solar fields not only are too costly to prove a concept, but it is also nearly impossible to reproduce a transient test case with exactly the same disturbances to provide fair comparisons.

Thus, a novel transient solar field model, the Virtual Solar Field (VSF), is developed within the scope of this thesis. The model couples a static hydraulic flow model with a detailed dynamic loop model making use of the different time scales in the system. This results in an accurate and computationally efficient simulation tool for commercial power plants scale, such that, for example, 10 hours of Andasol-III solar field operation can be simulated in under 10 minutes. VSF has been validated against solar field operation data from Andasol-III as presented in the thesis. Also new control schemes that use direct normal irradiance (DNI) maps from nowcasting systems, as well as single loop valve control have been implemented and tested in VSF. A controller performance assessment scheme based on energy output and conversion efficiency has been developed to estimate the expected revenues of the solar field within the simulated time. This provides information to quantify the benefits of using one control strategy over another. The availability of the simulation tool also paves the way for developing model-predictive control strategies to optimize the field operation and production.

Kurzfassung

Modellierung und Regelung transienten Verfahren in Parabolrinnenkraftwerke mit einphasigem Wärmeträgermedium

von Kareem NOURELDIN

Eine Betriebs- und -Regelungsoptimierung in Parabolrinnenkraftwerken ist besonders für transiente Vorgänge wie zum Beispiel den Durchzug von Wolken oder Anfahrprozeduren notwendig, um die Wirtschaftlichkeit der Technologie in Vergleich zu anderen erneuerbaren Energietechnologien zu verbessern. Obwohl Simulationswerkzeuge eine wesentliche Rolle bei der Konzeption und Optimierung spielen, können verfügbare numerische Modelle für die Solarfelder das Verhalten solcher Systemen mit hoher zeitlicher und räumlicher Variabilität in der Energiequelle nicht abbilden. Einige sehr detailgetreue Tools können mit praktikablem Zeit- und Rechenaufwand jeweils nur Teile des gesamten Systems simulieren. Das macht solche Werkzeuge als Testplattform für neue Regelkonzepte unter realistischen Betriebsbedienung nicht brauchbar. Auf der anderen Seite sind reale Versuche in Pilot- oder gar kommerziellen Anlagen nicht nur sehr aufwändig, es ist auch faktisch unmöglich, gleiche Bedienungen für zwei verschiedene Konfigurationen herbeizuführen, welche für einen systematischen Vergleich erforderlich sind.

Davon ausgehend wird in der vorliegenden Doktorarbeit ein neues Solarfeldmodell, Virtual Solar Field (VSF), entwickelt. Das Modell koppelt ein statisches hydraulisches Modell mit einem detaillierten dynamischen thermischen Modell. Auf diese Weise lassen sich unterschiedliche Zeitskalen für diese beiden Teilprozesse abbilden, wodurch sowohl präzise als auch rechenzeiteffiziente Simulationen realisiert werden können. Beispielsweise kann das Programm den zehnstündigen Betrieb eines Andasol-III Solarfeldes in weniger als 10 Minuten durchrechnen. VSF wurde mit Betriebsdaten des Solarkraftwerks Andasol-III und mit anderen Simulationsmodellen validiert. In der Arbeit wurden dann neue Regelungskonzepte, die auf Solareinstrahlungskarten sowie Strangregelventilen basieren, implementiert und getestet. Ein auf die Anwendung zugeschnittenes Regler-Bewertungsschema wurde entwickelt, um das Verhalten verschiedener Regler vergleichen zu können. Die Verfügbarkeit eines solchen Simulationswerkzeugs ebnet den Weg zur Entwicklung neuartigen Regelstrategien die beispielsweise auf modellprädiktiver Regelung zur Optimierung des Feldbetriebs und Ertrag aufbauen.

Acknowledgements

I would like to express my sincere thanks to everyone who helped, supported and educated me to make this work possible. Without you this work would have not been there and I would not have been able to achieve this significant milestone in my life.

My sincere thanks go to my parents who offered unconditional and endless support since I first saw the light till this very moment.

I would like to thank my doctoral supervisor, Prof. Robert Pitz-Paal for the continuous support and very constructive advice and feedback that guaranteed an obstacle-free realization of this doctoral thesis. I also thank Prof. Alexander Mitsos for agreeing to co-supervise my thesis and for his support. My special gratitude goes to my project supervisor, Dr. Tobias Hirsch, whose positive and goal-oriented attitude has always been a great inspiration for me and certainly left a positive impact on me that I will always owe him. His solid experience in the field makes me confident that I always have a solid pillar that I can get sufficient support from.

I could not have made it without the support I got from my wife for easing the difficult and stressful times for our small family, especially with overcoming the challenges of living abroad. Her support and encouragement have always been enlightening for me and offered great motivation. I thank my daughter and son for the inspirational smiles they give me all the time. I would also like to thank my brother, parents-in-law and grandparents for their continuous motivation and prayers.

I would also like to thank my colleagues at the German Aerospace Centre (DLR) who offered a very welcoming and collaborative work environment in the office and during lunch and coffee breaks. I would like to specially thank Dr. Fabian Feldhoff, who offered very precious advice especially regarding control engineering. I would also like to thank Dr. Michael Wittmann and Heiko Schenk for sharing their experience in solar field modelling and components. Your input during our brainstorming sessions helped a lot. I would like to thank my office-mate Abdullah Khenissi for his advice and passion to CSP technologies. I would also like to thank Dr. Lars Amsbeck for being my mentor for the project and giving me his advice. My sincere gratitude goes also to my colleagues in the qualifications department of the DLR in Almería, Spain, namely Dr. Stefan Wilbert, Bijan Nouri and Pascal Kuhn who provided me with valuable irradiance maps that I used as basis for the applications in my doctoral thesis. They also established contact with power plant operators that helped in the validation, as well as with implementing solar field controllers.

I would also like to thank our partners from industry for the productive collaboration within this project. I would like to thank the colleagues in TSK-Flagsol GmbH, especially Mr. Hans Gielen for sharing his solid experience in programming solar field controllers. I would also like to thank the operation teams in Marquesado Solar and Africana Energía for sharing their experience with the operation of Andasol-III and La Africana solar power plants, respectively.

Last, but not least, I express my thanks to the valuable contribution of the work of the students who I had the honour to supervise. Ana Carolina Burghi helped me with data processing and model validation. She also initiated a study and implementation of fuzzy logic controllers. Tareq Farrah assisted me with running hundreds of simulations to optimize and tune the different controllers. I am also grateful for the financial support through the DLR/DAAD Scholarship program.

CONTENTS

LIST OF FIGURES

LIST OF TABLES

LIST OF ABBREVIATIONS

ARW	**A**nti-**r**eset **W**ind-up
BC	**B**oundary **C**ondition
CFL	**C**ourant-**F**riedrichs-**L**ewy
CO	**C**ontroller **O**utput
CSP	**C**oncentrating **S**olar **P**ower
DNI	**D**irect **N**ormal **I**rradiance
DSG	**D**irect **S**team **G**eneration
FB	**F**eed **B**ack
FF	**F**eed **F**orward
HTF	**H**eat **T**ransfer **F**luid
IAM	**I**ncident **A**ngle **M**odifier
LCoE	**L**evellized **C**ost **o**f **E**lectricity
LFC	**L**inear **F**resnel **C**ollectors
MS	**M**olten **S**alt
NC	**N**ow**c**asting
nRMSE	**n**ormalized **R**oot **M**ean **S**quare **E**rror
PB	**P**ower **B**lock
PI	**P**roportional-**I**ntegral
PP	**P**ower **P**lant
PT	**P**arabolic **T**rough
PTC	**P**arabolic **T**rough **C**ollectors
PV	**P**hoto**v**oltaic
PV	**P**rocess **V**ariable
RK	**R**unge-**K**utta
RMSE	**R**oot **M**ean **S**quare **E**rror
SCA	**S**olar **C**ollector **A**ssembly
SI	**I**nternational **S**ystem of units
SP	**S**et **P**oint
STE	**S**olar **T**hermal **E**nergy
TES	**T**hermal **E**nergy **S**torage
VSF	**V**irtual **S**olar **F**ield

LIST OF SYMBOLS

A_{in}	pipe inner cross-section area	m^2
A_{or}	orifice hole area	m^2
c_D	coefficient of discharge	[-]
D	diameter	m
D_{in}	pipe inner diameter	m
d_{or}	orifice hole diameter	m
f	Darcy friction factor	[-]
f_f	collector focus factor	[-]
G_{eff}	effective solar irradiance	$W\,m^{-2}$
h_f	frictional head loss	m
$K_{orifice}$	Orifice hydraulic resistance	$kg^{-1}\,m^{-1}$
K_p	Pipe hydraulic resistance	$kg^{-1}\,m^{-1}$
K_v	valve flow coefficient	$m^3\,h^{-1}$
L	length	m
$\dot{m}$	mass flow rate	$kg\,s^{-1}$
p	pressure	Pa or bar
p_δ	pump differential pressure	Pa or bar
$\dot{q}_{conv}$	convective heat transfer rate per unit length	$W\,m^{-1}$
S_f	fluid energy source term	$W\,m^{-1}$
S_w	wall energy source term	$W\,m^{-1}$
t	time	s
T_f	bulk fluid temperature	$°C$
T_w	bulk pipe wall temperature	$°C$
t_w	pipe wall thickness	m
$\hat{u}$	internal energy	J
$\dot{V}$	volume flow rate	$m^3\,s^{-1}$
v_f	fluid velocity	$m\,s^{-1}$
w_{ap}	collector aperture width	m
x	spatial coordinate	m

Dimensionless parameters

Gr	Grashof number
Nu	Nusselt number
Pr	Prandtl number
Ra	Rayleigh number
Re	Reynolds number

Greek symbols

α_f	coefficient of convective heat transfer	$W\,m^{-2}\,K^{-1}$
β	orifice diameter ratio	[-]
β_v	volumetric coefficient of thermal expansion	K^{-1}

ε	emissivity	[-]
ϵ	surface roughness	m
ϵ_{exp}	expandability factor	[-]
φ	sun zenith angle	rad
λ	coefficient of thermal conduction	$W\,m^{-1}\,K^{-1}$
μ	dynamic viscosity	$Pa\,s$
ν	kinematic viscosity	$m^2\,s^{-1}$
ρ_f	fluid density	$kg\,m^{-3}$

Physical constants

Gravitational acceleration	$g = 9.81\ m\,s^{-2}$
Stefan-Boltzmann constant	$\sigma = 5.6703 \times 10^{-8}\ W\,m^{-2}\,K^{-4}$

For a better world for my family and everyone else

1 INTRODUCTION

With few exceptions, the deployment of renewable energies is considered a global goal to reduce CO_2 emissions and to supply sustainable energy. The Paris climate change agreement sets goals to limit the global temperature rise of the 21st century well below 2 °C above the preindustrial time levels. This shall be achieved by reducing greenhouse gas emissions within different sectors through various measures. Renewables play a significant role by contributing to more than 30 % of the desired CO_2 reduction by 2060 [90]. To fulfill such goal, we should rely on developed renewable energy technologies such as solar and wind power plants [50].

In the solar energy sector for electricity production, photovoltaic (PV) technologies showed significant reduction in installation and operation costs, that the levellized cost of electricity (LCoE) averaged at less than 50 €/MWh in 2016 with a net globally installed capacity of 300 GW. However, PV, and also wind power, are highly intermittent sources of electricity that strongly depend on the instantaneous solar irradiance, or wind speed, respectively. The prices increase drastically if a separate electric energy storage system is added, rendering the system neither economically nor technologically feasible [50]. As the portions of such electricity sources increase in the energy system, extremely high ramp-up rates are needed from back-up power plants to compensate for the missing power that intermittent renewables fail to deliver [19]. Problems with flexibility and dispatchability also become more prominent [38].

On the other hand, introducing concentrating solar power (CSP), also known as solar thermal energy (STE), in the energy mix offers a feasible solution for such problems [4]. In CSP, solar irradiation is collected and concentrated by mirrors on absorber surfaces that transform it to thermal energy or heat. The heat is fed into power cycles that transform it to mechanical work, which in turn rotates a generator to produce electricity. Despite the higher cost of electricity produced by CSP as compared to PV, with recent CSP projects under construction for an LCoE of 120 €/MWh and the most recent tender for the world's largest CSP project in Dubai for 73 €/MWh [2], CSP remains economically attractive. This is due to the cost-effective energy storage in the form of thermal energy, which enables the production of dispatchable electric power during different periods of the day [69]. This adds a significant value of the technology as the share of intermittent renewable energy sources is increased in the the electricity generation mix [23]. For example, the 50 MW CSP plant in Bokpoort in South Africa is reported to operate for 161 h continuously in March 2016 [78]. In addition, CSP has a very good potential to contribute to the sustainable development goals (SDG) set by the United Nations General Assembly in 2015 [14]. The SDGs

provide a framework for international efforts to achieve both human development and climate objectives, such as providing employment and sustainable and affordable energy for everyone, as well as providing appropriate nutrition and clean water. Furthermore, CSP has the lead in process heat applications to economically and environmentally-friendly supply heat to industrial processes [49].

With the global installed capacity of only 4.8 *GW* of CSP, which is nearly two orders of magnitude lower than PV [72], there exists a tremendous margin for cost reduction by improving the production process through economies of scale and by increasing the system efficiency [68]. Fostering the system efficiency involves not only improving component efficiencies, but also maximizing the collected solar energy through optimizing the power plant operation where solar field simulation tools could play an important role.

1.1 PARABOLIC TROUGH POWER PLANTS

The majority of commercially-operated CSP plants are based on parabolic trough collectors (PTC), which is a line-focus technology. Thus, optimizing their operation will have a significant impact on the potential of CSP. In addition, advancements in components and materials promise good returns when their operational challenges are addressed. In principle, line-focus CSP plants concentrate the incident solar irradiation on linear receiver tubes laying in the focus line of parabolic trough-shaped mirrors. The concentration can also be achieved by linear Fresnel collectors (LFC). A heat transfer fluid (HTF) is heated as it flows through the receiver tubes in the solar field to collect the thermal energy from the heated tubes due to the concentrated rays. The hot HTF then flows through heat exchangers to boil water and the generated steam is used to operate a turbine connected to an electric generator. Some power plants also include thermal energy storage (TES) systems to enable economical uninterrupted operation to be able to economically supply electricity when there is no solar irradiation for some time. In most of those systems, MS is used as the storage medium in one or two tanks.

Figure 1.1 shows some components of the solar field in parabolic trough (PT) power plants (PP), where the main components of a solar collector assembly (SCA) are illustrated in Figure 1.1a. An SCA is formed of connected elements attached to a single drive that manipulates their tracking angle. The SCA follows the sun on a single axis, such that parallel rays incident on the whole area of the parabolic-shaped mirrors reflect on the focal line, where the absorber tubes are located. Multiple SCAs are usually connected in series using flexible joints to form a collector loop. The joints serve the purpose so that the adjacent SCAs are able to have different tracking angles, which allow for more versatile solar input options. Valves are installed at the loop inlet to control the flow or for maintenance.

In full-scale PT power plants, multiple loops are connected in parallel to runner piping to form the solar field as shown in Figure 1.1b. Also multiple solar fields, namely subfields, can be connected in parallel to a power block (PB) using header piping. The PB includes

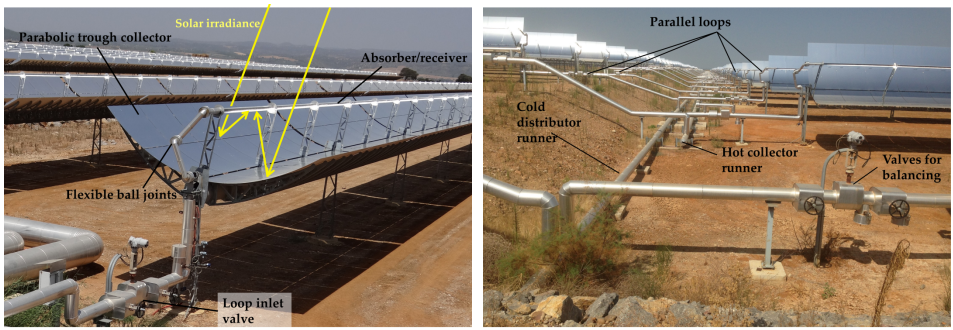

(a) Collector and optical principle. **(b)** Parallel loops and runners.

Figure 1.1. Components in PTC solar field.

the main flow pumps that drive the flow in the solar field. As the header lengths to the different subfields can vary, as well as the number of loops in each subfield, throttling valves are installed in the headers to compensate for the different pressure drops. Loop valves are also used to balance the flow in the single loops to compensate the pressure drop in the long runners and headers.

Heat transfer fluids

The HTF could be a single-phase fluid that retains its physical state, like oil or molten salt (MS), or it could evaporate, like in direct steam generation (DSG) systems. The most common HTF in PT solar fields is thermal oil based on an eutectic mixture of Biphenyl and Diphenyl-oxide [22]. There is also growing interest in using MS as the HTF in PTC due to its benefits [85]. Firstly, MS can be heated to higher temperatures than thermal oils, thus higher thermodynamic efficiencies of the work cycle of the steam turbine could be achieved. Secondly, MS will be directly used as the storage media without the need for heat exchangers at the storage tanks. However, MS needs to be maintained above its melting point, approximately 200 °C, at all times, which represents a challenge in solar field day and night operation. Alternatively, novel silicon-based oils are very promising as more environment friendly and efficient substitute to thermal oils [40]. Appendix A shows the temperature-dependent physical properties of the HTF used within this thesis, namely thermal oils and MS.

DSG systems include evaporation of water and superheating the steam within the absorber tubes [24]. The steam generated at the solar field is directly used to operate the turbine. Generally, the simulation of such systems needs special models that account for two-phase flow and are out of the scope of this thesis.

1.2 TRANSIENT PROCESSES AND CONTROL

PTCs focus only the direct normal irradiance (DNI) from the solar rays on the absorber tubes, as DNI is the only part that falls normal to the mirror surfaces and, thus, could be reflected in the correct direction. Clearly CSP plants are subject to strong transient conditions as the source of energy to the system cannot be manipulated at will. Different types of cloud passages cause disturbances in the energy source varying in, both, amplitude and frequency. A lot of efforts to categorize the temporal disturbances in the solar irradiance have been made, for example in [25, 55, 56]. The methods depend mainly on assessing how far the current DNI value is from the expected clear-sky value in the current instant, as well as the duration and amplitude of the disturbance. Another source of transient conditions in a solar field is start-up operations as the shadow of the collector loops on one another gradually vanish causing a progressive increase in the energy input to the field [27]. Similar behaviour is also experienced during shut-down as the solar irradiance gradually declines.

Challenges with SF operation and control

According to personal communications with solar field control experts [29], a perfect solar field controller shall be able to manipulate the flow rate in the solar field perfectly to maintain constant temperature while avoiding any defocussing instances. However, due to the large stretch of parabolic trough power plants, the spatial variability of DNI in the field is significant and inflicts substantial challenges to the controllers. State of the art solar field controllers do not have much information about the spatial distribution of the irradiance, as the information is provided by only a handful of sensors at different points in the field. For that, spatially-resolved DNI maps from a grid of upward-facing cloud cameras, or downward-facing shadow cameras [75] are used as input to, both the field simulation model and the controllers.

As for novel HTFs, the use of MS is also challenging in terms of solar field control. The combination of critical temperature limitations (upper and lower operating temperatures) and the potentially larger size of the solar fields require detailed understanding of the solar field behaviour [85]. In particular, control during transient processes, such as start-up, cool down, and passing clouds, imposes big challenges [27].

To keep the field operation controllable and stable under all conditions, the operator has to find the best trajectory for field mass flow, temperature set-points, and defocusing of collectors. In order to develop appropriate control schemes, a better understanding of the behaviour of the solar field under transient conditions will help reduce defocusing instances, improve field control, and, hence, increase the energy yield and confidence in this quickly developing technology. Therefore, comprehensive numerical models are required to study the hydraulic and thermal interactions in the field.

1.3 DYNAMIC SIMULATION TOOLS

Simulation software packages have helped engineers and scientists to develop, optimize and control CSP plants. In addition, reliable simulation tools reduce the costs and time during designing and testing phases when compared to preparing experimental test benches and building prototypes. Numerous simulation tools for line-focus solar thermal power plants are used throughout all the designing, financing, building, and commissioning phases of the plant.

Most transient models available in literature either investigate a single loop, like the model in [93], or consider a single representative loop to model the whole field as in [35]. On the other hand, performance and annual yield models, like the model in [27], assume equal mass flow distribution among the loops. Consequently, realistic mass flow distributions in the collector loops arranged in parallel cannot be modelled. A model developed in [30] calculates the flow distribution; however, it is not fully coupled with the thermal condition of the field. Commercial simulation software, like ISAAC Dynamics [79], can simulate multiple loops under transient conditions. However, there are limitations regarding computational times rendering it not possible to model full-scale commercial CSP power plants.

As for flow distribution in parallel pipes, a modelling strategy described in [1] outlines a method for computing loop valve positions in order to accurately balance the flow in the loops of a subfield. Yet, full coupling of the thermal and hydraulic states is not described, for example the effect of loop temperatures on the flow distribution without changing valve positions. Another model for the flow distribution in non-concentrating solar fields with flat plate collectors is recently published in [7]. The model considers the field at a much smaller scale than in CSP plants with lower energy densities and flow rates and couples it with a static thermal model. Transient models for gas pipe network flows like in [31, 32] consider isothermal flow along the pipes, which does not apply for CSP plants.

Under these circumstances, there is a lack in the availability of a simulation tool being able to model full-sized solar fields under realistic weather conditions to study solar field controller design and serve to optimize control strategies. In addition, the effects of degradation of different components, such as absorber tubes, on the over-all power plant energy yield can be studied.

1.4 MOTIVATION AND APPROACH

The main motivation of this thesis is to develop a simulation tool that enables solar field developers and operators to alleviate the performance during transient processes. Hence, a new transient simulation tool for a whole solar field was developed as part of the research in this thesis to fill-in the need. The tool is named Virtual Solar Field (VSF) and is meant to provide a virtual replica of the complete solar field. The simulation tool can mimic the plant

layout with any irregularities in the construction, such as different number of loops in the subfields and their orientation. In addition, the VSF is able to reproduce the plant response to realistic DNI conditions with, both temporal and spatial, variabilities. The tool also considers any diversity in the field operation conditions, such as different mirror cleanliness, loops shut-down for maintenance or broken glass in absorber pipes. In particular, the tool determines the flow distribution in the parallel loops and subfields depending on the setting of the loop and subfield valves and on the thermal condition in the absorber pipes. Also the control parameters in the simulation model match the parameters in real solar field operation. For example, the flow is controlled by manipulating the pump set-point and the focus of the SCAs is controlled by local built-in controllers. Furthermore, the DNI input to the controllers is passed from weather station measurements at the locations specified in the solar field or more advanced DNI maps. Above all is the computation speed, as the model is capable of computing a commercial-scale solar field, such as Andasol-III, in just about 1 % of real-time.

The main aspect of this thesis is to develop a numerical simulation scheme that accurately represents the dynamic behaviour of solar fields that is also computationally efficient. Then the implemented tool is used to investigate the means by which the availability of such a tool can help in improving the solar field controller performance in different transient situations. A performance assessment scheme based on the estimation of the economic yield is developed. With this method, different control and operation strategies can be fairly compared.

Secondly, state-of-the-art solar field control has been studied and a basic controller, based on that, is implemented and used as benchmark to compare some proposed advancements. An automatic controller is devised to overcome some difficulties faced by the basic controller during transient conditions, which usually cause the operator of a state-of-the-art solar field to manually intervene to avoid excessive losses. Lastly, new control concepts using DNI maps and forecasts from nowcasting systems have been formulated. In the same way, a simple loop valve control concept has been added to manipulate the flow rate in the single loops in response to localized transients.

It follows that by having access to all physical quantities in the simulated solar field, the economic benefit of using the described advancements in the controllers or any further improvements can be reasonably measured and quantified. A performance assessment method is devised enabling the user to compare the yield using different control approaches in a fully controlled and reproducible environment. The assessment scheme is based on assigning economic penalties for control actions deviating from the design point in the solar field. This provides comprehensive quantification of the benefit or loss of adding any advanced features to the solar field. It also enables the estimation of the economic feasibility of new investments.

Methodology

The Virtual Solar Field model consists of a hydraulic part and a thermal part that are coupled to account for the effect of the thermal condition of the field on the flow distribution among the parallel loops. The model is specifically designed for large line-focus solar fields offering a high degree of flexibility in terms of layout, condition of the mirrors, and spatially resolved DNI. The model has been validated using other simulation tools, as well as experimental and plant data, and the results show very good agreement. Besides, different control concepts are added-on to operate the virtual solar field.

In Chapter 2 below, the VSF tool is elaborated and the two parts constituting the model are described, as well as all the model assumptions and limitations. In this chapter, the categorization of the incident DNI maps is discussed. In Chapter 3, numerous validation test cases performed throughout the development phases of the tool, are described. At first, the validation is performed on the single model components using other validated tools. Then, the validation of the whole model against power plant operation data is shown in Section 3.3. After that, a control algorithm used to operate the solar field is outlined in Chapter 4, where the plant performance assessment scheme, as well as some difficulties the controllers face, is described. This is then followed in Chapter 5 by more applications of the VSF to develop new example control concepts and study their performance in comparison to the benchmark. Finally, some more possible tool applications are briefly outlined and the future outlook is discussed in Chapter 6.

2 VIRTUAL SOLAR FIELD - SOLAR FIELD MODEL

The Virtual Solar Field (VSF) is the simulation tool for parabolic trough power plants developed within this thesis. It models the HTF flowing from the power block (PB) through the main distributing header pipes to the subfields through the solar collector loops and back through the collecting header pipes to the PB. In contrast to solar thermal power plant simulation tools discussed in Chapter 1, VSF models every single loop and header pipe in the solar field. Common simulation tools, like tools based on Modelica, solve the complete system using a set of mathematical equations defined by Modelica compilers [35]. This costs a lot of computational time and resources rendering them unsuitable for large systems in the order of hundreds of kilometers of piping. Having complete control on the mathematical formulation of the physical problem paves the way to much more computationally efficient implementations.

On the other hand, VSF is based on coupling a hydraulic network solver to compute the flow distribution among the pipes in the field with a transient thermal solver to compute the temperatures with respect to the local thermal condition and thermal losses in the pipes. The model can predict the transient behaviour of full-sized solar fields in detail using realistic irradiance conditions.

Commercial PT solar thermal power plants cover large areas of land which makes them exposed to spatially varying solar irradiance. Hence, the detailed modelling for all collector loops and pipes in the VSF is essential to accurately predict the thermal energy output of the field. For example, Andasol-III power plant in southern Spain covers approximately $2\,\mathrm{km}^2$ of land [64] and Shams-1 near Abu Dhabi in the United Arab Emirates covers approximately $2.5\,\mathrm{km}^2$. The large stretch causes inhomogeneous thermal energy input to the different collector loops, hence causing the fluid to reach different temperatures. This, in turn, alters the flow distribution in the parallel pipes in the hydraulic network since the physical properties of the HTF are temperature dependent as reported in [1].

In this chapter, the governing equations and modelling approaches, assumptions and limitations are thoroughly discussed. Figure 2.1 depicts the solution algorithm adopted in VSF, as well as, the components of the simulation tool. Firstly, the hydraulic solver that computes the flow distribution depending on the pressure losses in the different pipes and valves is described in Section 2.1. Secondly, the thermal model is outlined in Section 2.2. It is based on one-dimensional discretization of the continuity and energy equations for the flow in all receiver pipes (loops), and header and runner pipes. Finally, the whole system model and implementation including fluid mixing, as well as the model inputs, are described in Section 2.3.

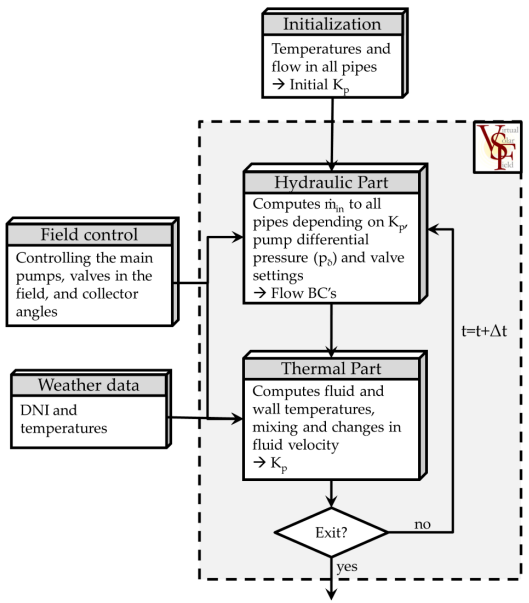

Figure 2.1. A schematic of the solution algorithm adopted in VSF.

2.1 HYDRAULIC PART

The solar field is modelled as a closed piping network with a central pump at the PB driving the HTF in the main header pipes. This approach is typically used to model large water networks and is thus referred to in this thesis as the hydraulic part. The flow is then split among the parallel subfields and then further split among the parallel loops. Figure 2.2 shows a simplified schematic for the hydraulic network in the solar field with the main pump, the subfields and the loops illustrated. Throttling valves in the loops and at the entrance of each subfield are also modelled.

The aim of the hydraulic part is to compute the mass flow rate distribution within the parallel loops for the corresponding pressure difference provided by the pump across the inlet and outlet of the network. The model is described in detail in the following sections.

2.1.1 Flow distribution and field balancing

As analogous to electric circuits, the flow splitting between 2 branches depends on the pressure drop in each branch. The splitting has to satisfy the fluid continuity and energy conservation principles as illustrated in [18, 80]. A viscous fluid loses some energy in the form of head or pressure loss due to the friction with the pipe walls according to the pressure form of the Bernoulli law for incompressible fluids. According to the Darcy-Weisbach

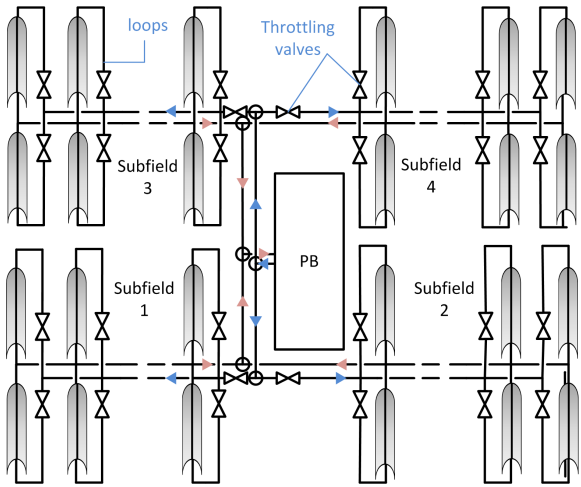

Figure 2.2. The layout of a parabolic trough solar field simulated by the VSF.

relation, the head loss in pipe flow is proportional to the flow velocity, fluid physical properties, pipe geometry, wall roughness, and the flow regime. The frictional head loss is given in [86] as

$$h_f = f\frac{L}{D_{in}}\frac{v^2}{2g}, \tag{2.1}$$

where f is the Darcy friction factor. It depends on the shear stresses in the fluid resulting from contact with the pipe walls. Different computation methods for f are listed in Appendix B. L and D_{in} are the pipe length and inner diameter, respectively. v is the mean flow velocity of the fluid in the pipe and g is the gravitational acceleration. Since the fluid properties are temperature-dependent (see Appendix A), the pressure drop along the specific pipe is considered as the conserved quantity instead of the frictional head loss, such that $\Delta p_p = \rho g h_f$. The same also applies for the velocity, and thus, the mass flow rate is used instead, such that $v = \dot{m}/(A_{in}\rho)$, where A_{in} is the inner pipe area. The pressure drop along a pipe section of length L, Δp_p, in terms of the mass flow rate, $\dot{m}$, and the pipes total hydraulic resistance, $K_{p,total}$, is expressed as

$$\Delta p_p = K_{p,total}\dot{m}^2. \tag{2.2}$$

In a solar field, throttling valves are used at the entrance of loops and subfields to compensate for the pressure losses in the header pipes and balance the fluid flow in all parallel loops in the different subfields. The valves also account for the different hydraulic resistances in the subfields in case the number of loops in each section is different. The valves are also used to control the flow in the individual subfields to account for cloud passages. In VSF, a generic modelling approach for valves is adopted. It is assumed that the valves can be represented by orifices with appropriate openings that constrict the pipe

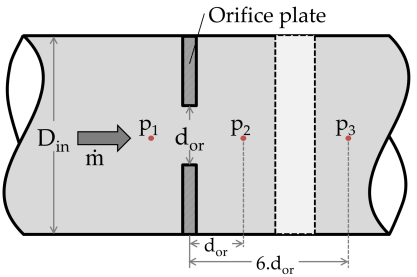

Figure 2.3. A sketch of an orifice plate in a pipe.

entrances and cause a drop in fluid pressure. This approach provides a straightforward relation between the pressure drop and orifice opening, which simplifies the integration in the used simulation scheme. The orifice plate is assumed to be perfectly flat with a perfect straight circular opening. The hole is also assumed to be concentric and the pipe surface directly after the orifice plates are considered perfectly smooth. Figure 2.3 shows a sketch of an orifice plate with a hole with diameter d_{or} in a pipe with diameter D_{in}. The mass flow rate passing through such an orifice is given in [71] as

$$\dot{m} = \frac{c_D \epsilon_{exp}}{\sqrt{1-\beta^4}} \frac{\pi d_{or}}{4} \sqrt{2\rho\Delta p} \,. \tag{2.3}$$

ϵ_{exp} is the expandability factor, which is equal to one for incompressible fluids. The diameter ratio, β, is equal to $\frac{d_{or}}{D_{in}}$ and the relation is valid for $0.2 \leqslant \beta \leqslant 0.6$; however the relation is used also outside the validity range, since it fulfills the qualitative behaviour as shown in Figure 2.4 and discussed below. ρ is the density of the fluid at the orifice and Δp is the undeveloped pressure difference across the orifice, $p_2 - p_1$ as represented in Figure 2.3. Therefore, by changing the orifice diameter, the mass flow rate changes, given a constant pressure drop in the orifice. c_D is the discharge coefficient of the orifice calculated as a function of the Reynolds number, Re, according to [9] as:

$$c_D = \frac{c_{D,max}\sqrt{Re}}{\sqrt{Re} + \sqrt{Re_{crit}}} \,, \tag{2.4}$$

where $c_{D,max} = 0.611$ and $Re_{crit} = 9.33$. The flow develops at a length of $6 \cdot d_{or}$ downstream the orifice, such that the kinetic energy of the vortices and in the turbulence following the hole recovers to static pressure, p_3. The pressure drop, $\Delta p_{or} = p_3 - p_1$, is given according to [71] as:

$$\Delta p_{or} = \left(1 - \beta^{1.9}\right) \Delta p \,. \tag{2.5}$$

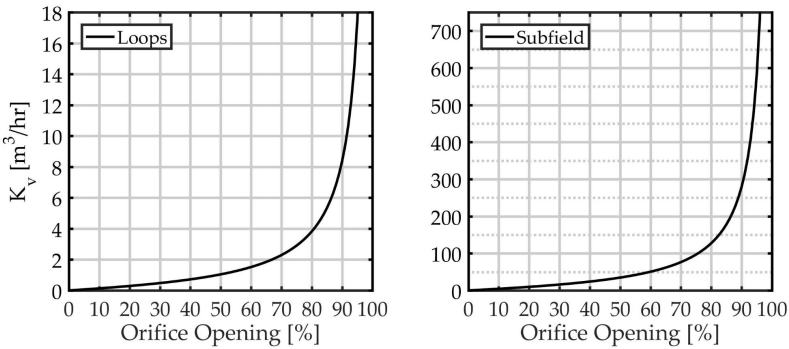

Figure 2.4. K_v values for orifices used as loop (left) and subfield (right) valves in VSF.

By rearranging Equation (2.3) in the form $\Delta p_{or} = K_{orifice} \dot{m}^2$ as in Equation (2.2) and substituting for Δp_{or}, we compute the hydraulic resistance of the orifice, $K_{orifice}$, as:

$$K_{orifice} = \frac{\left(1 - \beta^{1.9}\right)\left(1 - \beta^4\right)}{2\left(c_D A_{or}\right)^2 \rho}, \tag{2.6}$$

where A_{or} is the area of the orifice hole with a maximum value marginally smaller than the pipe inner area to avoid numerical division by zero when computing the flow according to Equation (2.3). Using the above procedure for all valves in the field, VSF computes the total hydraulic resistance in each pipe according to the valve or orifice opening. This is then used to compute the mass flow distribution in the field as explained in Section 2.1.3.

In comparison, valve manufacturers tend to tabulate the valve characteristic curves using the valve flow coefficient, K_v, as mentioned in [84, 86]. Figure 2.4 shows the K_v values for the orifices used as loop valves in a pipe with inner diameter of 66 mm like the SCHOTT PTR®70 receiver tubes as in [74] and subfield valves. The orifice opening is computed as $\frac{A_{or}}{A_{in}}$, where A_{in} is the pipe inner cross-section area. However, a completely blocked orifice with $A_{or} = 0$ would result in an infinite value for the hydraulic resistance and pressure loss resulting in a numerical error in the simulation. Hence, a minimum A_{or} of 1×10^{-5} m^2 is adopted. This results in a minimum valve opening of 0.3 % for the loops and approximately 0.01 % for the subfield orifices. The procedure to calculate the valve flow coefficient from the orifice opening is described in Appendix C.

To demonstrate the flow distribution in the loops, Figure 2.5 shows a sketch of a steady-state simulation for the flow distribution in 19 parallel loops under constant pressure difference of 7.8 bar from the PB and thermal oil as HTF. The loops are 600 m long, have an inner diameter of 66 mm and are subjected to a homogeneous effective irradiance of 900 W m^{-2}. The distributor and collector headers, blue and red lines, respectively, have cascaded diameters from $D_{h1} = 240$ mm to $D_{h19} = 70$ mm. The header sections are 34 m long between

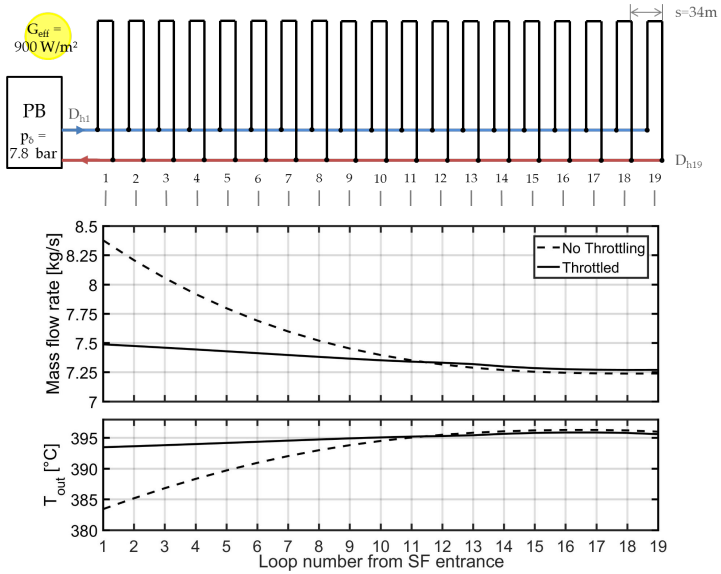

Figure 2.5. Example of the steady-state solution of 19 loops with thermal oil as HTF. The mass flow rate and loop outlet temperature in each loop are plotted for the cases without (dashed) and with (solid) throttling.

the loops. The mass flow rate and loop outlet temperatures for cases with and without throttling valves are also plotted in the figure. From the no throttling case, it can be seen that the loops further away from the PB get lower mass flow than the ones closer to the pump. This is due to the additional resistance of the header pipes lengths, which vary among the loops. As a result, inhomogeneous loop outlet temperatures are achieved. Thus, throttling valves are added to the entrance of each loop and their openings kept fixed to balance the flow in the whole network. This results in more homogeneous loop outlet temperatures as shown by the solid lines in Figure 2.5. The difference in flow rate between the first and last loops is reduced from 13.7 % to just 3 % for a total header length of 612 m. Furthermore, the total mass flow rate in all the loops of the exemplary solar field with the valves is lower, since the valves increase the total hydraulic resistance of the field. Absolutely equal mass flow rate in all loops is not reached due to the initialization of the valves as the pressure drop depends on the overall flow rate, which changes with the valve setting. More about field balancing and the initialization of valve settings in solar fields is described in Section 2.3.

2.1.2 Static model assumption

The transient behaviour in the hydraulic model is neglected due to the large difference in time scales between the flow distribution and the heat transfer and fluid flow problems.

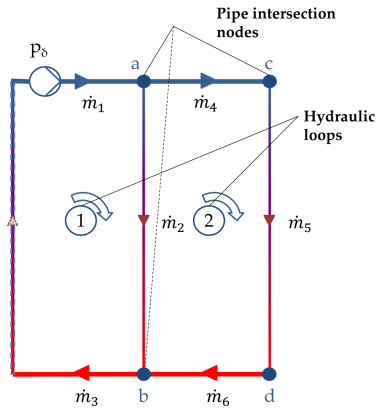

Figure 2.6. Schematic for parallel loops in a hydraulic network. Thick blue lines represent the distributor header, red lines are the collector headers and the thin gradually varying colours lines represent the loop pipes.

The pressure wave transporting change in pressure propagates through the network by the speed of sound which is approximately $1300\,\mathrm{m\,s^{-1}}$ for common oils [88, 91] and approximately $1500\,\mathrm{m\,s^{-1}}$ for heat transfer salts as stated in [53]. These salts are very similar in composition to typical solar salts. On the other hand, fluid flow in the system is governed by the flow velocity of the fluid, which is typically in the order of $2\,\mathrm{m\,s^{-1}}$, 3 orders of magnitude less than the speed of sound. As a result, a static model is used in every time step to compute the quasi-steady state fluid flow distribution in the pipes.

2.1.3 Governing equations

In this thesis, the node-loop methods described in [10, 18, 80] have been adapted to consider temperature dependent fluid properties. Figure 2.6 shows a schematic of a hydraulic network with multiple loops in parallel. The flow is driven by a pressure difference of p_δ provided by a pump as indicated in the figure.

According to the node-loop method, hydraulic networks are defined by: (1) pipe intersection nodes, and (2) closed hydraulic loops. According to Kirchhoff's first law applied to fluid flow, also known as the junction rule, the fluid divided among or collected from the pipes connected to a node must satisfy the mass conservation principle. For example, the mass balance at nodes a and b in Figure 2.6 are

$$\begin{aligned} \dot{m}_1 - \dot{m}_2 - \dot{m}_4 &= 0 \text{ and} \\ \dot{m}_2 + \dot{m}_6 - \dot{m}_3 &= 0\,, \end{aligned} \tag{2.7}$$

respectively. Loop equations represent the energy balance in the pressure form of the Bernouli equations in a pipe. The pressure drop depends on the total hydraulic resistance and the flow rate in the pipe as stated in Equation (2.2). The hydraulic resistance of a pipe, K_p, is derived from Equation (2.1) and Equation (2.2) as:

$$K_p = \frac{fL}{2A_{in}^2 D_{in}\rho}\,. \tag{2.8}$$

K_p is, thus, a function of density which varies with the temperature in the pipe. Since the temperatures vary significantly along the length of a loop, the hydraulic resistance and friction coefficient are computed for each discretized section in a pipe. They depend on local temperatures and flow velocities. Then the values of K_p are arithmetically summed up to give the total resistance of the pipe.

According to the pressure form of the Bernoulli equation for viscous fluid flow, the pressure drop between two points on a stream line is equal to the pressure loss due to friction between the points. Within a closed hydraulic loop, represented by the rounded arrows in Figure 2.6, the sum of pressure drop in all the pipes forming the loop must be equal to zero as the fluid traverses the loop. A positive flow direction is considered if the fluid in the pipe moves in clock-wise direction around the loop. Flow in the opposite direction gets a negative sign resulting in a negative pressure drop, for example, $\dot{m}_2$ in loop number 2. A pump in the loop acts as a source of pressure difference and is considered as a pressure source term as shown in Equation (2.9). Following this principle, the loop equation for loops number 1 and 2 in Figure 2.6 is

$$\begin{aligned} K_{p1}|\dot{m}_1|\dot{m}_1 + K_{p2}|\dot{m}_2|\dot{m}_2 + K_{p3}|\dot{m}_3|\dot{m}_3 &= p_\delta \text{ and} \\ K_{p4}|\dot{m}_4|\dot{m}_4 + K_{p5}|\dot{m}_5|\dot{m}_5 + K_{p6}|\dot{m}_6|\dot{m}_6 - K_{p2}|\dot{m}_2|\dot{m}_2 &= 0\,. \end{aligned} \tag{2.9}$$

The node and loop equations 2.7 and 2.9, respectively, are formulated for all junctions and hydraulic loops in the system. They are then arranged in a matrix form as a non-linear system of equations in the vector of mass flow rates in the different pipes, $\dot{\boldsymbol{m}}$, as

$$\mathbf{K}\dot{\boldsymbol{m}} = \boldsymbol{F}\,. \tag{2.10}$$

$\boldsymbol{F}$ represents the right-hand side of the node and loop equations. The matrix $\mathbf{K}$ is the matrix of coefficients from the node and loop equations having the following form for the network sketched in Figure 2.6 as an example:

$$\mathbf{K} = \begin{bmatrix} 1 & -1 & 0 & -1 & 0 & 0 \\ 0 & 1 & -1 & 0 & 0 & 1 \\ \vdots & & \vdots & & & \vdots \\ K_{p1}|\dot{m}_1| & K_{p2}|\dot{m}_2| & K_{p3}|\dot{m}_3| & 0 & 0 & 0 \\ 0 & -K_{p2}|\dot{m}_2| & 0 & K_{p4}|\dot{m}_4| & K_{p5}|\dot{m}_5| & K_{p6}|\dot{m}_6| \end{bmatrix} \begin{matrix} \left.\vphantom{\begin{matrix}1\\1\end{matrix}}\right\} \text{node equations} \\ \\ \left.\vphantom{\begin{matrix}1\\1\end{matrix}}\right\} \text{loop equations} \end{matrix} \tag{2.11}$$

The matrix entries in the loop equations are nonlinear in $\dot{m}$, thus, the solution is iterated to convergence of the mass flow rates as described in Section 2.1.4. The total size of the matrix is $(n_{pipes} \times n_{pipes})$, where the number of pipes, n_{pipes}, depends on the configuration of the hydraulic network, as well as the number of collector loops, n_{loops}. For the common H-layout solar fields with 4 subfields the number of pipes can be computed as

$$n_{pipes} = 3n_{loops} + 6\,. \tag{2.12}$$

2.1.4 Implementation

The simulation tool in its current form can model H-layout solar fields with 1-4 subfields and arbitrary number of loops per subfield. However, it could be expanded for more layouts and subfield numbers. The user can input the orientation of the loops with respect to the north direction, as well as, the geometry of every single loop and the characteristics of the throttling valves. Figure 2.2 shows the general layout implemented in VSF.

The equation system of the hydraulic network is solved using the Newton-Raphson procedure for solving systems of non-linear equations. Newton-Raphson methods are efficient and well-suited for problems with close initial guesses. This applies to all simulations in this thesis. For more sophisticated problems, implicit secant and multi-grid methods case be used.

All nodes in the system are numbered and the nodal discharge equation for node number j can be written as:

$$F_j = \sum_{i=1}^{n_j} \dot{m}_{j,i} = 0\,, \tag{2.13}$$

where the index i runs for all n_j pipes connected to the node j. The pressure loss equations are formulated for each hydraulic loop, k, in the system and can be written as:

$$F_k = \sum_{i=1}^{n_k} (K_p)_i \, |\dot{m}_{k,i}| \dot{m}_{k,i} = \Delta p_{ext,k}\,, \tag{2.14}$$

where the summation index, i, runs for all n_k pipes forming the closed loop and $\dot{m}_{k,i}$ is the mass flow rate in pipe number i of loop k. Then the set of non-linear equations in Equation (2.13) and (2.14) are expanded in a Taylor series, formulated in matrix-vector form and solved iteratively using the Newton-Raphson method as:

$$\frac{\partial \boldsymbol{F}}{\partial \dot{\boldsymbol{m}}} \left(\dot{\boldsymbol{m}}_t - \dot{\boldsymbol{m}}_{t-\Delta t} \right) = -\boldsymbol{F}\,, \tag{2.15}$$

where $\frac{\partial \boldsymbol{F}}{\partial \dot{\boldsymbol{m}}}$ is the Jacobian matrix of the derivatives, and $\dot{\boldsymbol{m}}_t$ and $\dot{\boldsymbol{m}}_{t-1}$ are the mass flow rate vectors for the current and previous iterations, respectively. $\boldsymbol{F}$ is the vector of the node and loop equations including the pressure difference between the solar field inlet and outlet in the first hydraulic loop. The mass flow rate is then solved as:

$$\dot{\boldsymbol{m}}_t = \dot{\boldsymbol{m}}_{t-\Delta t} - \left[\frac{\partial \boldsymbol{F}}{\partial \dot{\boldsymbol{m}}} \right]^{-1} \boldsymbol{F}\,. \tag{2.16}$$

The procedure is iterated until the difference between the current and previous solutions falls below a threshold value, $\delta\dot{m}$. It is also important to note that the values for K_p are computed for each discretized element in a pipe and includes the Darcy friction coefficient, f, which is a function of the velocity and mass flow rate in the corresponding element. Therefore, global iterations are performed to resolve such nonlinearities through computing the new coefficients according to the new fluid velocities.

The linear algebra library, Armadillo, is used to solve the equation system according to [73]. Armadillo provides a very efficient and user-friendly open-source library for the C++ programming language. It includes numerous functions for vector and matrix operations for various datatypes.

Another method for solving hydraulic networks is called the Hardy-Cross method [80]. It is based on solving the nodal and loop equations independently by introducing a flow correction factor to satisfy each equation. Then the solution is iterated till the correction factors are small enough. Although this solution method is simple to implement and provides good results for small networks, it was very inefficient and inaccurate for the large hydraulic networks in full-scale solar fields. For example, an Andasol III-like solar field required more than 1 million iterations to converge, while only 15 iterations are needed using the NR method. Figure 2.7 shows the different computation times for an initial implementation of the hydraulic solver in MATLAB® .

During transient warm up or cool down of the fluid, the fluid expands or contracts in the pipe, which causes the flow rate to vary along its length. Hence, the calculated $\dot{\boldsymbol{m}}$ vector above is the average mass flow rate in the pipe, $\dot{m}_{avg}$, from which the inlet mass flow rate is computed using a linear interpolation using the gradient from the previous time step, $t - \Delta t$, such that:

$$\dot{m}_{in}^{t} = \dot{m}_{avg}^{t} + \frac{\dot{m}_{in}^{t-\Delta t} - \dot{m}_{out}^{t-\Delta t}}{2}\,. \tag{2.17}$$

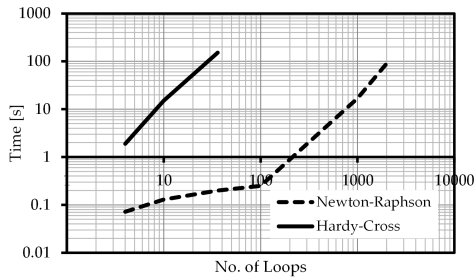

Figure 2.7. Comparison of computation times of the Newton-Raphson and Hardy-Cross methods for networks with different number of loops.

The inlet mass flow is then used as a flow boundary condition for the dynamic thermal model to compute the heat transfer along each pipe as described in the next section.

2.2 THERMAL PART

As illustrated in Figure 2.1, the inlet mass flow rate in each pipe (refer to Equation (2.17)) is passed to the thermal solver. There, the temperature of the HTF and the transient heat transfer in response to the varying DNI and according to the field control are computed. Mass and energy balance equations are solved for the flowing fluid, and energy balance equations are solved for the pipe walls. The use of hydraulic and thermal solvers results in adequate coupling of the thermal and flow conditions in the field without the need to solve momentum balance equations for the fluid in the thermal part. This results in a computationally efficient algorithm to model whole solar fields having total piping lengths in the order of hundreds of kilometers within reasonable time for the applications.

The exact axial temperature distribution in the pipes is not of interest for the intended investigations, since the flow is mostly turbulent during common operation conditions. Thus in VSF, we use a one-dimensional model for all receiver pipes (loops), and header and runner pipes. A simplified model for the thermal losses in the receiver pipes is adopted by using empirical relations without modelling the glass envelop. In this section, the governing equations and main assumptions are described and discussed, respectively.

2.2.1 Governing equations

Fluid Equations

The basic incompressible viscous fluid equations stating the three fundamental principles of physics, namely mass, momentum and energy conservation, for axisymmetric flow are given in the conservative form in [5, 26] as

$$\frac{\partial \rho_f}{\partial t} + \frac{\partial (\rho_f v_f)}{\partial x} = 0\,, \tag{2.18}$$

$$\frac{\partial (\rho_f v_f)}{\partial t} + \frac{\partial (\rho_f v_f v_f)}{\partial x} = \frac{\partial}{\partial x}\left(-p + \tau_{xx}\right) - \rho_f g \frac{\partial z}{\partial x} \quad \text{and} \tag{2.19}$$

$$\frac{\partial E_t}{\partial t} + \frac{\partial (E_t v_f)}{\partial x} = S_f + \frac{\partial}{\partial x}\left[(-p + \tau_{xx}) v_f\right]\,. \tag{2.20}$$

where ρ_f, v_f, and E_t are the fluid density, velocity and total energy, respectively. S_f is the fluid energy source term and p is the fluid pressure. As the fluid is dynamically incompressible, its density is considered to be function of the temperature only. τ_{xx} is the shear force, such that its derivative $\frac{\partial \tau_{xx}}{\partial x} = \Phi$ is the dissipation of momentum per unit length. It can be given by the pressure drop relation in 1D flow in a pipe with inner diameter D_{in} and a Darcy friction factor, f, according to [86] as:

$$\Phi = \frac{\rho_f f}{2 D_{in}} v_f^2\,. \tag{2.21}$$

The continuity equation is reformulated to compute the spatial gradient of the velocity resulting from the expansion or contraction of the fluid. The chain rule is used to reformulate the density gradients in terms of temperature gradients such that

$$\frac{\partial \rho_f}{\partial \xi} = \frac{\partial \rho_f}{\partial T_f} \cdot \frac{\partial T_f}{\partial \xi}\,, \tag{2.22}$$

where ξ represents general variables, namely t and x for this case. We then express the spatial gradient of the velocity as

$$\frac{\partial v_f}{\partial x} = -\frac{1}{\rho_f} \frac{\partial \rho_f}{\partial T_f} \left(\frac{\partial T_f}{\partial t} + v_f \frac{\partial T_f}{\partial x} \right)\,. \tag{2.23}$$

Figure 2.8 shows a sketch of the energy balance in the receiver tubes. The linear density of the solar energy incident on the tube, thermal losses, and convective heat transferred between the pipe walls and the fluid are indicated by $\dot{q}_{sol}$, $\dot{q}_{loss}$, and $\dot{q}_{conv}$, respectively. T_w and t_w represent the wall temperature and thickness. The momentum equation is used to simplify the energy equation by substituting

$$\frac{\partial p}{\partial x} = \Phi - \rho g \frac{\partial z}{\partial x} - \rho \left(\frac{\partial v_f}{\partial t} + v_f \frac{\partial v_f}{\partial x} \right)\,. \tag{2.24}$$

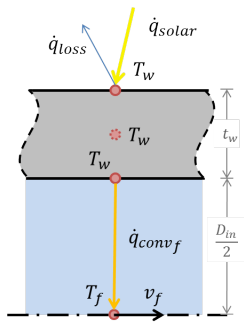

Figure 2.8. A sketch of the energy balance on a fluid element moving in the receiver pipes.

The total energy, E_t, is the sum of internal, kinetic and potential energies according to [42, 81, 86] and is expressed in the equation

$$E_t = \rho \left(\hat{u} + \frac{v^2}{2} + gz \right) . \tag{2.25}$$

The term $p(\partial v_f/\partial x)$ resulting from the product differentiation in Equation (2.20) is commonly negligible for incompressible fluids [26, 42]. The terms in the equation are evaluated for typical operation conditions to analyse the weights of the different terms. This term was found to represent only $0.4 - 0.25\,\%$ of the energy input to the fluid for common operation conditions and HTFs. An example set-up of this analysis is shown in Figure 2.9. For this reason, we could simplify the energy equation to the form

$$\rho_f A_{in} \left(\frac{\partial \hat{u}}{\partial t} + v \frac{\partial \hat{u}}{\partial x} \right) = S_f . \tag{2.26}$$

Then, by applying the chain rule to decompose the derivatives of the internal energy as we did for the density term in Equation (2.22), we get the term $\partial \hat{u}/\partial T_f$ and temperature derivatives. We then substitute the term $\partial \hat{u}/\partial T_f$ for the specific heat capacity of the fluid c_v [88] and the energy equation can be finally written as

$$\rho_f A_{in} c_v \left(\frac{\partial T_f}{\partial t} + v \frac{\partial T_f}{\partial x} \right) = S_f . \tag{2.27}$$

For incompressible fluids, $c_p = c_v$ and they can be interchanged.

Fluid energy source term

Heat transfer in pipe flow is dominated by convection while axial heat conduction is neglected. This is due to the very high Nusselt number of the flow [42]. The Nusselt number represents the ratio of convective to conductive transport and is calculated as the product

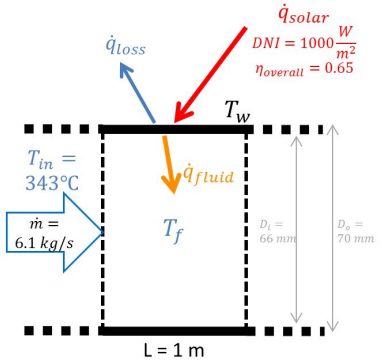

Figure 2.9. Sketch with the values used for computing the relative weights of the terms in the momentum equation for oil.

of the Reynolds and Prandtl numbers. Therefore, the energy source term for the fluid in receivers is equal to the convective heat flux, which is expressed as

$$S_f = \dot{q}_{conv} = \alpha_f \pi D_{in} (T_w - T_f)\,. \tag{2.28}$$

$\dot{q}_{conv}$ is the convective heat transfer rate per unit length between the HTF and the pipe walls at a temperature of T_w as indicated in Figure 2.8. α_f is the coefficient of heat transfer by mixed convection. Mixed convective heat transfer is considered since free convection becomes significant when the flow rate is very low at stand-still operations or recirculation at low flow velocities. The heat transfer coefficient is computed as a function of the Nusselt number as

$$\alpha_f = \frac{\lambda}{D_{in}} \left(Nu_{forced}^n + Nu_{free}^n \right)^{1/n}\,, \tag{2.29}$$

where λ is the coefficient of heat conduction of the HTF and n is a exponent to compute the mixed convection. The Nusselt number for forced convection is computed using either the Dittus-Boelter equation or the Gnielinski correlation [37]. As for free convection, the Nusselt number is computed as a function of the Rayleigh number according to [44]. The equations are given in Appendix D.

The values of the exponent n typically range from 3–4 [37]; however, for the initial implementations, the computation of the mixed Nusselt number is 60 times slower than if a simple addition with $n = 1$ is used. The loss in accuracy is not significant for typical solar field operation, where the mixed Nusselt number is approximately 4 % lower for a mass flow rate of $7\,kg\,s^{-1}$, as the free convection is so low in comparison to forced convection. The lower Nusselt number results in slightly higher wall temperatures, which in turn result in an increase in thermal losses of approximately 0.07 % for typical operation conditions. This error rises to a maximum of 0.8 % if very low mass flows of $0.5\,kg\,s^{-1}$ in the loops are considered.

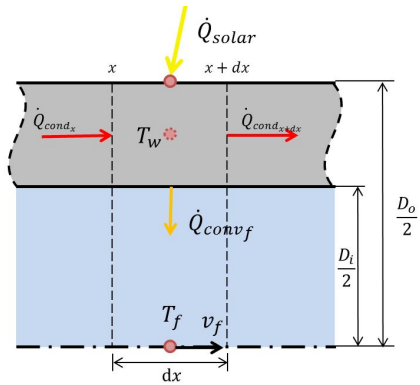

Figure 2.10. Schematic for heat transfer in pipe wall element with thickness dx. The grey (darker) shade represents the wall of the pipe and the light blue shade represents the HTF.

Receiver pipe wall equations

According to [15, 66, 93], the energy balance in one-dimensional rigid pipe walls can be expressed by

$$\rho_w A_{CS} c_{p_w} \frac{\partial T_w}{\partial t} + \lambda_w A_{CS} \frac{\partial^2 T_w}{\partial x^2} = S_w \,, \tag{2.30}$$

where A_{CS} is the wall cross-section area, and ρ_w, c_{p_w} and λ_w are wall density, specific heat capacity and coefficient of heat conduction, respectively. S_w is the energy source term in the pipe walls. We consider constant physical properties of the steel pipes over the temperature range. The Biot number of typical flow conditions range between 0.02 and 0.17. As a result, typical absorber tube models in literature consider the pipe wall as a lumped mass without any radial distribution of temperature within the thickness of the pipe walls. This assumption is also taken in the model implemented in VSF.

To simplify the wall energy equation, the axial heat conduction term in the pipe wall is often neglected in literature [15, 92]. To justify this, an analysis is performed for 1D heat transfer in a section of a pipe as sketched in Figure 2.10 that shows a wall element and the different heat fluxes. The analysis is based on methods used in microchannel flow to prove the significance of axial heat conduction in such cases as explained in [52]. The axial conduction heat transfer coefficient and the coefficient of heat transfer to the fluid from pipe entrance to pipe exit are compared. For typical operation conditions in commercial solar fields, the axial heat conduction in the walls represents less than 0.0001% of the convected heat to the fluid, and hence is neglected.

Wall energy source term

The energy source term is calculated from the balance on a wall element as illustrated in Figure 2.8 as

$$S_w = \dot{q}_{sol} - \dot{q}_{loss} - \dot{q}_{conv}\,, \tag{2.31}$$

where $\dot{q}_{sol}$ is the incident solar energy on the absorber tube as explained in Section 2.3.2 and $\dot{q}_{loss}$ represents the thermal losses from the receiver pipes. The losses are computed using simplified empirical relations in terms of T_w provided for common receiver manufacturers. For example, the thermal losses in SCHOTT®PTR70 as documented in [13] as given as

$$\dot{q}_{loss} = 0.141 \cdot T_w + 6.48 \times 10^{-9} \cdot T_w^4\,. \tag{2.32}$$

Other relations for the UVAC III absorber tube by Solel is given in [12].

Header pipes

Heat transfer rates in the header pipes are much lower than in the absorber tubes due to the thick insulation material. Hence, a single header temperature is used to represent the fluid as a model simplification. This will affect the start-up time of the solar field where the header pipe temperatures are low as compared to the solar field inlet temperatures from the cold storage tank. However, this case is not significant for the investigated test cases in this thesis and will be addressed for future investigations as discussed in Chapter 6. The fluid energy balance equation for the headers can be expressed as

$$\rho_f A_{in} c_v \left(\frac{\partial T_f}{\partial t} + v \frac{\partial T_f}{\partial x} \right) = -\dot{q}_{loss,h}\,, \tag{2.33}$$

where $\dot{q}_{loss,h}$ is the heat lost from an insulated pipe computed as

$$\dot{q}_{loss,h} = \frac{2\pi}{\ln\left[\frac{D_{out}+2t_{ins}}{D_{out}}\right]} \lambda_{ins} \left(T_w - T_{ins}\right)\,, \tag{2.34}$$

according to [84]. T_{ins} is the outer temperature and t_{ins} is the thickness of the insulation material fitted on the pipe. The coefficient of conduction depends on the insulation materials, common insulation materials used are MinWool-1260® and THERMO-12 Gold® for the cold and hot headers, respectively [30]. The computation for insulation outer temperatures and heat conductivities is explained in Appendix E.

2.2.2 Implementation

In this section, the numerical methods used to solve the governing equations are discussed. All spatial derivatives are based on 1st-order approximations and the 2nd- and 4th-order Runge-Kutta (RK) schemes are used for explicit time integration.

Firstly, the equations are spatially discretized using a cell-centered 1D finite volume scheme for elements of equal length, Δx. First order upwind schemes are used to compute the spatial gradients since the flow is dominated by convection in a specific upwind direction. Second order schemes have been tested with no significant benefit to the solution accuracy. Figure 2.11 shows the 1D discretization for the wall and fluid elements showing the point to be computed, P, and its neighbours on the east and west, E and W, respectively. So the spatial discretization of the fluid energy equation, Equation (2.27), is

$$\left.\frac{\partial T_f}{\partial t}\right|_i + \frac{v_i}{\Delta x}(T_{f_i} - T_{f_{i-1}}) = \left.\frac{S_f}{\rho \bar{c}_v A_i}\right|_i . \tag{2.35}$$

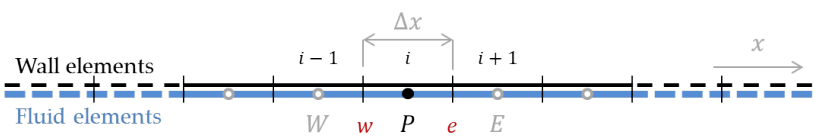

Figure 2.11. Discretization elements for the wall and fluid showing the center point, P, for the element number i and its neighbours in the east, E, and west, W.

As for the time integration of the differential equations, 2nd- and 4th-order RK schemes are used according to [26]. From Equation (2.35), $f_f(T^n_{w,f}, t^n)$ is defined as

$$f_f(T^n_{w,f}, t^n) = \left.\frac{\partial T_f}{\partial t}\right|_i = \left.\frac{S_f}{\rho \bar{c}_v A_i}\right|_i - \frac{v_i}{\Delta x}(T_{f_i} - T_{f_{i-1}}) . \tag{2.36}$$

Also the same is applied to the discretized wall equation and $f_w(T_{w,f}, t)$ is defined as

$$f_w(T_{w,f}, t) = \left.\frac{\partial T_w}{\partial t}\right|_i = \left.\frac{1}{\rho_w c_{p_w} A_{CS}} (\dot{q}_{sol} - \dot{q}_{loss} - \dot{q}_{conv})\right|_i . \tag{2.37}$$

The second order RK scheme for the differential equations is

$$T^{n+1}_i = T^n_i + \frac{k_1 + k_2}{2} , \tag{2.38}$$

where T^n_i represents the fluid or wall temperature at the current time step, while T^{n+1}_i represents the values at the next time step. k_1 and k_2 are the RK coefficients namely the explicit prediction and mid-point correction, respectively. They are computed as a combination of the derivatives as

$$k_1 = \Delta t\, f(T^n_{w,f}, t^n) , \tag{2.39}$$

$$k_2 = \Delta t\, f(T^n_{w,f} + k_1, t^n + \Delta t) . \tag{2.40}$$

Δt is the size of the time step and $f(T^n_{w,f} + k_1, t^n + \Delta t)$ is a gradient predictor for the following time step. Similarly, the fourth order RK step is expressed by

$$T^{n+1}_i = T^n_i + \frac{k_1 + 2k_2 + 2k_3 + k_4}{6}, \tag{2.41}$$

where

$$k_1 = \Delta t\, f_f(T^n_{w,f}, t^n), \tag{2.42}$$

$$k_2 = \Delta t\, f_f(T^n_{w,f} + \frac{k_1}{2}, t^n + \frac{\Delta t}{2}), \tag{2.43}$$

$$k_3 = \Delta t\, f_f(T^n_{w,f} + \frac{k_2}{2}, t^n + \frac{\Delta t}{2}) \quad \text{and} \tag{2.44}$$

$$k_4 = \Delta t\, f_f(T^n_{w,f} + k_3, t^n + \Delta t). \tag{2.45}$$

Fluid continuity equation

The continuity equation is used to couple the fluid velocity with the temperature gradients. After the gradients are computed within the RK step, the velocity gradient is computed as

$$\left.\frac{\partial v}{\partial x}\right|_i = -\frac{1}{\rho_i}\left.\frac{\partial \rho}{\partial T}\right|_i \left[\left.\frac{\partial T}{\partial t}\right|_i + v\left.\frac{\partial T}{\partial x}\right|_i\right]. \tag{2.46}$$

The velocity of a cell is then computed from the propagation of the inlet velocity. This inlet velocity is computed using the hydraulic solver depending on the flow distribution in the network as explained Section 2.1.

Numerical stability

The stability of explicit time integration schemes is dependent on the choice of the size of the time step and the length of the discretized elements in relation to the flow velocity of the fluid, v. The Courant-Friedrichs-Lewy (CFL) criteria needs to be satisfied in order to ensure the stability of the numerical scheme, such that

$$0 < v\frac{\Delta t}{\Delta x} < \mathrm{CFL}, \tag{2.47}$$

where CFL is the Courant number having a value between 0 and 1. The time step is computed for each element and, since the velocity of the cells are different (depending on the temperature), the minimum value is used for integrating all equations.

Nevertheless, in VSF, a fixed time step size is chosen that satisfies the CFL condition for all the loops in normal operation conditions. This spares the computation for each of

the discretized cells. However, since the headers vary significantly in length and diameter, some header pipes require smaller time steps. Consequently, the maximum time step allowed for the header pipes is computed as

$$\Delta t_{max,h} = CFL_{max} \frac{\Delta x}{v} . \tag{2.48}$$

Then, sub-iterations are performed only when and where necessary to allow for higher time step sizes for the whole solar field saving computational time.

2.3 SYSTEM MODEL

2.3.1 Coupling hydraulic and thermal parts

In this section, the combination of the hydraulic and thermal models to simulate full-scale solar fields is explained. The main structure of the program is illustrated in Figure 2.1. Firstly, loop and subfield valve openings are set in order to balance the plant. The nominal operation condition is input to the model, including nominal effective irradiance, and field inlet and outlet temperatures. From this information, the total nominal mass flow rate is computed according to a static energy balance depending on the average thermal losses and fluid properties. Then, an equal distribution of the flow among all loops is assumed and the valve setting needed to achieve this homogeneous distribution is acquired. The valve settings are kept constant throughout the entire simulation, except if a valve controller is used, as discussed in Section 5.3.

Secondly, the total hydraulic resistances in different pipes are computed and fed into the hydraulic solver, that in turn, computes the inflow velocity for each pipe in the solar field according to the pressure difference across the field inlet and outlet. The velocity is used as boundary condition for the fluid equations in the thermal part. The temperatures and changes in velocity as described in Section 2.2.2 are then solved for. Within the thermal part, the hydraulic resistance of the discretized elements is computed and summed up for each pipe. The total resistance for each pipe is fed to the hydraulic solver to compute the new flow distribution. Finally, to compute the temperature boundary conditions, the inflow is energetically mixed at the nodes and propagated to the outflow pipe or pipes of this node as illustrated in Figure 2.12. For example, T_3 in the figure is computed as

$$T_3 = \frac{\dot{m}_1 c_{p1} T_1 + \dot{m}_2 c_{p2} T_2}{\dot{m}_3 c_{p3}} . \tag{2.49}$$

For cases when the inlet temperatures to the node are within 50 °C from each other, the variations in specific heat capacity, c_p, are negligible and result in a variation of less than 0.15 % for thermal oil and less than 0.02 % for typical molten salts. For these cases, c_p values cancel out in Equation (2.49).

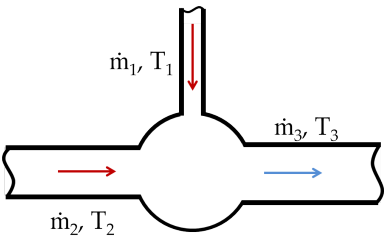

Figure 2.12. Illustration of fluid mixing in a node with 2 inlet pipes and one outlet pipe.

The procedure described above results in loose coupling of the hydraulic and thermal states of the field. The hydraulic state will affect the heat transfer, and hence, the temperatures, and similarly, the thermal condition will affect the hydraulic resistance, consequently affecting the flow velocities in the pipes. Since the update of the hydraulic resistance takes place at the following time step, the coupling is only loose.

The model also offers a high degree of flexibility in setting the geometry of the pipes, the number of loops and subfields, the type and quality of collectors and receivers, and the type of insulation material in the header and runner pipes. VSF is able to take any inhomogeneities of the plant design or manufacturing into account and consider the effect of such irregularities on the fluid distribution in the field. For example, a subfield might have different header lengths or diameters that would directly affect the flow rate going into it. Moreover, flow maldistribution as reported in [1] can be modelled using this simulation tool. For example, to make the flow rate equal in all parallel loops in a subfield, throttling valves are used; however, partial shading of some loops would cause flow maldistribution of the fluid.

Also the user can choose between different field control options, either by providing the time series of the control parameters, or by choosing one of the controllers described in Chapters 4 and 5. In the next section, I discuss how the main energy source, the solar irradiance, is addressed in VSF.

2.3.2 Solar resource

In Equation (2.31), the absorbed solar energy, $\dot{q}_{sol}$, represents the energy input term to the system. As thoroughly discussed in [41], the incident angle of the direct normal solar irradiance (DNI) with respect to a normal on a surface is represented by the solar altitude and azimuth angles. These angles depend on the time of the day and year, as well as the local latitude location of the surface. Different types of solar collectors have various solar tracking strategies that depend on the number of tracking axes, and the shape and orientation of the collector surface.

VSF considers parabolic trough collectors with single axis tracking oriented in the N-S direction. These collectors are equipped with E-W-horizontal solar tracking systems that follow the sun trajectory, such that the surface normal in the center of the parabola is in the direction causing minimum solar incidence angle to the surface when the collectors are fully focused. The effective solar irradiance falling on the collector, G_{eff}, and the absorbed solar energy in the absorber tubes, $\dot{q}_{sol}$, can be expressed as

$$G_{eff} = G_{bn} \cos\varphi \cdot IAM \tag{2.50}$$

$$\dot{q}_{sol} = G_{eff} \cdot w_{ap} \cdot \eta_{opt} \cdot \eta_{endloss} \cdot \eta_{shading} \cdot f_f \,. \tag{2.51}$$

Firstly, the G_{bn} is the measured irradiance falling per unit area of the collector and is multiplied by the net aperture width of the mirrors, w_{ap}. It is corrected according to the sun elevation and azimuth angles through multiplication by the cosine of the angle between the normal to the earth surface and the sun angle ($\cos\varphi$ factor) according to [34, 41]. The incident angle modifier (IAM) is also multiplied by the DNI value to account for the efficiency loss in the collectors due to the off-normal incident sun rays. The IAM is computed for the SKAL-ET collector class according to [8, 51].

Secondly, the combined optical efficiency is multiplied by the effective irradiance. The optical efficiency includes losses associated with the reflection of the mirrors, the absorptivity of the receiver tubes, the transmittance through the glass envelop, gaps between mirror panels and the intercept factor. The intercept factor includes errors in the mirrors, errors in positioning of the absorber pipes, sun-tracking errors and the sun shape. Thirdly, the irradiation lost due to reflection beyond the absorber tubes, $\eta_{endloss}$ are computed according to [30] as a function of the sun incidence angle and collector focal lengths. Finally, the shading of loops is computed as a function of the sun position and the spacing between the collectors according to [41]. The shading factor is a value between 0 and 1 indicating how much of the incident solar radiation is not shadowed by the neighbouring collectors. For N-S-oriented collectors, shading effects from collectors in the east and west directions are significant only at low sun angles during sunrise and sunset.

f_f represents an efficiency factor due to the focusing of the collector in the sun direction. As described in [41], the acceptance angle curve represents the focusing of the collector in terms of the deviation of the collector solar tracking angle from the sun angle. The shape of the curve depends on the mirror geometry and the width of the collector tube. VSF determines percentage focus of the collector according to the acceptance angle curve as shown in Figure 2.13 as an example. A different acceptance angle curve is suggested in [41]; however, no information has been given about the type of collector addressed. The shape of the curve has a significant impact on the computational results as discussed in Chapter 3. The collector drive is modelled by a linear actuator rotating the SCA at a constant angular velocity of $0.2\,^\circ\,s^{-1}$.

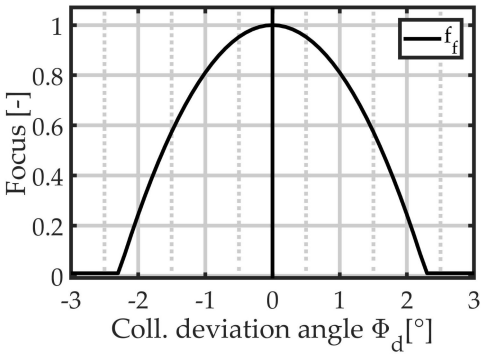

Figure 2.13. Acceptance angle curve (according to communications with industrial partners [29]).

DNI maps and nowcasting systems

With the presence of such a detailed simulation tool that considers individual loops in a solar field, the spatial variation of the solar irradiance on the large extent of the field can be considered. For that, we used spatially-resolved DNI maps from a grid of upward-facing cloud cameras, or downward-facing shadow cameras [75]. These systems are capable of producing DNI maps for a land area of 4 km^2 with a temporal resolution of 15–30 s and a spatial resolution of up to 5 m $\times$ 5 m. Satellite derived data produce much lower temporal and spatial resolutions. This does not match the necessities of dynamic plant controllers, and hence is not suitable for the application [48]. More information about the operation of the camera systems can be found in [47, 62, 87] for the cloud camera systems and in [45] for the shadow camera systems.

We have been provided with numerous DNI maps measured at the Plataforma Solar d'Almería in southern Spain. The maps data are spatially and temporally interpolated to provide input matrices to VSF, such that an effective irradiance value is given for each collector at each time step. The spatial interpolation process is done using the intrinsic MATLAB® function `interp2` which performs linear approximation from the surrounding points in a two dimensional mesh. The temporal interpolation depends on linear approximation between the measurement points. More information can be found in [3], where the processes are more thoroughly described.

To test the different controllers in various weather conditions, we identified five irradiation categories. The identification process is based on visual inspection of the the provided DNI maps. The shape and travel of the cloud shading on the field are observed. Table 2.1 shows the main categories identified with example irradiance maps for each category in Table 2.2. The maps shown are interpolated on a full-scale exemplary solar field resembling

La Africana parabolic trough solar power plant near Posadas in the province of Córdoba in southern Spain [63].

Table 2.1. DNI categories classified for this work (Abb.: Abbreviation)

	Category	Abb.	Definition
1.	Clear-sky	CS	no spatial variability on the field
2.	Random-quick	RQ	high-frequency, low-amplitude disturbances, corresponding mainly to cirrus clouds
3.	Thick, small	ThkS	strong localized disturbances that shade a small portion of the solar field
4.	Thick, large	ThkL	large cloud fronts
5.	Clouds with gaps	ThkH	dense large clouds with some gaps representing very high spacial variability on the solar field

Table 2.2. Examples for the DNI categories classified for this work.

1. Clear-sky (CS)	2. Random quick clouds (RQ)
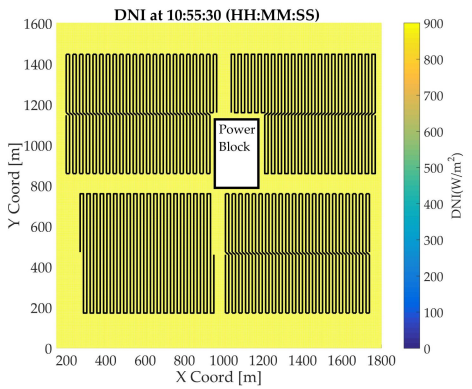	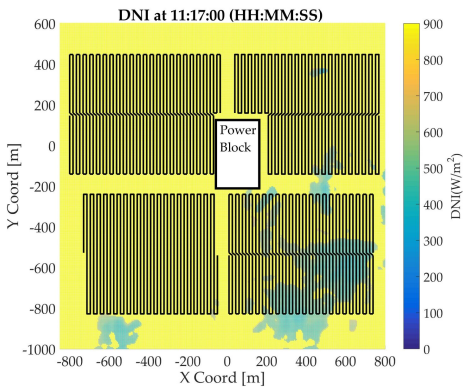
3. Small thick clouds (ThkS)	**4. Large thick clouds (ThkL)**
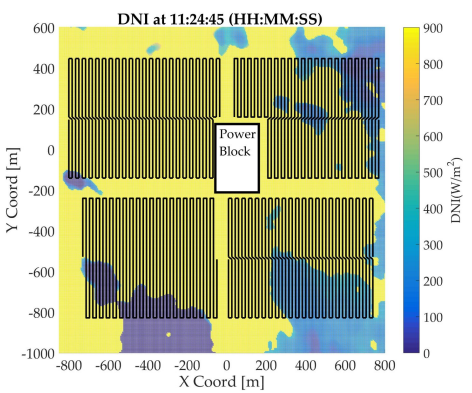	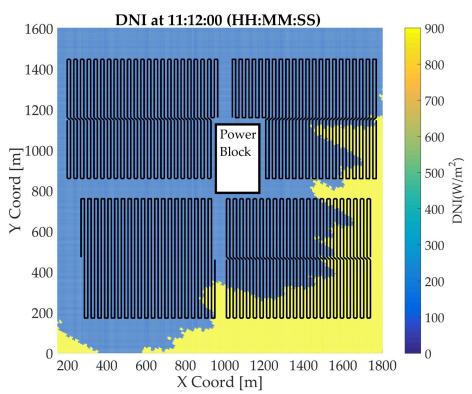
5. Thick clouds with gaps (ThkH)	
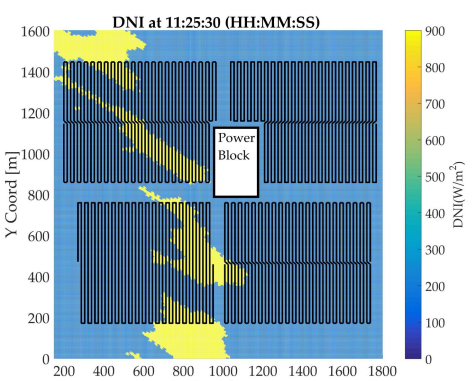	

3 MODEL VALIDATION

The model needs to represent the simulated system with sufficient accuracy to be useful for any of the applications mentioned in Chapter 1. In this chapter, the validation methods used during the different phases of the model development are discussed. Firstly, the validation cases for the initial implementation of the hydraulic solver in MATLAB® are shown. Secondly, the thermal model for a single loop is validated against an analytical model and another simulation tool developed at the DLR, as well as single loop measurements from Andasol-III power plant. Finally, some validation cases of the simulation tool against real operational data of Andasol-III power plant are shown and discussed.

3.1 HYDRAULIC PART VALIDATION

To validate the static hydraulic part, the results are compared with a model built in EBSILON® Professional using the solar thermal component library described in [36]. EBSILON® Professional is a static commercial thermodynamic cycle simulation tool. It uses some control schemes to compute the required pump pressure and the corresponding pressure losses in the pipes to achieve the flow needed for a specific outlet temperature set-point according to the given solar condition. In order to make the mass flow rate equal in all loops, throttling valves are added at the entrance of each loop to compensate for the pressure lost in the header pipes, Δp_h. For the validation, the required pump pressure computed by the Ebsilon model is input to the hydraulic solver, then the mass flow is compared to the one in Ebsilon. The average temperatures in the loops are used to compute all the physical properties needed. In addition, the pressure drop at the throttling valves is compared for a given pump pressure. Table 3.1 shows the input parameters for the test cases used for validation.

The headers are cascaded, such that the first header closest to the pump has a diameter of $D_{h,max}$, that linearly decreases to the diameter of the last header of $D_{h,min}$. Two different sets of header diameters are used to vary the net pressure lost in the system, and also the valve setting.

A test solar field of 4 loops is simulated and the DNI is varied in the Ebsilon model. The corresponding pressure loss in the system, as well as the mass flow rate is plotted and compared. Figure 3.1 shows the resulting total flow rate from the hydraulic model for the low header pressure loss case. The percentage difference is also plotted showing a constant relative error of 0.2 % and good agreement between both models. Figure 3.2 shows the calculated pressure loss in each loop valve to attain equal mass flow in the parallel loops

Table 3.1. Parameters for validation of the hydraulic solver.

Δp_h Parameter	Low	High	Units
$D_{h,max}$	200	30	mm
$D_{h,min}$	170	24	mm
l_h	18	36	m
D_{abs}	65.4		mm
l_{abs}	600		m
T_{in}	293		°C
ΔT_{loop}	100		°C

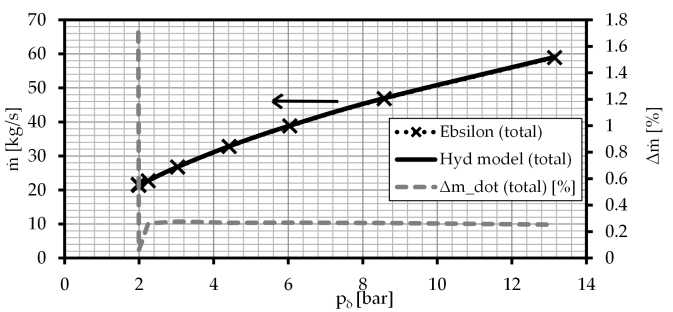

Figure 3.1. Comparison of mass flow rates between Ebsilon model and the hydraulic model for 4 loops and low Δp_h.

in the field at 2 different pump pressures. The results from both models show very good agreement with a normalized root mean square error (nRMSE) in the loops of 0.67 % for the mass flow rates and approximately 0.52 % for the pressure loss in the throttling valves.

Likewise, the results of a second test case with significantly higher pressure drop in the header pipes are shown in Figures 3.3 and 3.4. Both models show very good agreement with nRMSE of 0.07 % for the mass flow rates and approximately 0.1 % for the pressure loss in the throttling valves. This second test case is performed to test the proper functionality of throttling. The chosen pressure differences and mass flows are to validate the model under a broad range of conditions. This shows that the model is able to set the throttling valves appropriately to balance the flow in the parallel loops.

3.2 SINGLE LOOP MODEL VALIDATION

In this section, some validation test cases for the thermal part of the model are presented. A single loop is simulated and the results compared with an analytical model, another validated simulation tool and field data from a commercial power plant.

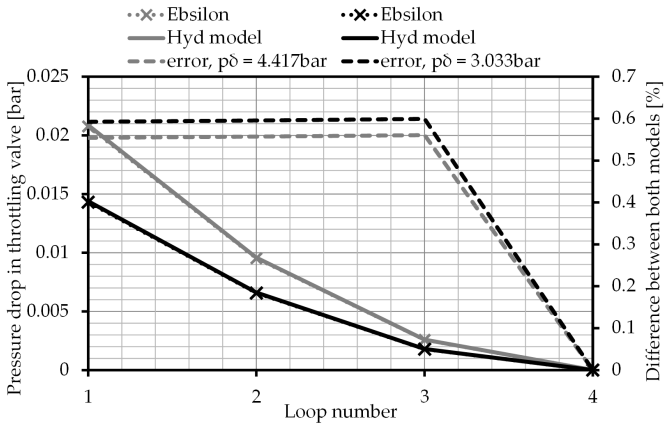

Figure 3.2. Pressure loss in loop valves with low Δp_h.

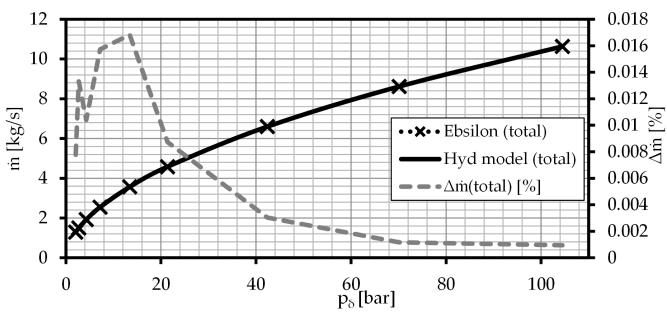

Figure 3.3. Comparison of mass flow rates between Ebsilon model and the hydraulic model for 4 loops and high Δp_h.

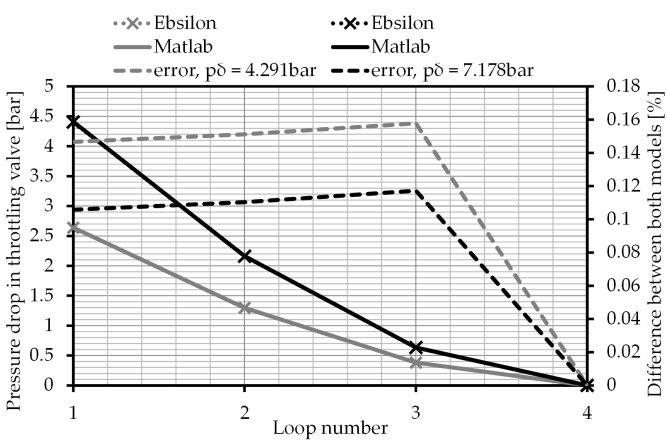

Figure 3.4. Pressure loss in loop valves with high Δp_h.

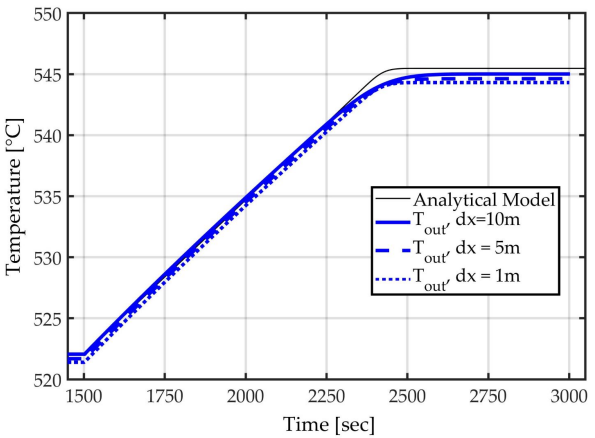

Figure 3.5. Dynamic response of the outlet temperature due to a step in G_{eff} from 850 to 935 $W\,m^{-2}$.

3.2.1 Analytical system response

To validate the dynamic system response of the thermal model, the temperature response to a step in the irradiation is compared against the analytical response using the κ_D-model described in [33, 70]. The κ_D-model uses the Laplace transformation of the physical differential equations to calculate the spatial and temporal transfer functions. The model considers single-phase flow with constant properties along the receiver tube. Moreover, the external heat source is assumed to be homogeneous along the length of the absorber tube. Figure 3.5 shows the response of the pipe outlet temperature to a step in effective solar irradiance from 850 $W\,m^{-2}$ to 935 $W\,m^{-2}$. The pipe is 1000 m long and 66 mm in diameter. The HTF is molten salt with a density of 1900 $kg\,m^{-3}$ and specific heat capacity of approximately 1500 $J\,kg^{-1}\,K^{-1}$. The mass flow rate is kept constant at 8 $kg\,s^{-1}$ and the convective heat transfer coefficient is 2390 $W\,m^{-2}\,K^{-1}$.

The model shows good agreement with the analytical model with spatial discretization steps of up to 10 m. The dynamic behaviour, represented by the response time, as well as the magnitude of temperature variation, resembles that of the analytically predicted one.

3.2.2 Comparison with simulation model

In this section, the thermal part of the model is validated against a transient model developed at the German Aerospace Center (DLR) for a single loop [11]. Figure 3.6 shows the results of a 1000 m long loop of Schott® PTR70 receivers with MS as HTF as an example. The inlet mass flow rate is set to a constant value throughout the simulation at 7.3 $kg\,s^{-1}$. The incident DNI is varied as shown by the red dashed line in the figure. The outlet and

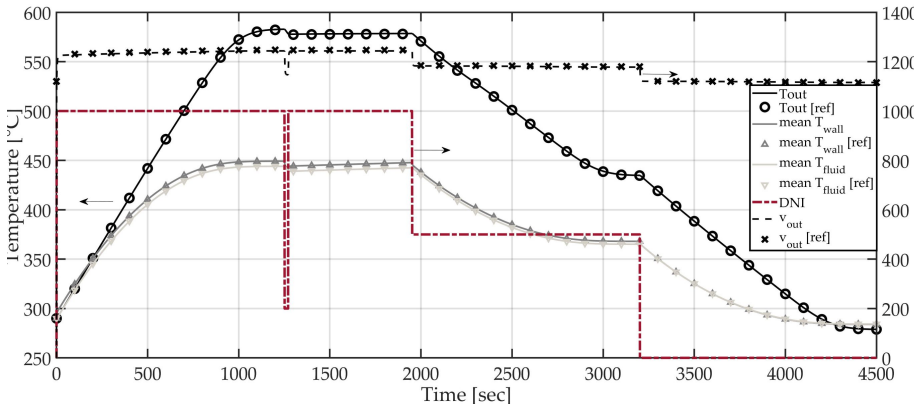

Figure 3.6. Comparison between the thermal model and the reference model (ref) described in [11].

mean fluid temperatures, as well as the mean wall temperatures, are compared for both models. The results show resemblance with respect to the transient response of the system to time-varying irradiation condition. The outlet velocity also changes with temperature as the fluid density varies while the mass flow is kept constant.

3.2.3 Comparison with single loop measurements

The model was also used to simulate a test campaign conducted by a research group at the Institute of Solar Research of the DLR on a single parabolic trough loop. The test took place in Andasol-III with loops of 600 m length and thermal oil as the HTF. The group measured the inlet and outlet temperatures, as well as the temperature, flow rate and DNI in the middle of the loop (cross-over pipe). The overall cleanliness was obtained via reflectivity measurements on all 48 collector modules of the loop. For the simulation, the inlet temperature, inlet flow rate and DNI were used as input boundary conditions for each time step. The collector focus was also considered by comparing the sun inclination angle with the collector tracking angle.

Figure 3.7 shows the outlet and cross-over pipe temperature responses to the measured DNI and flow rate for 2 measurement days, 22. and 23.04.2015 in Figures 3.7a and 3.7b, respectively. The results show very good agreement with the measured data; all transient responses are accurately captured along the length of the loop. Discrepancies in the temperatures at the start of the simulation in Figure 3.7a are due to improper initialization of the linear temperature distribution since the initial temperature distribution along the whole loop is not measured. However, the outlet temperatures are overestimated by 1 % to 6 % for the second day. Possible sources of errors include inaccurate representation of the collector optical efficiency as function of the collector angle as discussed in Section 3.3.

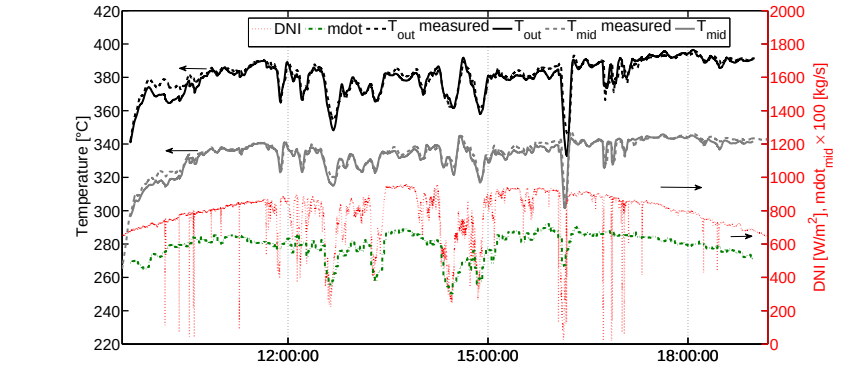

(a) 22.04.2015

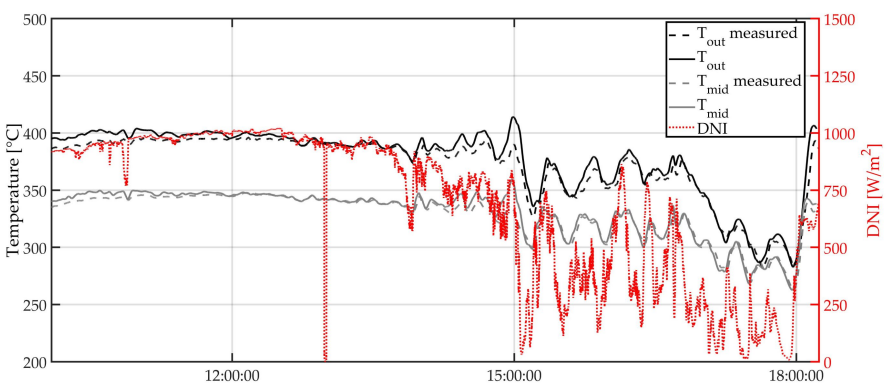

(b) 23.04.2015

Figure 3.7. Comparison between the thermal model and measured loop data in Andasol-III.

To summarize the previous sections, the building blocks of the VSF tool, namely the hydraulic and thermal parts, were validated using different analytical, numerical and experimental methods. The model shows very good agreement with the validated models and with experimental data. The validation cases also showed some issues with the assumptions used for computing optical efficiencies when the collectors are defocused. The validation test cases for the whole solar field model with operational solar field data is presented in the next section.

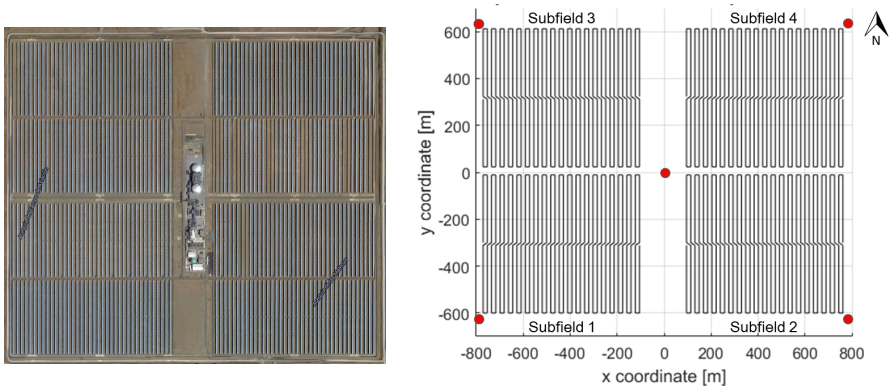

Figure 3.8. [Left] Satellite image of Andasol-III power plant [Map data: Google, Inst. Geogr. Nacional]. [Right] Computational domain (header pipes not shown). The red dots indicate the approximate locations of the weather stations.

3.3 VALIDATION AGAINST COMMERCIAL POWER PLANT

The next step is to validate the model using power plant operation data, such that the coupling of both parts and the fluid mixing could be verified. Hence, we developed a collaboration with Marquesado Solar S.L., the operators of Andasol-III (AS-3) solar thermal power plant in southern Spain [64], to test the accuracy and validity of the simulation tool. Marquesado Solar provided operational data of a few days in Spring 2015 that we used to simulate the power plant and compared them with the simulated plant response. The validation test cases are published in [57] and are summarized in this section.

3.3.1 Comparison data and model input

Andasol-III is designed to provide 50 MW of electric power. Its collector field has 4 subfields with 38 loops per subfield and thermal oil is the HTF. Figure 3.8 shows a satellite image of the power plant and the simulated computational domain. The plant has two tanks filled with MS that are used for thermal energy storage. However, the storage tanks, as well as the power block, are not simulated within the scope of these validation cases.

Table 3.2 shows a list of the measurement signals from the solar power plant that are used as input for VSF. Marquesado Solar provided plant designs and pipe geometries that were used to design the simulation cases. In addition, information about the type of collectors, absorbers and header pipe insulations, as well as the piping materials, were provided. Since the solar field inlet temperature is not measured, we used the temperature of the fluid at the inlet of each subfield to compute it by considering the travel time and heat losses in

Table 3.2. Measured data from AS-3 used as input parameters for VSF.

	Parameter	Comment
1	Field layout	including all pipe diameters and lengths
2	Subfield inlet temperatures	also used to compute the solar field inlet temperature
3	Pressure difference between the inlet and outlet of the solar field. Used to compute the flow rates in the field	
4	SCA tracking angle	used to compute the collector focusing (a factor from 0 to 1 depending on the sun azimuth and elevation)
5	DNI	interpolated to each collector using measurements from 5 weather stations

the main headers. We also used the measured pressure difference between the entrance of the cold header and the exit of the hot header as input for VSF to drive the fluid through the solar field. To input the focus control of the collectors, I used the measured collector angles and compared them to the theoretical sun position to compute the focus factor of each single collector according to collector acceptance angle relations as will be described in Section 3.3.4. Any missing time stamps in the raw data were temporally interpolated.

The DNI measurements from weather stations in the power plant were also provided. AS-3 is equipped with five weather stations; there is one weather station at each corner of the field and one at the power block. To calculate an estimate of the solar irradiance on a collector in the solar field, the raw DNI data was preprocessed by spatial linear interpolation of the three nearest weather stations to the subfield containing the collector. For example, collectors in subfield 1 in Figure 3.8 use measurements from the weather stations at the power block, and in the north-western and south-western weather stations. The advantage gained from this method is the consideration of large clouds that cover significant parts of a subfield or the solar field in the simulation model. However, this caused some over-estimation of the cloud sizes as discussed in Section 3.3.4.

With regard to the hydraulic balancing of the plant, there was no information provided concerning the settings of the loop valves. Therefore, static loop valve settings are computed using a prescribed nominal operation condition including nominal DNI and design inlet and outlet temperatures. The needed mass flow rate in each loop is then computed and, accordingly, the pressure losses in the headers that need to be compensated by the loop valves. The corresponding valve opening is then computed as illustrated in Chapter 2 and fixed throughout the simulation.

The output of VSF is compared against temperature and flow rate measurement signals from the power plant. The main temperature signals used for the validation cases are temperatures at the loop inlets and outlets, subfields inlets and outlets, and solar field inlet and outlet. However, temperature measurements provided by Marquesado Solar are plotted in normalized form as requested by the plant operators. In order to prove the validity of the comparison, the root mean square error (RMSE) of the simulations is computed and noted on the corresponding figures. Flow measurements were only provided for the subfield inlets. In addition, we used the same data from a measurement campaign performed at the AS-3 power plant on a single loop. This also included flow rate measurements in the middle of the loop and more precise temperature measurements [58].

Firstly, a grid convergence study is performed for a simple test case. Then a test case simulating plant normal operation during a few transients is demonstrated. Finally, some discrepancies due to local DNI transients and assumptions of the optical efficiency are discussed. There are also more test cases presented and discussed in [57]. Simulation runs for the whole solar field take 1 % of the simulated real time, i.e. 5 hours take VSF around 3 min of computation time.

3.3.2 Grid convergence

A grid convergence study has been performed to study the effect of the number of discretization cells per loop on the accuracy of the results. For common simulation tools for parabolic trough solar fields running with single-phase HTFs, a very wide range of discretization element lengths of about 10 m to 150 m are used. For the grid study, we used the Andasol-III setup to simulate a simple test case with DNI shown in Figure 3.9a.

The loops of 600 m length are discretized into 8 to 60 elements, making element lengths of 75 m to 10 m. Fewer number of elements lead to less computation time, while loosing details about the spatial variability of the irradiance. Also larger discretization cells increase the numerical errors when solving the differential equations. Figure 3.9b shows the normalized RMSE (nRMSE) of the field outlet temperature and mass flow rate, with the case of 60 elements used as reference. The figure shows a decay of the error as the number of cells per loop increases. The decrease becomes less significant as the number of cells are more than 40 cells per loop. Hence, all simulations presented in this work use 48 to 52 cells per loop to discretize the loops resulting in element lengths between 11.5 m and 12.5 m in the absorber pipes. The analytical model presented in Section 3.2.1 also shows good agreement for this length. The element length is also suitable for DNI maps, which are typically resolved by 5 $\mathrm{m} \times 5\ \mathrm{m}$ and 10 $\mathrm{m} \times 10\ \mathrm{m}$ grids.

3.3.3 Plant operation data

Figure 3.10 shows the pump control on the field and the corresponding computed and measured volume flow rates in subfield 3 as an example. In addition, the percentage of

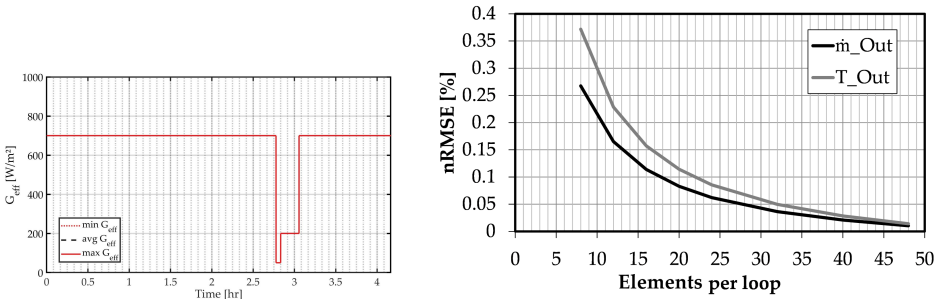

(a) G_{eff} **(b)** nRMSE for different number of cells.

Figure 3.9. Grid convergence study.

focused collectors is plotted against time. Only one subfield is plotted as a representative to improve the clarity of the graphs. In this case, the pump differential pressure at the PB is input to VSF. Using this data, VSF computes the flow rate in each pipe in the field according to its hydraulic resistance. The comparison between the computed and measured flow rates in subfield 3 is shown in the figure. VSF can follow the transient behaviour of the solar field with a nearly constant deviation of $\approx 5\,\%$ at pressure values above $6\,\mathrm{bar}$. The deviation is much lower at lower pressure and flow rates, for example between 14:15 and 15:00. This same behaviour is observed in different test cases and could be a result of the calibration of the measurement equipment or geometry specifics that are not apparent in the plant designs provided to the simulation tool. In addition, the loop valve settings and characteristics in VSF are based on an assumed nominal operation of the field and orifices which might be different from the actual setting. However, the effect of the field control through varying the pump pressure in response to changes in DNI to alter the fluid mass flow rate could be represented by VSF. Also important to note is that most collectors are in focus within the investigated period as shown by the purple line in the figure. This eliminates the effects of discrepancies resulting from the computation of optical efficiencies as pointed out later in Section 3.3.4.

Figure 3.11 shows the comparison between computed and measured temperatures during normal operation of the power plant and a few clouds passing over the field. The three DNI measurement stations are the ones interpolated to the discretized computational domain. Using the flow boundary conditions in the loops and header pipes, and the incident DNI, VSF computes the heat transfer to and from the HTF in each pipe section. Then the fluid is mixed at the pipe junctions. The subfield temperatures in Figure 3.11 show very good agreement between the VSF results and the measurements with a RMSE of $4.32\,^{\circ}\mathrm{C}$ for the subfield temperatures and $2.75\,^{\circ}\mathrm{C}$ for the whole solar field outlet temperature within the plotted period. There are some small deviations, for example at 13:30 and 16:15 mainly due to the inaccurate DNI interpolation from only 3 weather stations when compared to the actual irradiation state in the field as will be discussed later. In Figure 3.11, 3–5 min

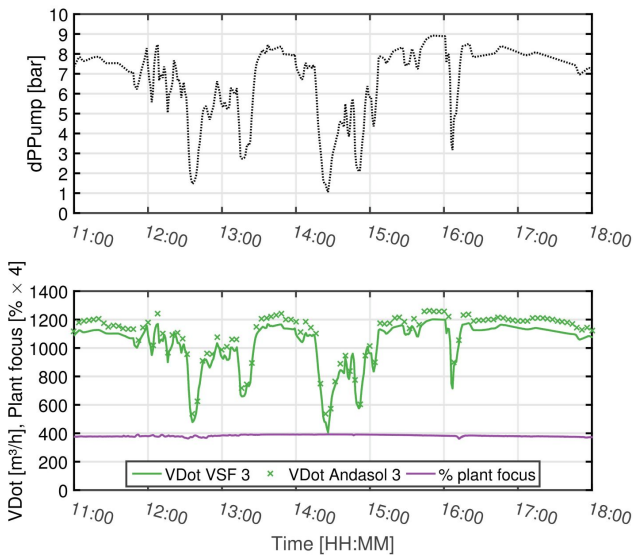

Figure 3.10. Comparison with AS-3 operation data - [Top] Pump differential pressure. [Bottom] Fluid volume flow rate in subfield 3 and total solar field focus.

time shift could be observed throughout the day. This time shift is noticed for all 4 subfield outlet temperatures, however the loop temperatures do not show such shifts as could be shown in Figure 3.12. The solar field outlet temperature also shows shorter and more irregular delays due to the mixing of all the HTF from all the subfields. Consequently, the time shifts are considered to result from deviation of pipe dimensions and from not knowing the exact location of the temperature sensors measuring the subfield outlet temperature in the header pipe.

Figure 3.12 shows the model results compared with the single loop measurements performed by DLR in AS-3 on the same simulated day. The measurements are performed on one loop only with more equipment than already installed in the field. The figure shows the comparison of the inlet, middle (cross-over) and outlet temperatures of this investigated loop. In addition, the flow rate in the loop has been measured and could be compared with the simulated mass flow distribution by VSF. As shown in the figure, the temperatures could be very accurately simulated. The loop inlet temperatures show a small time shift, which could be attributed to the deviations of the location of the measurement point since it is smeared out for the middle and outlet temperatures. Small deviations due to local cloud passages could be seen at 16:10 and around 17:00. As will be discussed in Section 3.3.4, smaller clouds that are registered by only one weather station would have an effect on one or more subfields in the simulation, causing an overestimation of the size of the cloud and lower temperatures in VSF. When observing the outlet temperatures of the different

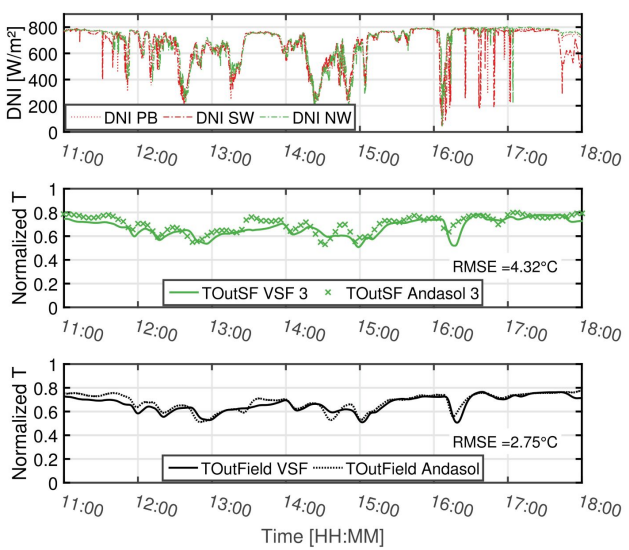

Figure 3.11. Comparison with AS-3 operation data - [Top] DNI values at the 3 stations around subfield 3. [Middle] Normalized subfield outlet temperature. [Bottom] Normalized field outlet temperature. Normalized temperature scaling = 1:85K.

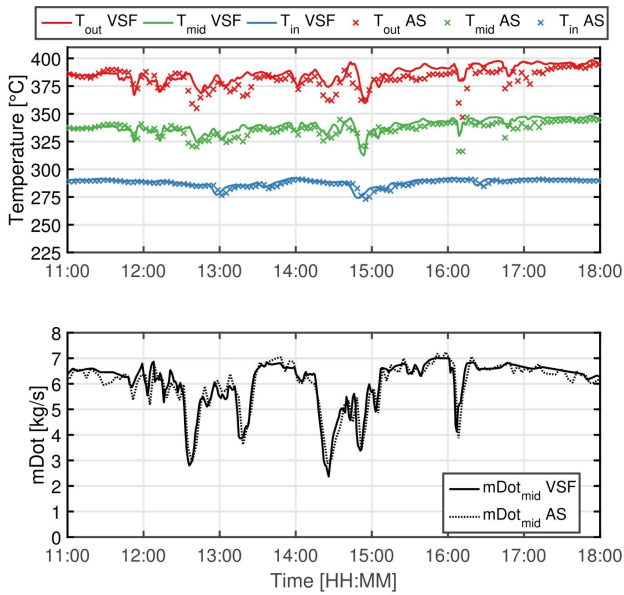

Figure 3.12. Comparison between VSF (solid lines) and DLR measurements of 1 loop (AS, crosses or dashed lines). [Top] Loop inlet, middle and outlet temperatures. [Bottom] Mass flow rate in the middle of the loop.

loops between 16:00 and 16:30, higher temperature drops were measured at the loops on the southern side of the subfield than at the ones closer to the power block. This shows that the cloud passage is localized and not possible to detect by the measurement equipment available on the field.

In summary, the results show that VSF can accurately predict the thermal and hydraulic behaviour of the power plant with slight differences that will be discussed in in the next section. The uncertainty in some input values like the loop valve settings and the errors in pump pressure gauges cause deviations of the model results from the plant data. In addition, the lack of spatially resolved DNI data causes inaccurate input to VSF.

3.3.4 Validation challenges

In this section, two sources of discrepancies in the validation cases are discussed. First, the effect of the spatial resolution of the DNI measurements on the model results are shown. Then the sensitivity of results to collector acceptance angle curve is outlined. In the validation cases of AS-3, DNI measurements from 5 weather stations are used. Since the distances between the weather stations are approximately 600 m in each direction, some measurements could be misinterpreted. For example, some smaller clouds could pass over the loops but do not shade the weather stations and thus are not recorded in the measurements.

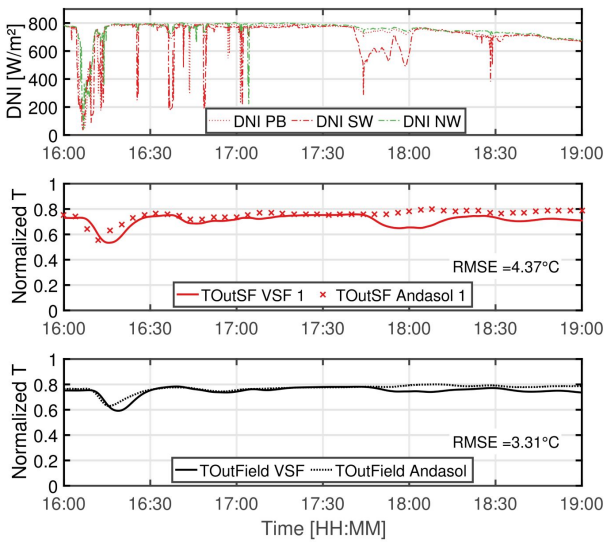

Figure 3.13. Discrepancies in subfield normalized outlet temperatures due to the lack of spatially resolved DNI data. Normalized temperature scaling = 1:115K.

On the other hand, some clouds could only shade the weather stations and a small number of loops, while the drop in DNI measurements affects all the loops in the simulation due to the interpolation assumptions.

Figure 3.13 shows a typical example of that case such that a drop in DNI is registered between 17:35 and 18:00 by the south-western (SW) weather station. This drop affects the interpolation of DNI values for all the loops in subfield 1, as shown in Figure 3.14. It results in a drop in the calculated outlet temperature, even though no temperature drop is registered in the plant logging information and no other reason could be identified for such temperature drops. Thus, it can be concluded that the difference is due to a variation in effective heat input.

Consequently, we observe that the spatial distribution of the heat input, that is the DNI, has an impact on the temperatures in the field. Hence, studies focusing on the details of temperature distribution over the field and validation with operational data are only possible for clear-sky situations or with measurement devices that provide spatial resolution of DNI, such as the nowcasting systems discussed in Section 2.3.2 and Chapter 4.

As also discussed in Section 2.3.2, the optical efficiency of the SCAs depend on the collector deviation angle and the shape of the acceptance angle curve. In the following test case, the effect of varying the acceptance angle curve is shown. As described in [41], the acceptance angle curve represents the focusing of the collector in terms of the deviation of the collector solar tracking angle from the sun angle. The shape of the curve depends

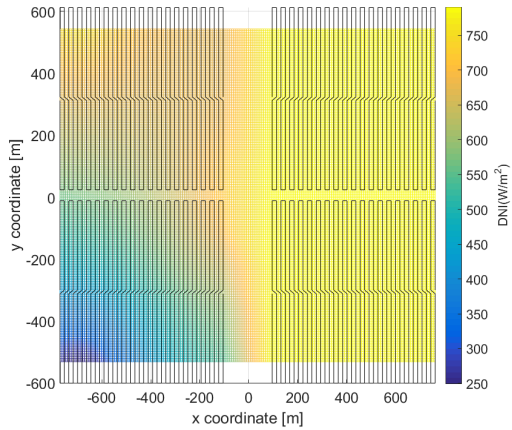

Figure 3.14. Interpolation of the instantaneous DNI measurements on the computational grid at 17:44 as used for the simulation.

on the mirror geometry and the width of the collector tube. This has a significant impact on the computational results, especially when there is a lot of collector partial defocusing taking place. Curve 1 in Figure 3.15 shows an example as given in [41]; however, the exact shape of the curves are prone to a lot of uncertainties. Unfortunately, there is information regarding the collectors used to compute this curve nor the exact acceptance angle curves for the collectors in AS-3. VSF compares the measured collector tracking angle, α_{coll}, to the theoretical tracking angle, ϕ_{sun} computed using the sun azimuth and elevation, to compute $\Delta Angle_{coll}$.

A narrower acceptance angle curve variation is plotted as curve 2 in Figure 3.15 and the resulting loop outlet temperatures for both curves are plotted in Figure 3.16. Also the percentage focus of all the collectors in the loop is shown using the purple solid line. By using the narrower curve, we could reduce the partial focus of the four collectors in the loop by approximately 12 % when we compare the percentage focus curves in both cases. Consequently, we could get rid of the temperature overshoots in Figure 3.16 during strong defocusing cycles between 18:45 and 19:50, such that the RMSE dropped from 14.4 °C to 9.71 °C in the first and the second cases, respectively. However, both curves represent approximations to the real collector behaviour and more representative curves are needed to ensure the correctness of the results in cases with the defocusing cycles.

3.4 SUMMARY AND CONCLUSION

In this chapter different validation methods throughout the development phase of the simulation tool have been presented. The first prototype of the hydraulic part showed good

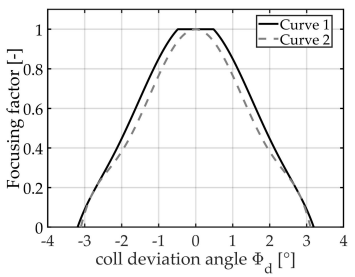

Figure 3.15. Acceptance angle curve examples. On the x-axis is the difference between the measured collector tracking angle and the theoretical one.

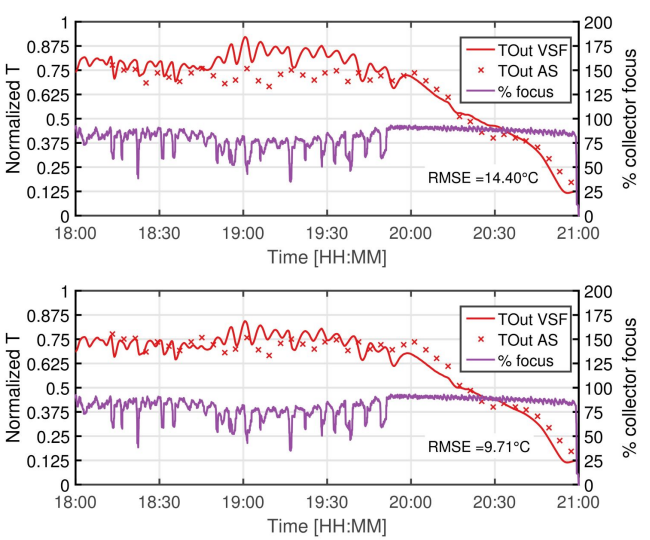

Figure 3.16. Normalized loop outlet temperatures using different acceptance angle curves. Purple: Focus percentage. [Top] Based on curve 1 in Fig.3.15. [Bottom] Based on curve 2. Normalized temperature scaling = 1:190K.

agreement of the mass distribution and pressure loss in the valves with models in EBSILON® Professional. Then the thermal part was validated using analytical, numerical and experimental methods. For all test cases, the model showed very good agreement with the results.

Then, the final implementation of the whole tool is validated using full power plant operational data. VSF successfully computes the mass flow distribution in the field and in single loops according to the thermal condition using the differential pressure between the solar field inlet and outlet. The computed flow distribution is then used as flow boundary condition to compute the heat transfer and the resulting temperatures. Then, the fluid is propagated and mixed from all subfields to the field outlet taking into account the travel time in the header pipes. The results show very good agreement with the plant data with slight discrepancies observed in the through-put time of the headers, causing a time shift. It was also shown that the results depend on the quality of the DNI measurements and whether spatially resolved DNI data could be obtained or not, especially during transient conditions. Finally, the sensitivity of the results to the collector acceptance angle curves has been shown.

Generally, the results prove that VSF is a reliable tool and can be used to investigate different applications of interest for research and industry to optimize the energy output of the solar field and enhance field control as will be shown in the following chapters.

4 STATE OF THE ART SOLAR FIELD CONTROL

The control of commercial solar fields is a challenging task as the controllers need to deal with various interacting systems. For example, the loop temperatures, that are regulated by the local SCA controllers, are affected by the flow rate passing in the absorber pipes, which is mainly regulated by the main pumps controller. The controllers need to also take care of the hazard- and fail-safe operation of the power plant, hence sometimes sacrificing optimal operation for safety. By having an accurate and detailed simulation model for the system, we could test solar field controllers and evaluate the performance under different operation conditions effectively and efficiently. In this chapter, the implementation of common state-of-the-art controllers described in literature is discussed. Practical experience of those controllers is also collected from engineers in power plants operated by industrial partners we collaborate with. In addition, a systematic approach for testing the performance of these implementations under different operation conditions is thoroughly described. Such approaches can significantly contribute to improving the available solar field controllers and to developing novel control concepts as will be outlined in the next chapter.

Solar field control is an established topic in literature and in practice. Different aspects of common controllers in solar fields operating with single-phase HTF, commonly thermal oils, are discussed in [15, 43, 95]. Most recent research in solar field control focus on direct steam generation power plants, where controlling both steam pressure and temperatures are critical especially during transient cloud passages [24]. Thus, there has not been much advancement in control of solar fields with single-phase HTF recently. Numerous control concepts are compiled in [15] and more advanced ones, such as model-predictive control, in [16]. However, to our knowledge, most of those advanced concepts did not find their way to be implemented and tested in real systems. The main flow controllers in the investigated power plants, rather, rely on control concepts like the ones described in [95]. The main goal of the controllers is to achieve stable operation of the solar field while maximizing its thermal energy yield.

Despite this, the implemented controllers fail to perform well during spatially-varying transient processes like passing clouds. It has been reported that the solar field operators often prefer to manual intervention during cloud passages to avoid excessive defocusing and to stabilize the field outlet temperature. That is to avoid thermally stressing the heat exchangers and other components in the power block.

The controller components in this work are described in Section 4.1. The aim is not to implement a fully functioning control concept that would outperform and replace state-of-the-art controllers. Rather, the goal is to show that VSF can be used as a platform to help

users develop, test and compare different control concepts. It also offers the possibility to try novel concepts that could offer significant advancement in parabolic trough field control.

4.1 CONTROL ELEMENTS

The control system in VSF, is adapted from control systems described in literature and from common control concepts in some commercial solar fields. It is divided to local collector focus controllers in the SCAs and a field main flow controller. In this section, the basic principles of how both controllers are implemented in VSF are described.

4.1.1 Loop focus controller

The main task of a loop focus controller is to ensure that the collectors are tracking the sun. It also limits the temperature of the HTF to guarantee safe operation as described by the manufacturers. The manipulated variable is the deviation of the collector from the tracking angle, Φ_d. The controlled variable is the HTF temperature at the center of the collector, T_{SCA}. In principle, this should be guaranteed by providing the suitable mass flow rate in the loops. However, this is not the case in real plant operation due to the many uncertainties and inaccuracies of real systems as will be discussed further in Section 4.1.2. Moreover, as clouds pass over the field, the plant is subject to transient conditions, where the different loops are exposed to varying energy input due to partial shading of the clouds. Hence, the loop focus control depends on local temperatures measured in the SCAs. This includes a proportional-integral (PI) temperature feedback (FB) controller that manipulates the collector angle to ensure that the collector temperatures are within the set-points. It is also equipped with a built-in emergency controller that would put the collectors totally out of focus in case the temperature limit of the fluid is exceeded. Both parts are described below.

Local PI-controllers

Based on temperature measurements in the middle of the SCA, as well as the loop outlet temperatures, as shown in Figure 4.1a, the controller manipulates the deviation angle of the SCA from the sun, Φ_d as in Figure 4.1b. The four local controllers work independently such that collector-wise focusing and defocusing strategies are achieved [89].

The control diagram is shown in Figure 4.2. The temperature in the middle of the SCA, T_{SCA}, is compared to the set-point temperature for the collector, $T_{SP,OK}$. The set-points depend on the inlet temperature of each loop and are set such that a linear temperature rise from $T_{loop,in}$ to $T_{f,OK}$ in the loop, as shown in Figure 4.3, is assumed. $T_{f,OK}$ is the safe operation temperature of the HTF.

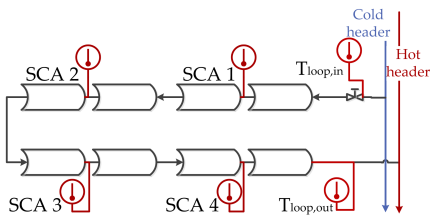

(a) Input temperature measurements in each SCA controller.

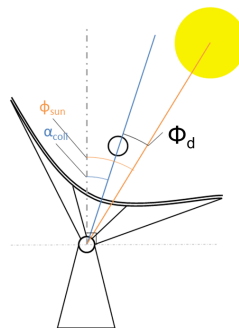

(b) Front view of an SCA showing sun and collector angles. Φ_d is the controller output.

Figure 4.1. A schematic of the input and output of the local SCA controllers in a loop.

The PI-controller works on eliminating the temperature error, $e_T(t)$, by computing the needed SCA deviation angle, Φ_d. Φ_d is thus computed as

$$\Phi_d = K_c e_T(t) + \frac{K_c}{T_i} \int e_T(t) dt \,, \tag{4.1}$$

where K_c and $\frac{K_c}{T_i}$ represent the proportional and integral gains, respectively. These controller gains are tuned using the first-order plus dead time (FOPDT) method.

System dynamics is studied by imposing a step disturbance in the controller output (CO), which is the collector deviation angle in this case, and analysing the system response to this step, here the collector temperature as the process variable (PV). From the system response the process gain, K_p, time constant, T_p, and process dead time, θ_p, are determined and used to compute the controller gains as described in [76] as

$$K_c = \frac{1}{K_p} \frac{T_p}{(\theta_p + T_c)} \,. \tag{4.2}$$

T_c is the controller time constant and is equal to T_p multiplied by a factor varying from 0.1 to 10 for aggressive to conservative controller behaviour, respectively. The integral time constant, T_i, is equal to the process time constant, T_p which is discussed further in Section 4.2.3. K_p is the system process gain computed as

$$K_p = \frac{\Delta PV}{\Delta CO} \,. \tag{4.3}$$

The dead time, θ_p, is the time the system needs to show the first response to the disturbance. Table 4.1 lists the system parameters from studying typical operation conditions in the solar field. Δt_{sim} is the simulation time step. The controller output, Φ_d, is then sent to

Table 4.1. SCA focus controller parameters

	K_p [°C/deg]	T_p [s]	θ_p [s]
SCA 1	-8	5	Δt_{sim}
SCA 2	-9	5.2	Δt_{sim}
SCA 3	-10	5.4	Δt_{sim}
SCA 4	-11	5.6	Δt_{sim}

the actuator of the SCA and the solar collecting efficiency is computed from the acceptance angle curve as described in Section 2.3.2.

Anti-reset wind-up (ARW) is used to avoid the accumulation of the integral in case the CO reaches the operational limit and also to compensate for slow system dynamics. All feedback values are passed through a filter that disturbs the signal to emulate the uncertainties resulting from measurement equipment.

Overheat protection

SCAs are also equiped with safety mechanisms to force emergency defocus in case the fluid maximum operation temperature is reached. In VSF, a maximum temperature for each SCA is defined, such that the loop outlet temperature does not exceed 99.5 % of the maximum allowed temperature for the HTF as shown in Figure 4.3. If the collector temperature exceeds this value, the solar deviation angle is set to 4° behind the sun. For the last SCA in the loop, typically the forth one for typical commercial power plants, like Andasol-III, an additional defocus signal is issued if the loop outlet temperature exceeds the safety limit recommended by the manufacturer of the HTF.

4.1.2 Flow controller

The main solar field flow controller regulates the inlet mass flow to stabilize the solar field outlet temperature to a set-point at different weather conditions. Figure 4.4 shows the control block diagram for the different control elements involved. As described in Section 2.1, the flow in VSF is controlled by the differential pressure, p_δ, along the solar field. This is referred to as pump pressure within the text. The pump is assumed to follow a first-order dynamic behaviour with a time constant significantly faster than the system dynamics, typically 12 s [96]. The pump pressure is also bounded by minimum and maximum values that can be varied depending on the system design. The components of the control concept are described in detail below.

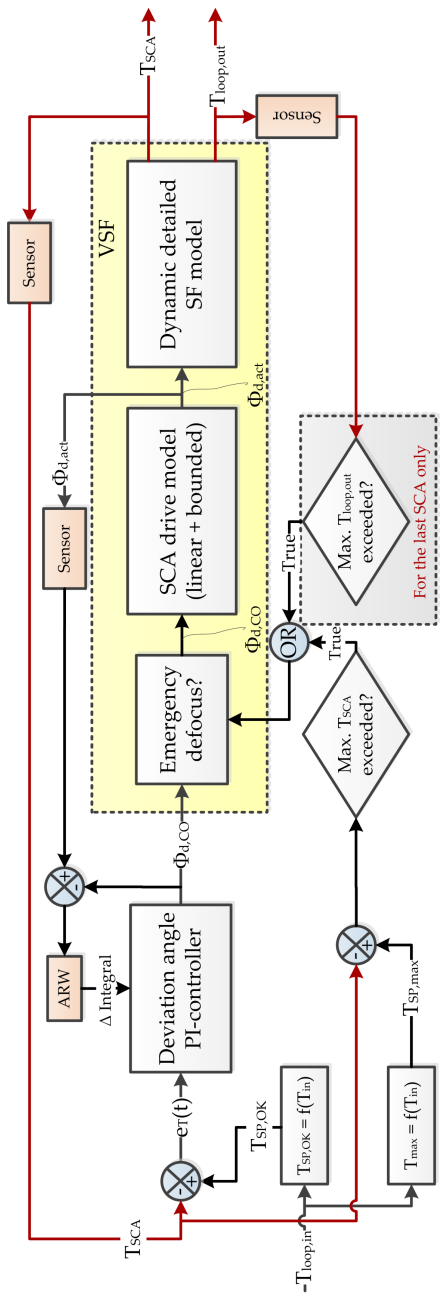

Figure 4.2. The control diagram for the local SCA focus controllers with a block only active for the last SCA in the loop. Emergency controllers are also shown.

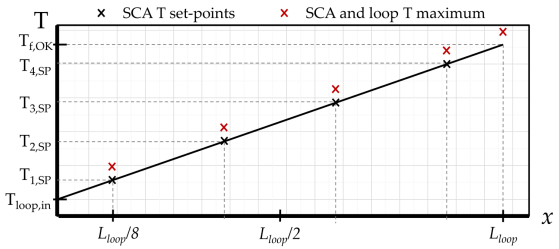

Figure 4.3. Set-point temperatures in the SCA controllers with linear temperature rise along the loop length, x.

Mass flow feed-forward

A feed-forward (FF) pump controller computes the required mass flow depending on the current solar energy incident on the field, $\dot{Q}_{sol}$. A simple plant performance model based on static energy balance in the whole field is used for the FF controller as described in [15, 24, 39]. The required mass flow rate in the solar field to achieve a prescribed temperature rise in the solar field, ΔT_{field}, is calculated as

$$\dot{m}_{Req} = \frac{\dot{Q}_{sol} - \dot{Q}_{loss}}{\bar{c}_p \cdot \Delta T_{field}} \,. \tag{4.4}$$

$\dot{Q}_{sol}$ is computed from average values of the available measurement points in the solar field. $\dot{Q}_{loss}$ is the total thermal losses in all the header pipes and loops in the field computed in the VSF. $\bar{c}_p$ is the average specific heat capacity integrated along the range of temperatures in the solar field.

To translate the required mass flow to a pressure drop along the hydraulic network, I use the hydraulic system curve. Figure 4.5 shows the system curves calculated for 2 commercial solar power plants with DOWTHERM® as the HTF, namely La Africana and Andasol-III. The system curves are produced by keeping a constant temperature in all the pipes and noting the total mass flow rate as the differential pressure is varied. The required pressure from the FF controller is thus computed as

$$p_{\delta,FF} = c_1(T)\dot{m}_{Req} + c_2(T)\dot{m}^2_{Req} \,, \tag{4.5}$$

with temperature-dependent coefficients, c_1 and c_2, which are polynomial-fitted from different simulated data. The differential pressure values are normalized so as not to disclose confidential data provided by out partners. The FF loop provides immediate response to global irradiance variations on the field.

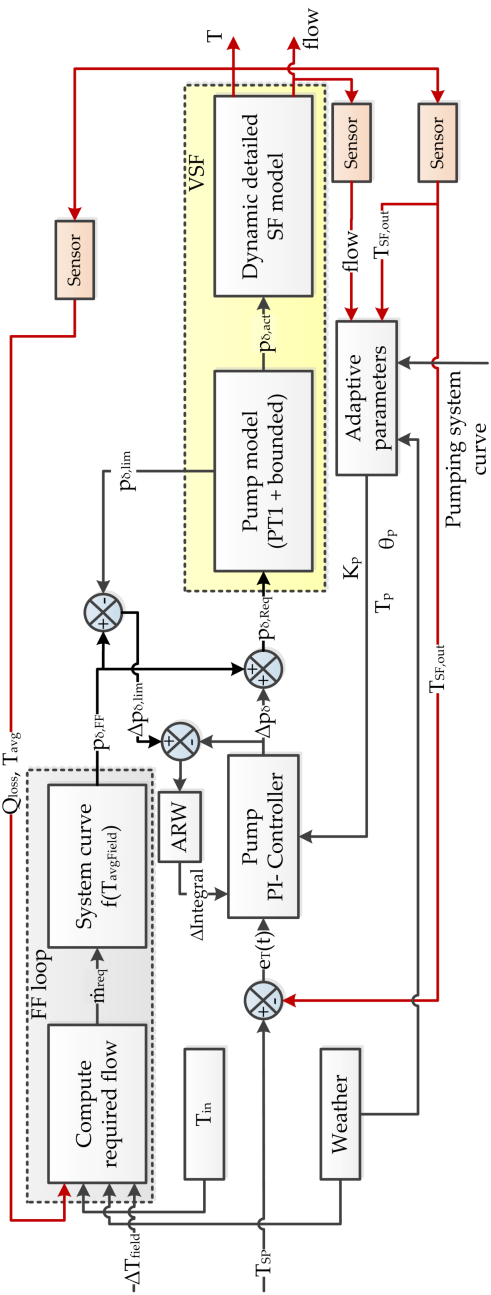

Figure 4.4. Control diagram for the basic flow controller implemented in VSF.

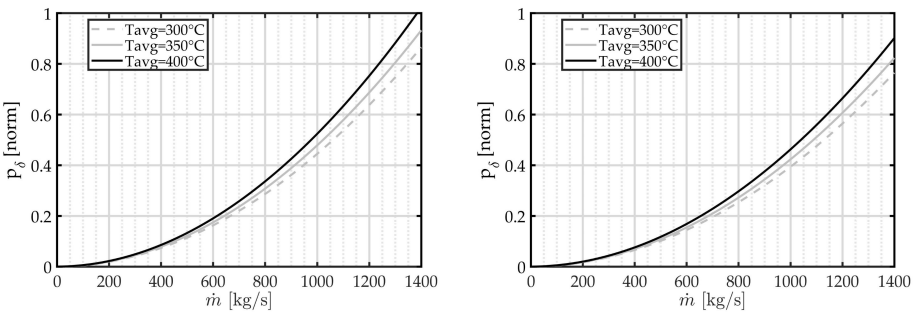

(a) La Africana **(b)** Andasol-III

Figure 4.5. System curve at different temperatures.

Field temperature feedback

The structure of the FF controller is very simplistic as it does not consider any spatial variation of the solar irradiance, since the energy input is based on the mean value of a few measurement points in the solar field. It also does not consider the thermal transient behaviour of the power plant and the thermal inertia in the pipes. Hence, a temperature feedback PI-controller is added to provide closed-loop system control. The controller corrects the pump pressure by a value, Δp_δ, depending on the solar field outlet temperature feedback as indicated in Figure 4.4. A temperature set-point is given to the controller and the deviation from it, $e_T(t)$, is computed. The change in pressure difference is given by the PI-controller as

$$\Delta p_\delta = K_c e_T(t) + \frac{K_c}{T_i} \int e_T(t) dt \,. \tag{4.6}$$

The controller tuning parameters, K_c and T_i, are adaptively computed based on the FOPDT method described in Section 4.1.1. They depend on the field condition, like solar energy input and losses, as well as the thermal inertia and fluid travel time in the pipes to compute the time constants and process dead times [67]. This renders the controller suitable for a wide range of operation conditions as typical for the solar fields. The computation of the parameters is throughly discussed in Section 4.2.3.

The controller output is bounded to $\pm 3.5\,\mathrm{bar}$ to avoid excessive off-design operation. An anti-reset windup loop is added to avoid accumulation of the integral part of the controller as the output reaches the operation limit. The input to the ARW is the maximum allowable positive and negative changes to pump differential pressure, $\Delta p_{\delta,\mathrm{lim}}$ and the PI-controller output is then bounded to these values.

4.1.3 Control concept

In this section, some results of applying the control concept described above are shown. The commercial power plant La Africana near Posadas in the province of Córdoba in Spain

(a) Satellite image of the power plant [Map data: Google, Inst. Geogr. Nacional].

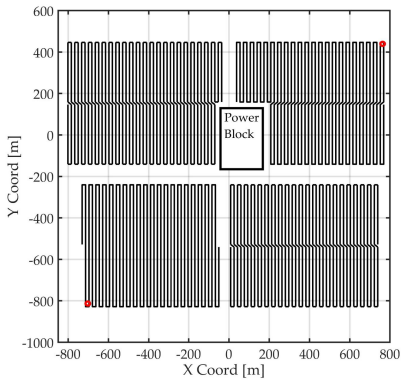

(b) Computational domain (header pipes not shown). Red circles indicate approximate locations of the weather stations.

Figure 4.6. La Africana power plant

Table 4.2. Simulation input parameters

Parameter	Value	Unit
T_{in}	290	°C
ΔT_{field}	103	°C
T_{SP}	393	°C
$\dot{m}_{min}$	84	$kg\,s^{-1}$
$p_{\delta,min}$	0.01	bar
$p_{\delta,max}$	15	bar

[63] is simulated and used as a test case. The plant geometry and layout are provided by the plant operators, africana energía, through a collaboration with industrial partners including TSK Flagsol Engineering GmbH. La Africana is designed to provide 50 MW of electric power. Its solar collector field has 4 subfields with a total of 168 loops and DOWTHERM®[21] thermal oil is the HTF. For all the simulations performed in this study, a constant solar field inlet temperature of 290 °C is used. The plant has two tanks filled with MS that are used for thermal energy storage; however, they, as well as the power block, are not simulated within this entire work. La Africana is equipped with 2 weather stations located in the NE and SW corners in the plant as indicated in Figure 4.6.

A fixed simulation time step of $\Delta t = 2\,s$ is used for the simulations. The Churchill method and the Dittus-Boelter equation are used to compute the friction coefficient and the convection heat transfer coefficient, respectively. The loops have lengths of 600 m and are discretized in 48 elements. Other header pipe sections are discretized in 2–5 elements depending on their lengths. The maximum allowable fluid temperature is set to 400 °C. Table 4.2 lists some more input parameters to VSF.

Spatially-invariant irradiance

Firstly, a spatially invariant DNI profile is applied to the solar field. This is to test the control concept at different DNI levels and with various temporal disturbances. Figure 4.7 shows the applied irradiation disturbance, where G_{eff} is the effective irradiance as described in Section 2.3.2. The simulated time is shown as the number of hours from the start. The profile represents long- and short-term disturbances at different DNI levels starting from 700 $W\,m^{-2}$, then 900 $W\,m^{-2}$ and dropping till 100 $W\,m^{-2}$. Also gradual step-up and down scenarios are shown at different rates, as well as a single jump.

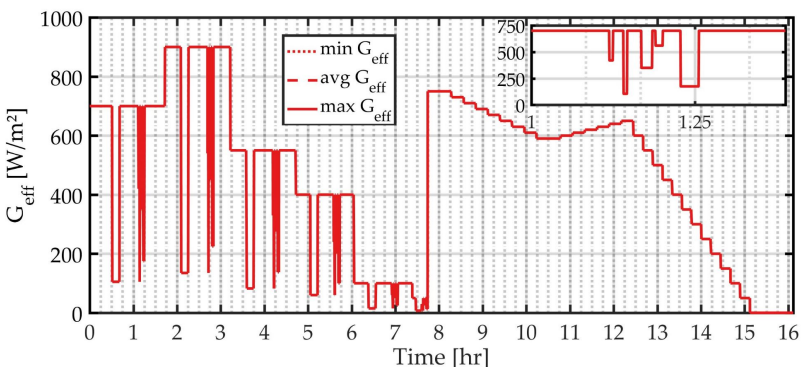

Figure 4.7. Spatially-invariant irradiance profile applied to the solar field with a zoom-in of the high frequency disturbances.

Figure 4.8 shows how the required mass flow rate, computed by the FF part, compares to the actual inlet mass flow rate as regulated by the controller. The FF controller provides good estimates of the required mass flow that result in stable field outlet temperatures till approximately 3.25 hrs. The FB loop was also able to regulate the mass flow when the temperature dropped slightly after strong fluctuations in the DNI.

From 3.25 hrs on, a significant difference between the required and actual mass flow rates can be observed and also linked with a drop in outlet temperature. Figure 4.9 shows the total percentage of the collector focus in the field. This provides some explanation to the reduced flow rate, such that after 3.25 hrs, approximately 10 % of the collectors are defocussed. By plotting the percentage focusing and temperatures of the 4 SCAs of an exemplary loop in the solar field, we observe partial defocusing mostly at the last SCA that keeps the collector temperatures below the temperature set-points as shown in Figure 4.10b. As the field outlet temperature did not recover from the slight decrease caused by the DNI fluctuations, the flow rate is slightly reduced to allow the temperature to rise. Since, in this case, the flow is lower than the required flow for the DNI level at that moment, overheating in the SCAs takes place causing them to remain defocused or even defocus more. The same behaviour is observed after the long period of very low DNI at 7.75 hrs. The defocusing is

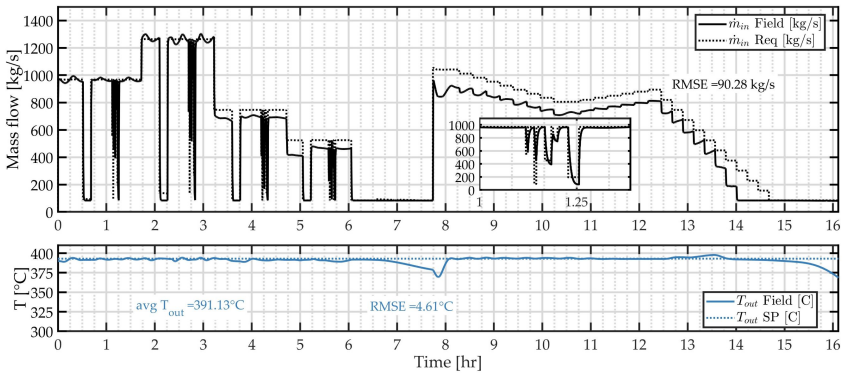

Figure 4.8. Mass flow rate and field outlet temperature for spatially invariant irradiance.

maintained at quasi-steady-state from 8 hrs till the next large disturbance at t = 13.5 hrs, where the temperature starts to drop resulting in excessive drop in mass flow, which causes some extra defocusing in the collectors.

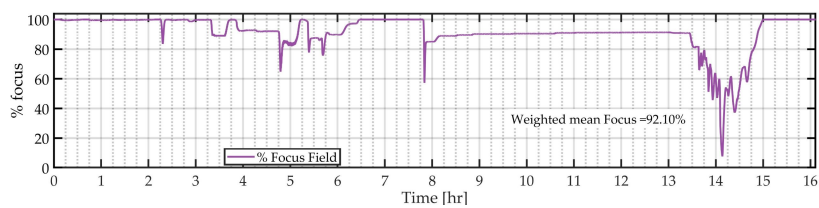

Figure 4.9. Total percentage focussing in the solar field.

Overall, the average outlet temperature is 391.13 °C with a root mean square error of 4.61 °C from the set-point. The mean focus of all the SCAs is weighted by the average effective irradiance at the corresponding time step and a weighted mean is computed. Through this method, higher weight is given to defocused collectors during clear skies than during cloud coverage. For this test case the weighted mean focus is 92.1 %. This means, that with the current controller, the solar field fails to collect approximately 8 % of the incident solar energy, even without spatial variation of the DNI.

Spatially varying irradiance

In this case, we consider spatial variation of irradiance by using DNI maps. The maps for this case are produced from shadow camera images installed at the Plataforma Solar d'Almería as described in Section 2.3.2. In Figure 4.11, the average effective irradiance falling on the field is plotted together with the minimum and maximum values observed

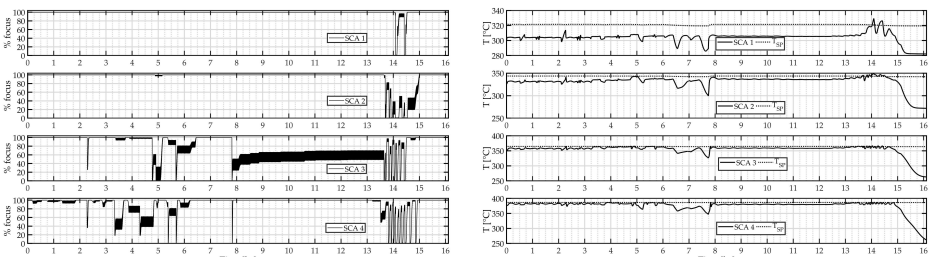

(a) Collector focus. **(b)** Collector middle temperatures.

Figure 4.10. Local SCA values in loop number 29 in subfield 1

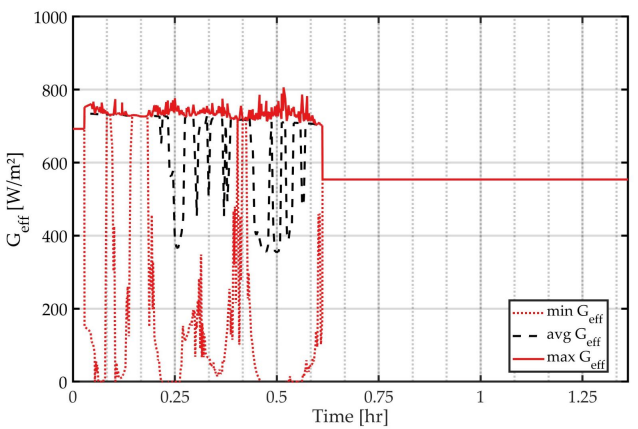

Figure 4.11. Solid and dotted lines show the maximum and minimum irradiance values in the field as measured by shadow cameras. Dashed line represents average irradiance from 2 weather stations. Values measured on 19.09.2015 at the PSA, Spain.

using the shadow cameras from [45] on the whole field as a function of time. The irradiation profile belongs to the category with thick small clouds, ThkS in Table 2.1. The duration belonging to the category is approximately 0.6 hrs, then the solar field is exposed to constant, spatially-invariant DNI in order to compute the steady-state response of the field after the disturbance. Some snapshots of the irradiance map are shown in Figure 4.12.

Figure 4.13 shows the inlet mass flow rate plotted with the required mass flow rate from the FF loop. Here again, a deviation of the actual flow rate from the required one is observed starting even earlier than the previous test case. Also a slight drop of the field outlet temperature is observed at the same time. The temperature drop results from partial shading of some loops. As shown in Figure 4.12a the clouds are not detected by the 2 weather stations and, thus, are not accounted for by the FF loop. The temperature drop causes the FB loop to reduce the flow slightly, which, in turn, later results in overheating in

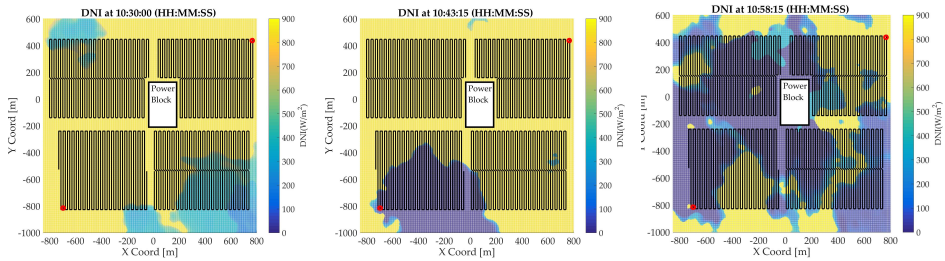

(a) t = 0.05 hrs **(b)** t = 0.25 hrs **(c)** t = 0.5 hrs

Figure 4.12. DNI maps at different times on 19.09.2015. The red circles indicate the approximate location of the weather stations.

the unshaded loops that get defocused. Some thick clouds can be observed starting from 0.25 hrs as the average irradiance value is nearly half of the maximum value.

Figure 4.14 shows the range of outlet temperatures of all the loops in the solar field. In the first diagram, the maximum, minimum and average loop outlet temperatures are plotted together with the solar field outlet temperature resulting from the mixing of all the loops. The operational temperature range between 375–398 °C is indicated by the dotted lines. The maximum temperature corresponds to the maximum allowable temperature of the fluid with a safety factor of 0.5 %, while the minimum temperature is chosen as a convenient value to avoid high thermal stresses in the components. The number of loops that exceed the maximum temperature or fall below the minimum temperatures are plotted in the second diagram as nTHigh and nTLow, respectively. The loop controller is successful to keep the HTF safe, with an average maximum temperature of 397.2 °C and maximum temperature overshoot of approximately 401.8 °C briefly reached in the loops. The minimum temperature in the loops is found to be 353.3 °C.

The lower diagram of Figure 4.14 shows the total focusing in the solar field. After approximately 0.2 hrs, some collectors start to defocus as the inlet mass flow rate is reduced as the field outlet temperature drops due to the passing clouds. However, as the sky gets clear and the field outlet temperature is still low, the controller does not push in enough flow which results in overheating and defocusing of the SCAs. This continues until a steady-state is reached with some defocusing maintained. This controller behaviour resulted in unnecessary defocusing and wasting of solar energy. The weighted mean focus is 88.7 %. It is also worth noting that at t=0.25hrs and t=0.5hrs, two contradicting effects take place; approximately 40 % of the collectors are defocused while, at the same time, 40 loops show a drop in the outlet temperature, representing approximately 23 % of the field. This is due to the absence of local flow control as the flow for al the loops is reduced, causing unshaded collectors to overheat, while completely shaded ones cool down.

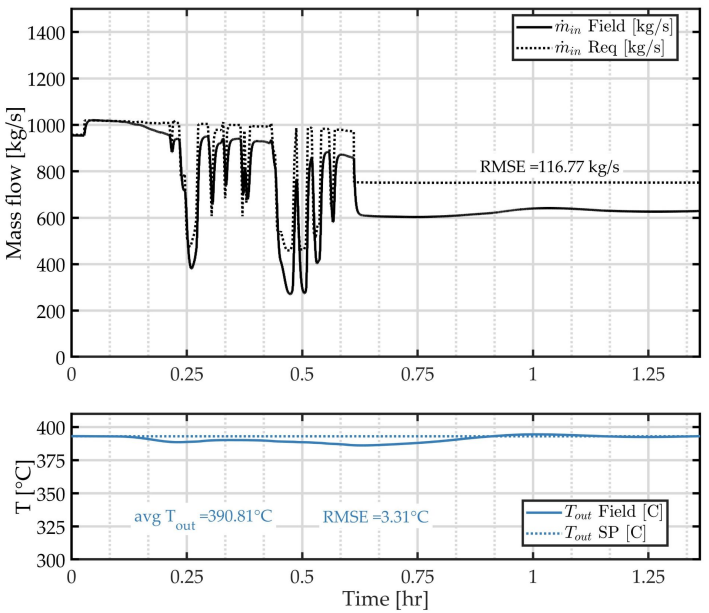

Figure 4.13. Solar field flow and outlet temperature for DNI data from 19.09.2015.

4.2 CHALLENGES

4.2.1 Manual operator intervention

The behaviour of the controller described above is practically unacceptable due to the large amount of wasted solar energy through defocusing. In operational power plants, manual operator intervention is needed in such situations. As observed in parabolic trough power plants in collaboration with this work, the operators switch off the solar field main flow controllers during strong transients and use their experience to control the flow to maximize energy yield and stabilize the field outlet temperature as much as possible. If they observe excessive defocusing in the collector field, they force in more flow to get the defocused collectors back to sun focus and then control the field outlet temperature accordingly. Alternatively, some operators prefer to reduce the flow to maintain the field outlet temperature while sacrificing some uncollected solar energy as shown previously. This depends on the plant operation strategy and the required energy yield on the specific day.

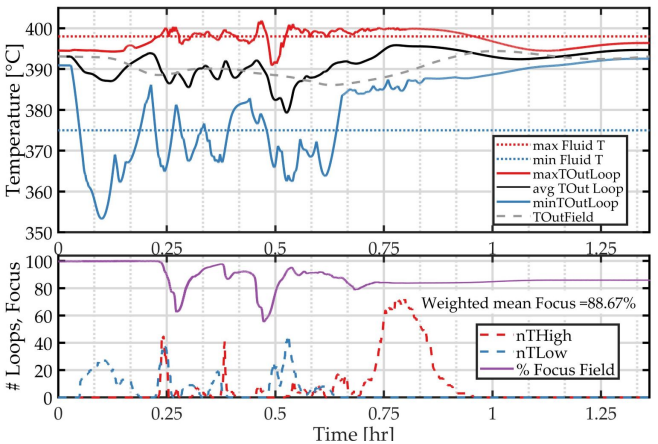

Figure 4.14. Range of loop outlet temperatures and field total focus for spatially-varying DNI.

4.2.2 Plant performance model

As described in Section 4.1.2, the mass flow FF loop relies on a simple static plant model to compute the required flow for the current irradiation condition. However, such model highly depends on the solar field condition such as the cleanliness of the mirrors and loop maintenance schedule. It also depends on the accuracy of the irradiation measurement devices and estimation of the thermal losses in the field [15, 17].

In the controller implementation presented in this work, the FB loop provides correction to the FF controller to compensate for the model errors listed above. The robustness of the control concept to systematic errors is discussed in the next chapter.

4.2.3 Wide range of operation

Solar fields have a wide range of operation in terms of the flow rate and temperatures, that has a notable effect on the system dynamics. Consequently, we used adaptive controller parameters that take the current state of the system into account so the controllers are properly tuned for the different behaviours. Figure 4.15 shows an example of the different system dynamics in response to a step down of the pump differential pressure from 8 to 7.5 bar. Two irradiance levels are studied, first with $600\,W\,m^{-2}$ and the other with $800\,W\,m^{-2}$, and the change in field outlet temperature is normalized and compared in the figure.

The controller tuning parameters depend on the process gain, K_p, time constant, T_p and dead-times, θ_p. The process gain is defined as the system response to a disturbance in the controlled parameter as stated in Equation (4.3). This is clearly different for the exemplary cases shown in Figure 4.15. As a result, the temperature FB controller parameters are computed adaptively depending on the system condition. A simple field model based on static

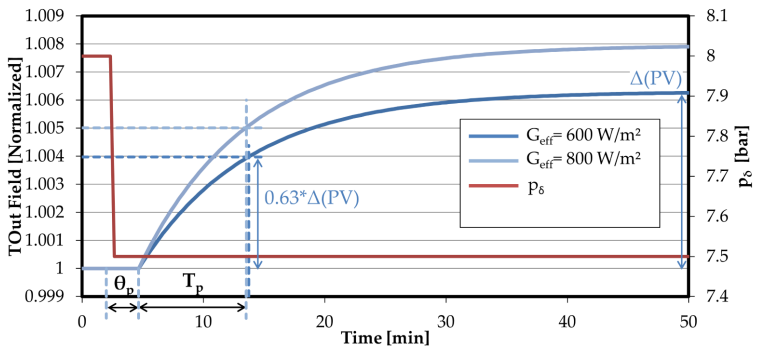

Figure 4.15. FOPDT different tuning values for different operation conditions in response to a step-down of the pump differential pressure, p_δ.

energy balance is set-up and a relation between the change in the field outlet temperature is response to a change in the pump pressure is derived as

$$K_p = -\frac{(\dot{Q}_{sol} - \dot{Q}_{loss})}{\bar{c}_p \cdot \dot{m}^2 (2c_2(\overline{T}_{Field})\dot{m} + c_1(\overline{T}_{Field}))} . \tag{4.7}$$

$c_1(\overline{T}_{Field})$ and $c_2(\overline{T}_{Field})$ are hydraulic system curve coefficients that depend on the mean temperature in the solar field as explained in Section 4.1.3. The values computed with this method show very good agreement with the simulated system response.

The time constant is defined as the time needed for the system to reach a change of 63.2 % of the steady state value for first-order systems. T_p depends mainly on the thermal inertia of the field and if there is a difference in the fluid through put time from the different subfields [43]. Quasi-dynamic models for the loop performance and residence time models for the travel time are described in [39], however, to save computation time, an approximation of T_p is computed as

$$T_p = \frac{\Delta H_{Field}}{\dot{Q}_{in,Field}} \times 0.6 , \tag{4.8}$$

where $\dot{Q}_{in,Field}$ is the net input thermal energy and ΔH_{Field} is the change of enthalpy in the field calculated as the sum of heat input to the HTF and to the pipe walls. This computation method does not consider the different fluid travel times from the subfields. This resulted in a systematic error from simulation data, which is fitted with the correction factor of 0.6

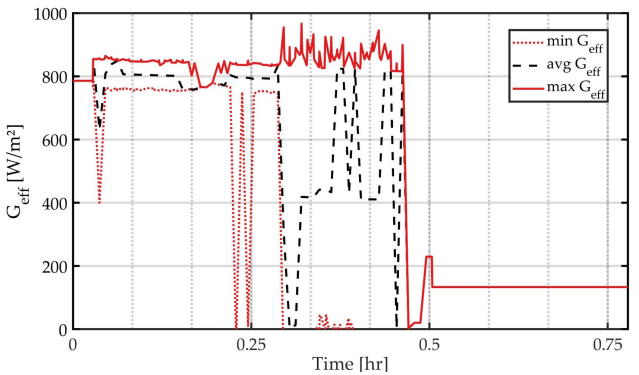

Figure 4.16. Solid and dotted lines show the maximum and minimum irradiance values in the DNI map. Dashed line represents average irradiance from 2 weather stations. Values measured on 16.06.2016 at the PSA, Spain.

for La Africana solar field. The process dead-time is computed from the shortest travel time from the subfields to the solar field outlet as

$$\theta_p = \min\left(\frac{l_{header}}{v_{header}}\right) + \Delta t_{sim}\,, \tag{4.9}$$

where l_{header} and v_{header} are the length and fluid velocity of the headers, respectively. The simulation time step, Δt_{sim}, is added, since the controller does not observe the response of the control action until, at least, 1 simulation time step.

4.2.4 Spatial variability of DNI

Parabolic trough power plants cover a very large surface area; however, they are usually equipped with only a handful of irradiation measurement points. For example, Andasol-III has 5 weather stations, while La Africana has only 2. The controllers use the measurement points to estimate the required flow for the FF loop. These are usually sufficient during clear-sky days or days with very little clouds. However, a lot of clouds pass undetected or cloud sizes are over- or underestimated when the spatial resolution is so low.

Figure 4.16 shows the minimum, maximum and average values of G_{eff} measured on 16.06.2016 as another example. Figure 4.17 shows a few snapshots of the irradiance maps, which are particularly interesting for a controller lacking information about the spatial distribution of clouds. The controlled flow and the resulting temperatures in the solar field are plotted in Figure 4.18.

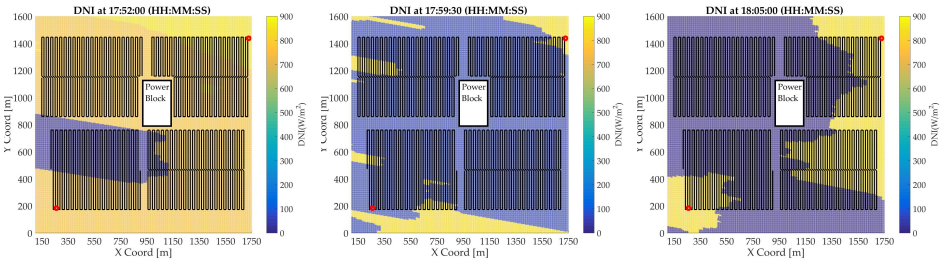

(a) t = 0.22 hrs **(b)** t = 0.33 hrs **(c)** t = 0.42 hrs

Figure 4.17. DNI maps at different times on 16.06.2016. The red circles indicate the approximate location of the weather stations.

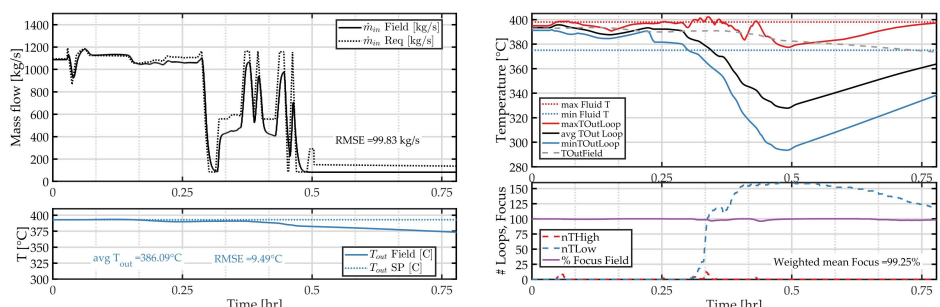

(a) Solar field flow and outlet temperature. **(b)** Loop outlet temperature ranges

Figure 4.18. Simulation results for DNI data from 16.06.2016.

In Figure 4.17a, a relatively large cloud covers a significant part of the solar field at t=0.22hrs without being registered by the weather stations and not affecting the FF controller. This results in temperature drop in the loops as shown in Figure 4.18b. At t=0.33hrs, large clouds cover nearly all of the field, however are only detectable by one of the weather stations. As a result, the average of both measurements indicates only partial shading and the flow is too high for the irradiation situation and the temperature drops noticeably. The third snapshot in Figure 4.17c shows large clouds that are not detected by any of the weather stations. The resulting increased flow causes further drop of the average loop and solar field temperatures.

4.2.5 Assessing controller performance

If the flow controller fails to provide the adequate flow rate in the solar field, the HTF will either overheat and cause defocusing of the SCA, or will be cooled down resulting in a lower solar field outlet temperature. Both result in a reduction in the field performance and energy yield, which is challenging to quantify. In order to evaluate the performance of the different controllers, energetic penalties for collector defocusing and reduced field

outlet temperatures have been developed. The penalties are calculated and summed up, such that the total penalty is

$$p_{tot} = p_{def} + p_{T,PB} + p_{TES}\,, \tag{4.10}$$

where p_{def}, $p_{T,PB}$ and p_{TES} are the penalties due to defocusing, reduced power block efficiency and diminished TES efficiency, respectively. The penalties are computed in monetary value to try to estimate the economic benefit or loss of using a specific control concept in specific situations. Then, we compute the pentalties as percentages of the calculated revenue for the investigated time interval.

To make the economic computations more realistic, we performed an annual yield simulation of the investigated power plant configuration using Greenius simulation tool developed at the DLR [20]. The simulation provides annual averages of the LCoE and power block conversion efficiency, $\eta_{PB,a}$, which is estimated as

$$\eta_{PB,a} = \frac{E_a}{Q_{PB,a}}\,, \tag{4.11}$$

where E_a and $Q_{PB,a}$ are the annual electric energy output of the power plant and thermal energy input to the power block, respectively. Each kW_{th} of energy not collected due to defocusing results in an economic penalty of

$$p_{def} = Q_{def} \cdot \eta_{PB,a} \cdot LCoE\,. \tag{4.12}$$

Q_{def} is the solar energy lost due to defocus in the respective time interval, which is equal to $\int \dot{Q}_{th,SF}(t + \Delta t_{tr}) \cdot \frac{1-f(t)}{f(t)}\,dt$. The value of $f(t)$ is the amount of focusing in the field as a function of time and $\dot{Q}_{th,SF}(t + \Delta t_{tr})$ is the thermal power output of the field which are calculated from the simulation results. The transient time delay Δt_{tr} is considered, because the current focusing state corresponds to the thermal energy output of a future time step. It is computed according to the average travel time in the field piping from the subfield outlet to the PB.

Another important factor that makes a good controller is the field outlet temperature. Off-design field outlet temperatures reduce the power block efficiency, as well as the efficiency of the thermal energy storage (TES). In order to penalize a reduced PB efficiency, the efficiency at the design temperature, η_{PB,T_o}, is estimated using a detailed heat flow diagram of the PB implemented in EBSILON® Professional . From this model, the PB efficiency, $\eta_{PB,T}$, is derived as a function of the HTF temperature as shown in Figure 4.19 for a 50 MW turbine. The reduction in HTF temperature is penalized as

$$p_{T,PB} = Q_{th,SF} \cdot \eta_{PB,a} \cdot \left(1 - \frac{\eta_{PB,T}}{\eta_{PB,T_o}}\right) \cdot LCoE\,. \tag{4.13}$$

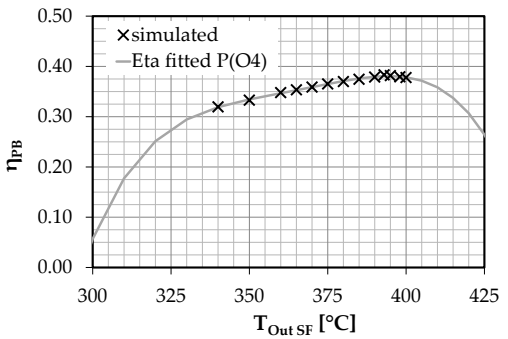

Figure 4.19. Simulation results and fitted interpolation of the PB efficiency as a function of temperature.

Finally, we add a penalty to account for the reduced stored energy due to low MS temperatures being pumped in the hot storage tank and the limited tank capacity. As the tank gets full, any thermal energy more than the PB capacity is an overload and will need to be dumped. The penalty value of such instances of dumping due to reduced storage efficiency is calculated as

$$p_{TES} = Q_{th,SF} \cdot \eta_{PB,a} \cdot \left(1 - \frac{T - T_{in}}{T_0 - T_{in}}\right) \cdot \frac{Q_{OL,a}}{Q_{TES,a}} \cdot LCoE\,. \tag{4.14}$$

T and T_{in} are the field outlet and inlet temperatures, respectively, T_0 is the design field outlet temperature, and the ratio $\frac{Q_{OL,a}}{Q_{TES,a}}$ represents the annually averaged ratio of TES overload resulting in solar energy dumping in the SF. Both annual averages are estimated from the Greenius simulations. The simulation results for the La Africana power plant set-up with yearly irradiance data are listed in Table 4.3.

Table 4.3. Greenius simulation results for La Africana power plant

	Value	Unit
LCoE	192.5	€/MWh
$\eta_{PB,a}$	0.25	-
$Q_{OL,a}/Q_{TES,a}$	0.33	-

The absolute penalty values have not been validated against real power plant data. However, they serve as excellent comparison values when comparing different control concepts as will be shown in Chapter 5 as more control concepts are developed and compared with the ones described in this chapter. To provide a reference value, the theoretical revenue is computed. This corresponds to the expected revenue from an ideal controller, which is

able to maintain the field outlet temperature at the set-point without any defocusing, and neglecting heat losses in the solar field. The theoretical revenue is computed as

$$R_{th} = \eta_{PB,a} \cdot LCoE \cdot \sum_{SCA} \int \left[G_{eff} \eta_{opt} w_{ap} l \right]_{SCA} dt \,. \tag{4.15}$$

On the other hand, the actual revenue results from transforming the thermal energy output of the field into electrical energy and is computed as

$$R_{SF} = \eta_{PB,a} \cdot LCoE \cdot \int \dot{Q}_{th,SF} dt - \left(p_{TES} + p_{T,PB} \right) \,. \tag{4.16}$$

The penalties due to defocusing are already included in R_{SF}, hence, only the additional penalties due to the reduced field outlet temperatures are subtracted. Other losses in the field correspond to the thermal losses and additional losses from the field transient behaviour that are not accurately considered within the computation of the penalties. These other losses are computed as

$$\text{oth.losses} = R_{th} - p_{def} - \eta_{PB,a} \cdot LCoE \cdot \int \dot{Q}_{th,SF} dt \,. \tag{4.17}$$

Thermal losses depend on the fluid temperature of the field, as well as the flow rate and are, hence, influenced by the field operation and control. The revenues, losses and penalties are, then, normalized by the theoretical revenue and used for the comparisons. The absolute values depend highly on the values of the PB efficiencies and LCoE computed from the annual simulation model in Table 4.3 and are only meant as to give an order of magnitude of the economics. In Chapter 5, the revenues and penalties for different control concepts in various DNI conditions are compared to provide a comprehensive and reliable measure of the plant and controller performance.

5 NOVEL CONTROL STRATEGIES

As more CSP projects are being built, continuous advancement and improvement to the field controllers is necessary. Moreover, new developments in related research and application fields, such as meteorology and control hardware, render it possible to incorporate more sophisticated control concepts and foster the energy yield of solar fields. For example, advancements in cloud detection and motion prediction can provide accurate irradiation maps and even short-term forecasts paving the way for optimized solar field control with model-predictive approaches. Moreover, the economic and technological feasibility of solenoid control valves and improvement in network communications offer the possibility to control the flow in each single loop to account for any local transients with very high resolution.

Nevertheless, the economic benefit of applying such advancements is yet to be proven. A simulation model with a high level of detail helps to estimate the benefits and feasibility before applying the control strategies to real solar fields. This reduces the commissioning time and risk, and avoids interrupting the operation of the power plant. In this chapter, the use of VSF to test and evaluate the benefit of some novel control concepts is discussed. Firstly, we take the first steps towards a fully automatic solar field flow controller under different weather conditions. Secondly, an initial study of the use of short-term DNI forecasts, known as nowcasts, is discussed. Finally, we investigate the potential of adding loop valves to improve the solar field performance. The main findings and result highlights are presented in this chapter; however, the reader is referred to Appendix F for the details of each simulated test case. Using the detailed simulation results, the scheme is able to quantify the economic benefit of one control strategy over the other.

5.1 AUTOMATIC FLOW CONTROLLER

As described in Chapter 4, the flow controller was found to be too slow for overcoming the effect of local transients. It also fails to recover the required flow to overcome the excessive defocusing in the collectors for some cases as shown in Figure 4.9 and 4.14. In some operational parabolic trough power plants, the operators switch off the automatic flow controller during thick cloud passages and manipulate the flow manually according to their experience and the field condition.

Numerous solar field control concepts are reported in literature, for example, main common flow controllers are described in [15, 95]. Moreover, a simple PID controller is modelled and described in [6]. More advanced control concepts which, to the knowledge of the

author, have not yet been implemented in large commercial projects, like model-predictive and fuzzy logic controllers are briefly outlined in [16]. However, a lot of challenges regarding automatic solar field control have been reported due to the local variations in irradiation on the large solar fields. An automatic solar field controller is interesting for us, so that the VSF can run independently and be used to test new control concepts. Thus, within the work for this thesis, an automatic solar field controller has been developed and implemented. The goal is to implement a controller that is more robust in various realistic irradiation conditions. In addition, a performance evaluation scheme is developed to compare it to other controllers as introduced in [60, 61]. In the following section, this scheme is discussed in more detail in the next section.

5.1.1 Field focus feedback

To emulate what a manual operator would normally do, an additional feedback (FB) loop observing the focusing condition of the solar field has been added to the flow controller. The control diagram is shown in Figure 5.1 where all 3 control components are shown, namely, the flow FF loop, the temperature FB controller and, finally, the focus FB (FFB) loop. This last FB loop forces the controller to push in more fluid to reduce the temperatures in the SCAs and, hence, getting them back to tracking. This controller does not directly control the pump; it, rather, alters the temperature error, $e_T(t)$, using a PI-controller. It indicates over heating when higher flow rate is needed and also signals field cooling to reduce the flow rate causing more defocusing in the case when solar energy dumping is needed. Using this method, we avoid having an over-determined system, where more than one controller manipulates the same parameter, in this case the change in pump pressure, Δp_δ.

The change in temperature error, Δe_T, is computed from the deviation, $e_f(t)$, of the current total focus in the plant, $f(t)$, from the focus set-point, f_{SP}. A set-point filter is added to increase the stability of the control scheme against abrupt set-point changes. It works by smoothing out sharp changes using a first order lag with a time constant equal to the integral time as shown in Figure 5.2. Also to foster the stability of the system, the controller output is bounded to $\pm 12\,^\circ C$ as a convenient value to avoid abrupt changes to the temperature error. The value of the bounds depends on the focus error from the set-point, such that a large absolute value for the bounds is used when the focus error is large, while smaller values are used for only small deviations from the focus set-point. The controller is manually tuned and satisfactory results for different scenarios have been obtained for process gain, $K_p = 3\%/^\circ C$, process time constant of $T_p = 160\,s$ and dead time $\theta_p = 4\Delta t_{sim}$. The performance of the controller is shown in the test cases described below.

Spatially-invariant irradiance

Firstly, the artificial spatially-invariant DNI disturbance shown in Figure 4.7 is tested in the same plant layout described in Chapter 4. Figure 5.3 shows the inlet mass flow rate

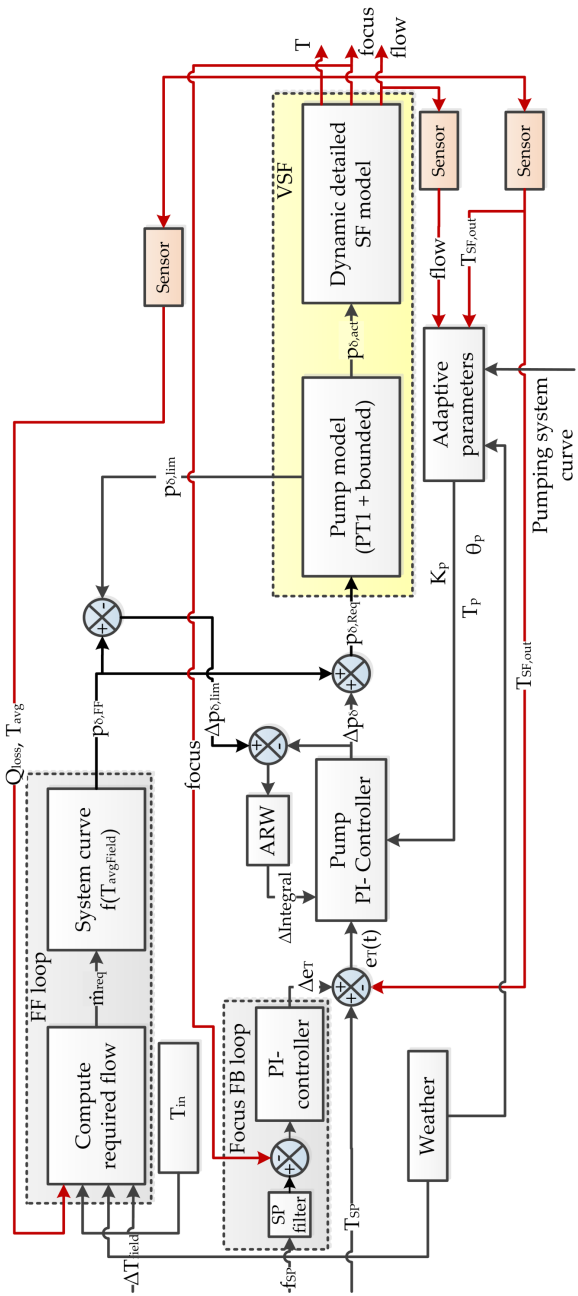

Figure 5.1. Automatic flow controller diagram.

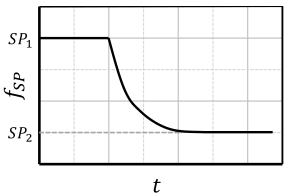

Figure 5.2. Schematic of the action of the set-point filter.

compared with the required mass flow rate from the FF controller, as well as the field outlet temperature. When the focus feedback loop is switched on, more flow is pumped to the solar field as soon as the field focus drops below the set value, here 100 %. As a result, the mass flow controller agrees better with the FF controller with a root mean square error (RMSE) of 55.78 kg s^{-1} as compared to 90.28 kg s^{-1} achieved by the basic controller in Figure 4.8. The automatic controller is also able to maintain the field outlet temperature close to the set-point, such that the mean outlet temperature is 390.22 °C with a RMSE of 4.91 °C from the SP. The mean field outlet temperature is, however, slightly lower than the 391.13 °C achieved by the basic controller. This is due to the prioritization of the controller to avoid defocussing over maintaining the exact temperature set-point.

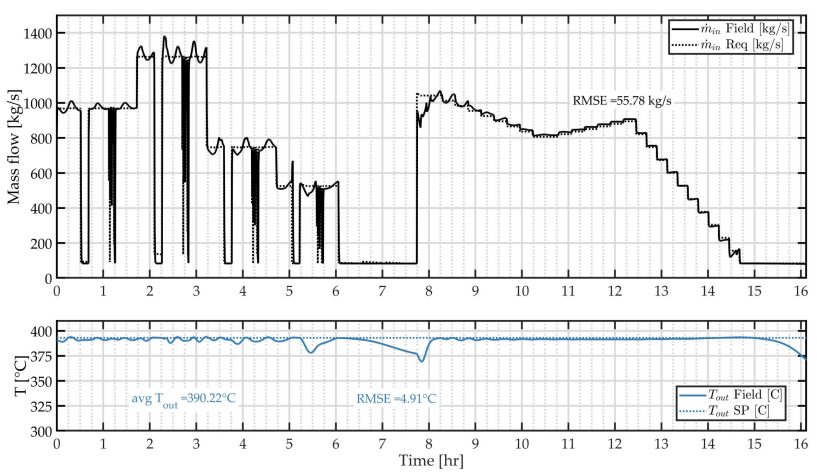

Figure 5.3. Mass flow rate and field outlet temperature for spatially-invariant DNI with the automatic flow controller.

Figure 5.4 shows the total field focus during the simulation time. The automatic controller demonstrates significantly improved solar energy harvesting with a weighted mean

focus of 99.35 % as compared to only 92.1 % in Figure 4.9. Also appreciably lower disturbance in the collector focus and temperatures in shown in Figure 5.5 as compared to Figure 4.10.

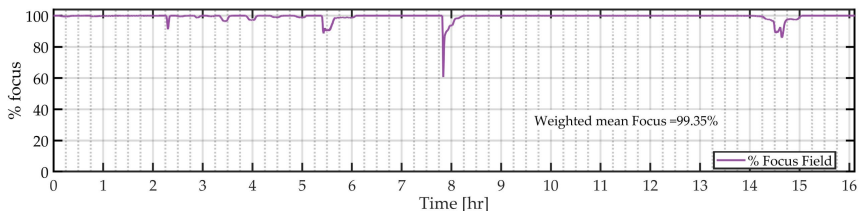

Figure 5.4. Total percentage focussing in the solar field for spatially-invariant DNI with the automatic flow controller.

As described in Section 4.2.5, the penalties method provides a comprehensive comparison between the different control concepts. The total penalties as percentage of the plant theoretical revenue for the basic and the automatic controllers are shown in Figure 5.6a and 5.6b, respectively. The break-down of the 3 different penalties and other losses is also shown. The total of the revenue, penalties and losses represents the theoretical revenue if all the incident solar irradiance were to be perfectly captured without any thermal or defocus losses. This is equal for both the basic and automatic cases. The basic controller resulted in revenue of 83.54 %, where the penalty resulting from defocusing represent the clear majority of the penalties at 7.02 %. Thermal losses in the field account for approximately 9.1 %. On the other hand, the automatic controller yields 90.43 % of the theoretical revenue and is able to significantly reduce the defocusing penalty to only 0.59 %. However, the PB and TES efficiencies are slightly reduced resulting in an increase of the corresponding penalties as compared to the basic controller. This is due to the slightly reduced field outlet temperature as shown in Figure 5.3. The thermal losses are also slightly lower due to the reduced field operation temperature.

Spatially varying irradiance

The controller shows also better performance with irradiance data from the DNI map on 19.09.2015 shown in Figure 4.11. Figure 5.7 shows the mass flow rate and field outlet temperature. As with the spatially-invariant test case, the average field outlet temperature is 388.15 °C, which is lower than that of the basic controller, 390.73 °C, as shown in Figure 4.13. However, the difference in average field outlet temperature between both controllers is noticeably higher for the spatially varying case at 0.68 % in contrast to only 0.23 % for the spatially invariant case. This is due to the absence of spatially distributed flow control as the overall flow is increased in response to overheating and defocusing of unshaded

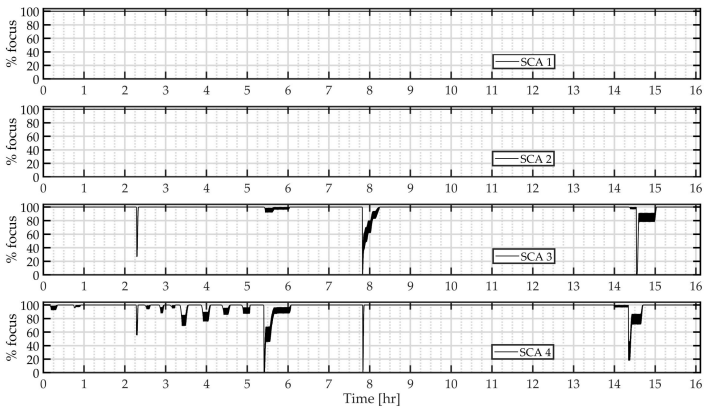

(a) Collector focus.

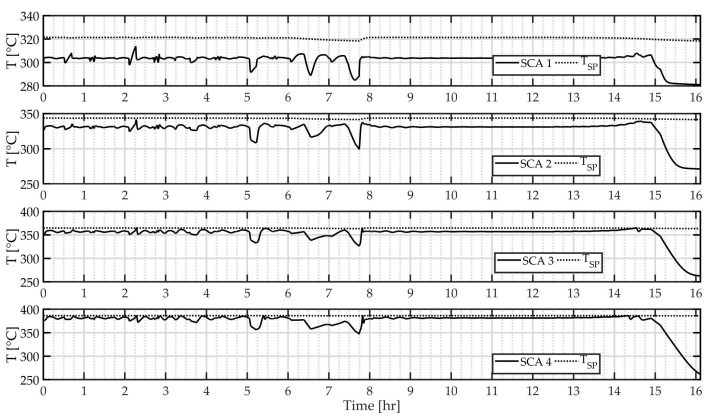

(b) Collector middle temperatures.

Figure 5.5. Focus and temperatures of 4 SCAs in loop number 29 in subfield 1 for spatially-invariant DNI with the automatic flow controller.

loops as some thick clouds partially shade the field. This is specifically prominent at approximately t = 0.5 hrs as shown in Figure 5.8, where more than 130 loops cool down in comparison to only 40 loops in the previous case. This is the expected behaviour as the advanced controller forces in more flow to reduce the over-all defocusing and achieves a weighted average focus of 96.42 % against only 88.67 %.

Consequently, the automatic controller is able to increase the economic benefit by 7.1 % of the theoretical revenue using the same irradiance data from weather stations as the basic controller as shown by the penalties in Figure 5.9. The additional penalties due to the lower field outlet temperature are also shown in the figure as the PB and TES penalties are nearly tripled.

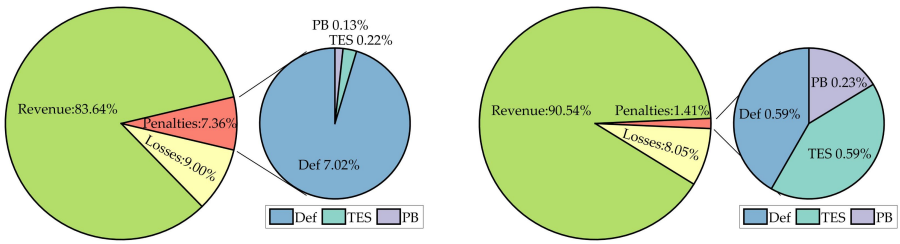

(a) Basic controller without FFB. **(b)** Automatic controller with FFB.

Figure 5.6. Penalties break-down for spatially-invariant DNI.

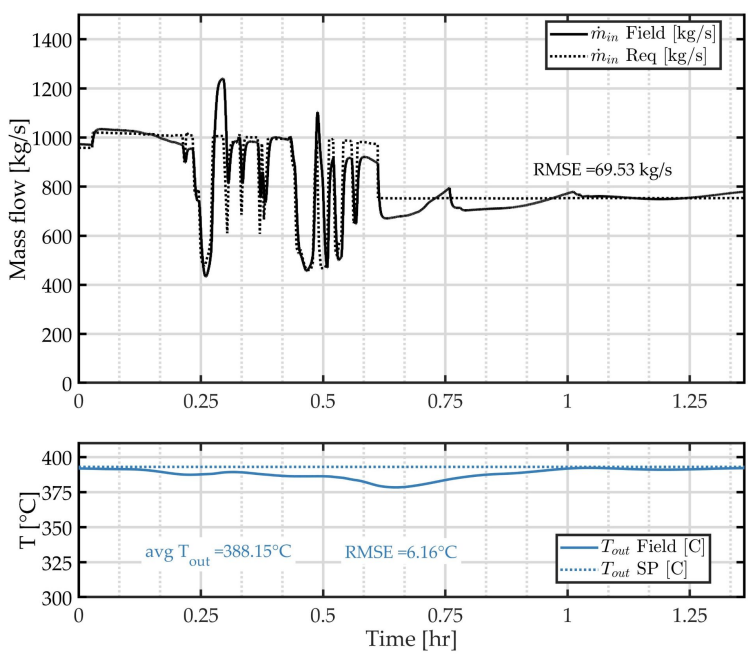

Figure 5.7. Solar field flow and outlet temperature for spatially varying irradiance (ThkS1).

In Section 4.2.4, the challenges associated with spatially varying DNI have been discussed. Figures 5.10a and 5.10b show the penalties break-down for the test case on 16.06.2016 with the basic and automatic flow controllers, respectively. Despite the reduction of the defocusing penalties and thermal losses, the automatic controller slightly underperforms the basic controller in this test case due to the significant drop in outlet temperature resulting in reduced PB and TES storage efficiencies. The plots given in Figure F.19 depict the flow rate and temperatures in the field. The mean field outlet temperature of

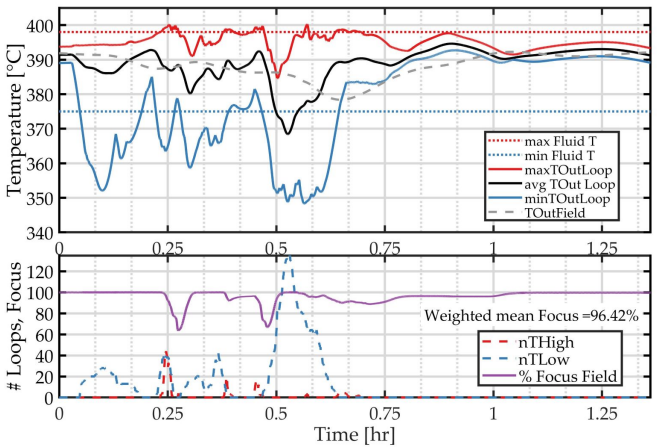

Figure 5.8. Range of loop outlet temperatures and field total focus for spatially varying irradiance (ThkS1).

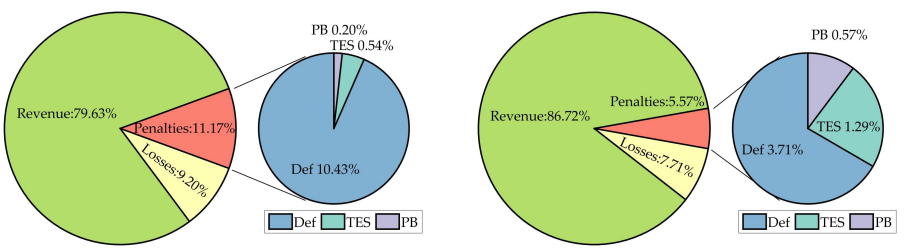

(a) Basic controller without FFB. **(b)** Automatic controller with FFB.

Figure 5.9. Penalties break-down for spatially varying irradiance (ThkS1).

384.51 °C is approximately 0.41 % lower than that resulting from the basic controller in Figure 4.18a.

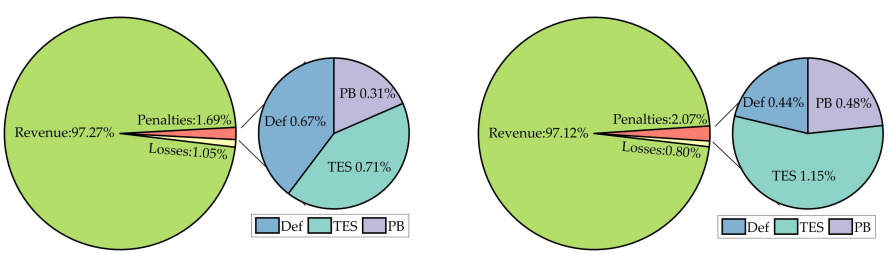

(a) Basic controller without FFB. **(b)** Automatic controller with FFB.

Figure 5.10. Penalties break-down for test case on 16.06.2016 (ThkH4).

Both controllers are compared for numerous test cases. Table 5.1 shows a list of the different test cases classified according to the DNI category as presented in Section 2.3.2. The number of test cases in each category correspond to the number of representative incidents found within the data processed from DNI maps from cloud and shadow cameras. The detailed simulation results are presented in Appendix F. Figure 5.11a shows a radar map of the percentage revenue from the theoretical revenue averaged for each of the DNI categories. The automatic controller harvests an average of 90 % of the incident irradiance in the CS and RQ categories. The collected energy slightly drops to approximately 85 % for days with small and large thick clouds, ThkS and ThkL, respectively. This is typically due to the increased defocusing in the field as the loops are exposed to spatially varying DNI conditions whilst the flow is not adjusted for each loop accordingly. On the other hand, the expected revenue significantly drops to round 67 % for days with thick clouds with little gaps belonging to the ThkH category. Generally, the flow is very low for such DNI conditions, as shown in Appendix F.5, which results in high thermal losses and significant over-heating of any loops that get exposed to solar irradiance through the gaps in the clouds.

The performance of the automatic controller surpasses the basic controller for all categories except RQ, where the revenue for both controllers is nearly the same. Figure 5.11b shows the normalized percentage revenue of the basic and automatic controllers for all the weather categories. For CS and RQ, the differences between both controllers is minor showing that the basic controllers could effectively operate the solar field for most cases. The highest performance boost is with the ThkS and the ThkL categories, where the cloud disturbance traverses the whole field and the automatic controller improves the revenue by 10 % and 13 %, respectively. However, the improvement is only 2.5 % when the DNI belongs to the category of thick clouds with gaps, ThkH. This is because there are only very few unshaded loops and the flow corresponding to the mean DNI is generally too high for most of the loops. Hence, the field outlet temperature drops significantly. This causes the temperature FB PI-controller to reach its output limits and not to be able to modify the prescribed flow from the FF loop adequately. Also a further reduction in the flow would cause an increase in the defocusing of the unshaded loops. In addition, the output of the FFB loop is also limited to $-3.5\,^{\circ}\mathrm{C}$ resulting in it not being able to correct the temperature drops that exceed $20\,^{\circ}\mathrm{C}$ from the SP according to Figures F.16 and F.19, for example.

5.1.2 Challenges

In this section, some common challenges for the automatic controller are described. Furthermore, the performance and robustness of the controller during those challenges is tested for the different DNI conditions and the limitations are discussed.

Table 5.1. Test cases dates and times for each DNI category. The time interval does not include the clear sky part added to achieve steady-state.

	Day	from	to	Duration [min]	Day	from	to	Duration [min]
	CS				RQ			
1	18.09.2015	10:10:15	10:53:00	42.75	18.09.2015	09:45:15	10:10:00	24.75
2	18.09.2015	11:16:45	14:41:15	204.50	19.09.2015	08:31:45	08:39:45	8.00
3	18.09.2015	15:06:15	16:03:15	57.00				
4	24.11.2015	11:31:00	16:07:30	276.50				
5	27.11.2015	09:50:30	13:53:30	243.00				
	ThkS				ThkL			
1	19.09.2015	10:30:00	11:05:00	35.00	08.09.2015	14:14:00	15:42:00	88.00
2	19.09.2015	11:46:30	12:34:45	48.25	16.06.2016	14:17:00	14:46:00	29.00
3	19.09.2015	12:54:15	13:12:15	18.00	16.06.2016	15:04:30	15:28:00	23.50
4	19.09.2015	14:53:45	15:11:30	17.75	27.09.2016	14:31:00	15:11:00	40.00
5	19.09.2015	16:50:00	17:11:45	21.75				
	ThkH							
1	18.09.2015	16:20:30	18:08:15	107.75				
2	18.09.2015	18:21:00	18:39:45	18.75				
3	19.09.2015	18:19:00	18:41	22.50				
4	16.06.2016	17:40:00	18:08:30	28.50				

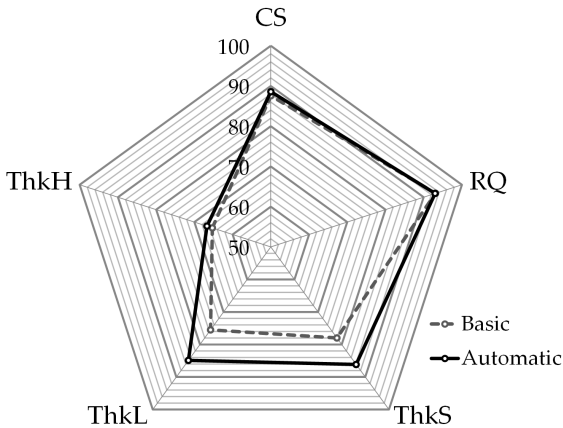

(a) Revenue percentage.

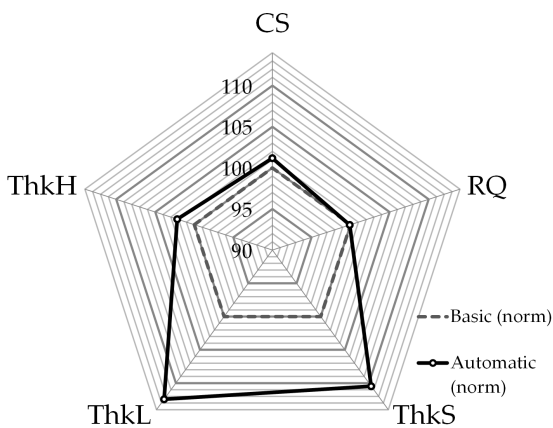

(b) Normalized revenue.

Figure 5.11. Comparision between the basic and automatic flow controllers for different DNI categories.

Thermal performance model

In real power plants it is considered impossible to predict the thermal performance of the solar field accurately. The thermal performance highly depends on a few factors, some examples are listed below:

- Mirror cleanliness, which is very difficult to determine accurately given the large stretch of the solar fields and dependence on the dust and sand conditions in the air.
- Irradiance condition, which is impossible to accurately predict in the case with passing clouds, as power plants are usually equipped with only a few weather stations measuring the irradiance at specific locations. Even though cloud cameras provide

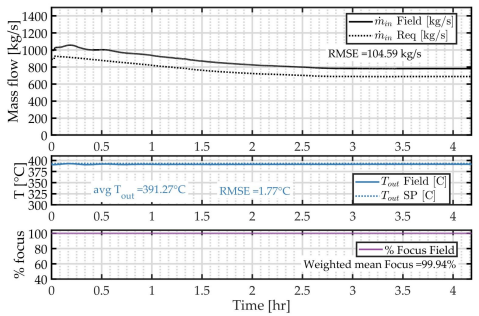

(a) Flow, outlet temperature and field focus.

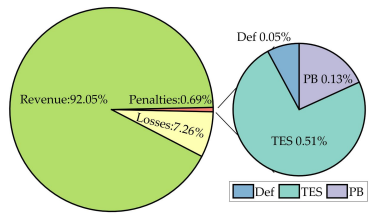

(b) Penalties and losses.

Figure 5.12. Case CS2 with −10 % error in FF controller.

detailed irradiance maps on the field depending on the cloud conditions, they come with some uncertainties estimated to be in the range of 8–10 % according to [47].

- Field maintenance, such that one or more loops could be shut down for maintenance.
- Defective components such as mirror facades or absorber tube glass, which affects the thermal insulation of the tube [65].
- Measurement uncertainties of all DNI, flow, temperature and pressure sensors.

If the above information is not accurately provided to the flow FF controller, the resulting required flow or pressure, $p_{\delta,req}$, will be erroneous. For clear-sky conditions, controllers predict a correction factor for the FF controller, which depends on the actual plant performance. However, during short term transients, like passing clouds, this correction factor fails to adjust the required flow accordingly as the cloud situation changes quickly.

In the test cases described above, we considered that the mass flow FF controller provides ideally accurate estimates of the required mass flow for the current average irradiance condition in the field. As most of the above-mentioned sources of error occur over long periods of time, for example a few hours to few days, they impose systematic errors in the system. Therefore, we impose systematic error on the mass flow rate provided by the FF loop of ±5 % to 25 % to test the robustness of the controller to more realistic cases. Figure 5.12 shows the simulation results for test case number CS2 in Table 5.1 as an example. The FB controllers in this case are able to adjust the flow, such that the process variables are kept at the set-points despite the erroneous prescribed mass flow. The robustness of the controller is proven by comparing the revenue from idealistic mass flow FF and the one with the imposed error. In this test case, the revenue is 92.04 % of the theoretical revenue, which is nearly equal to the revenue without any errors in the FF controller at 92.09 % as shown in Figure F.2. Accordingly, the control concept is considered robust for such disturbances.

With regard to transient conditions, Figure 5.13 shows the results of another test case with passage of some thick small clouds and considering positive and negative errors in

the FF controller. The case with the ideal mass flow controller is shown in Figure 5.7 and correspond to the DNI category ThkS1. Again, the two FB components of the control system are able to correct the flow accordingly and provide stable operation with small effects of less than 1 °C on the average field outlet temperature and field focus. These small differences are mainly due to slower response to the temperature drops resulting from the accumulated integral part of the FB components that correct the inaccurate estimate of the FF loop. This is especially prominent in the case with the negative error. The distribution of revenues and penalties plotted in Figures 5.13c and 5.13d show a difference of less than 0.5 % in revenue from the ideal case in Figure 5.9b. Overall, for cases with negative error in the FF part, the FB PI-controllers have a high positive integral part causing them to tend to force in slightly more flow than needed. This, in turn, results in some minor drop in temperature, which increases the penalties due to losses in PB and TES efficiencies. Moreover, this results in an increase in plant focus as the collectors have lower tendency to overheat. In contrast, having a positive error in the FF part results in high tendency of the FB controllers to reduce the flow a bit too much, which, consequently, causes some defocusing in the field and an increase in the corresponding penalties. In general, the defocusing losses are considerably higher than the losses due to the lower outlet temperature, which results in higher revenues for the case with negative error often surpassing the performance of the ideal FF controller.

This investigation is performed for all the test cases and categories listed in Table 5.1 for errors in the mass flow FF of ± 5 % to 25 %. The revenues are normalized by the revenue in the case with ideal mass flow FF controller for each category. In Figure 5.14, a summary of all the results is compiled. For the most part, the control concept is very robust to systematic errors of up to ± 10 % losing no more than 0.5 % for CS, RQ and ThkS cases. The controller is even still very robust for ± 25 % in the ThkS cases. However, the performance drops slightly for the ThkL category and more significantly for the ThkH category as the controllers are operating at their boundary output values while keeping the field operation stable. As for the ThkL case, the controller with negative error outperforms the one with positive error as discussed previously. Nevertheless, behaviour is inversed with the ThkH category as the average DNI level is generally very low for this category as are the temperatures of the shaded loops. As a result, the unshaded loops are overheated and only minor benefit on the defocusing can be achieved with slight increase in flow for the negative error cases as compared to the positive error ones. Under these circumstances, the penalties resulting from even lower temperatures are higher than the small benefit of the reduced defocusing resulting in lower overall revenues.

In conclusion, the described control concept is robust to errors in the thermal performance model in the FF controller. The two FB components of the controller are able to correct the errors and yield performance similar to the ideal case for errors up to ± 10 % for the CS, RQ, ThkS and ThkL cases. The performance drop is, however, more prominent for the ThkH category as the it drops by up to 2 % from the controller with ideal overall mass

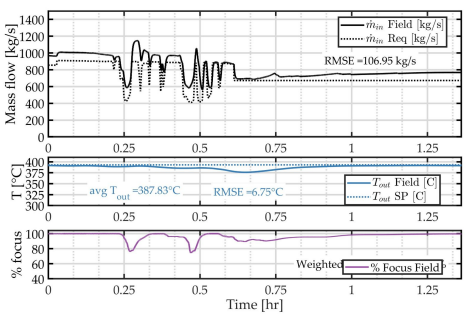

(a) Error of -10%.

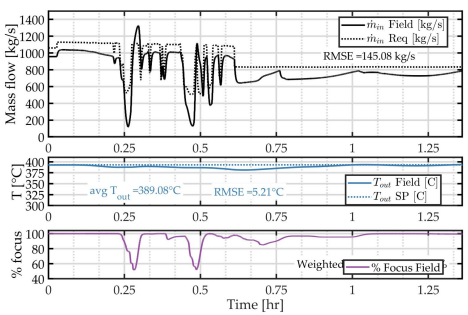

(b) Error of +10%.

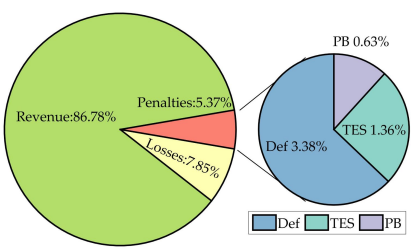

(c) Penalties for -10% error.

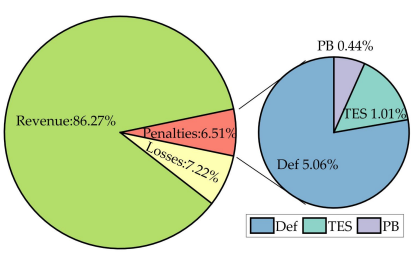

(d) Penalties for +10% error.

Figure 5.13. Case ThkS1 with ± 10 % error in FF controller.

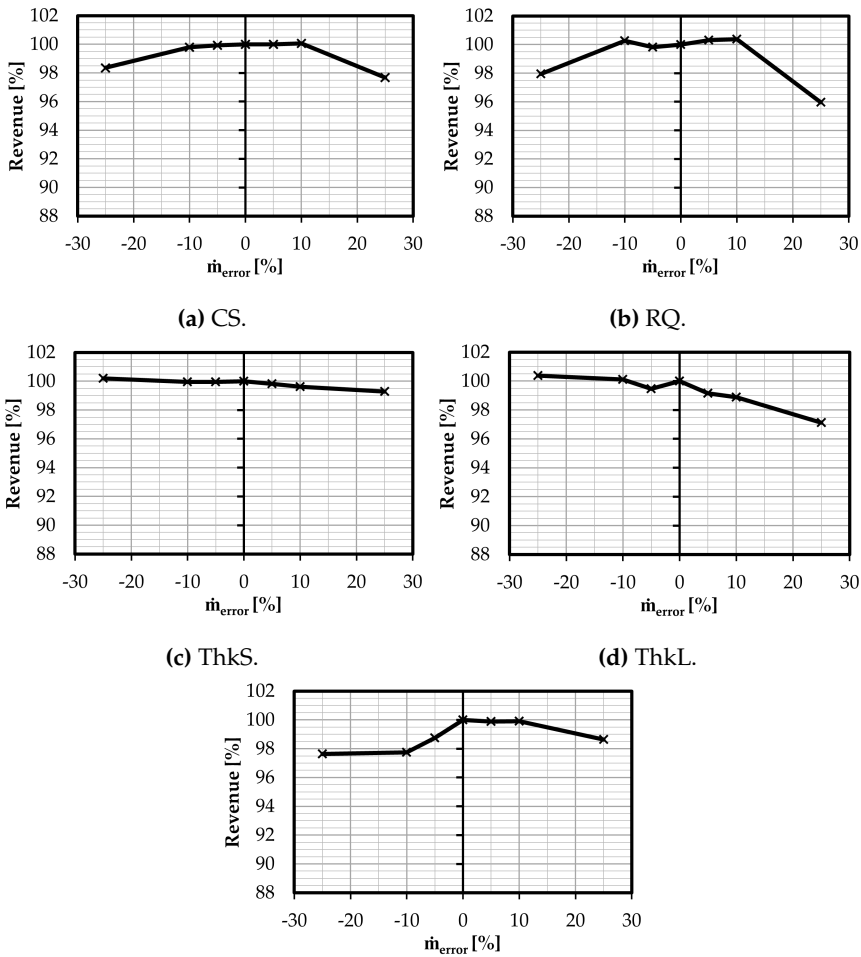

(a) CS.

(b) RQ.

(c) ThkS.

(d) ThkL.

(e) ThkH.

Figure 5.14. Normalized average revenues of the test cases of the 5 categories at different errors in the mass flow FF controller.

flow FF estimation. This is not expected to have a significant effect on the plant daily or annual yield, as the revenue during such weather conditions is anyhow very low. As for the errors as high as 25 %, the performance drops by up to 4 %. As a result, the plant performance models should be accurate enough to avoid such considerable decline in revenues.

System dead-time

Up to this point, the controllers have been reacting in real-time and operating every simulation time step, which is typically 2 s for all the simulations included in this thesis. The controllers have instantaneous access to all needed FB quantities and current process variables to produce their adjusted output accordingly. This, however, is challenging to realize within real systems and is associated with a few system delays that could be due to

- signal processing,
- actuator response and dead times,
- operator input, and
- mass or thermal inertia of the controller actuators or sensors that is not considered in the controller tuning.

The above listing have been obtained from power plant designers and operators experiences, and also observed from field visits to commercial solar fields. Exact information about the durations of such delays are not investigated within this work. The study is intended to show the controller reaction if such delays are present in the system and how they affect the plant performance and energy yield in different DNI situations.

Therefore, artificial system delays of 10, 15, 30, 45, 60, 90 and 120 s are added to the system, such that the controllers in VSF are only invoked at those time intervals. Within the time intervals, the flow controllers do not receive any information about the system and, hence, do not change their output. The local SCA controllers, however, are always online. Figure 5.15 shows the changes in revenue with the added system delays for the same simulation set-up described before with the 5 DNI categories. As can be expected, system delays have negligible effects on clear-sky situations, because of the imperceptible changes in irradiance within the scope of 2 min delay. Nearly similar is the behaviour with random-quick clouds (RQ); however, the performance drops by nearly 1 % with system delays of 120 s as the little disturbance in irradiance already affect the yield.

In contrast, for transient cases, the revenues increase considerably for short system delays, where they peak at approximately 15 s delay and then tend to decline for longer delay times. The performance boost is approximately 3 % for ThkS and ThkL clouds and is a whole 6 % for the ThkH category. To explain this, the results of a time delay of 30 s in case ThkL3 is presented in Figure 5.16 and compared to the no delay case in Figure F.15 as an example. Firstly, it is observed from the flow in Figure 5.16a that the controller is more conservative and the overshoots in the flow are hindered. As a result, excessive temperature drops are avoided as the average field outlet temperature is approximately 2 °C more

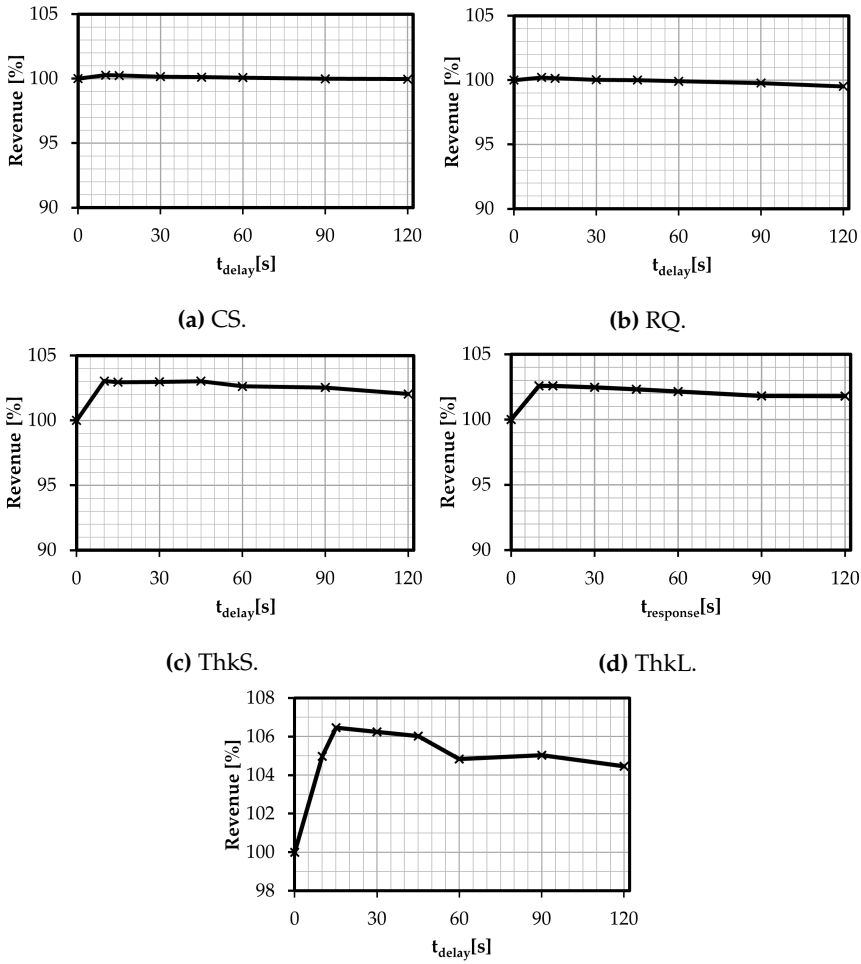

(a) CS.

(b) RQ.

(c) ThkS.

(d) ThkL.

(e) ThkH.

Figure 5.15. Normalized average revenues of the test cases of the 5 categories with different system time delays.

in this case. This serves for the reduction of the PB and TES penalties as shown in Figure 5.16b. Secondly, due to the reaction delay the flow does not follow the high frequency DNI disturbances like the ones shortly before $t = 0.5hrs$. This causes the unshaded collectors to remain in focus and does not significantly affect the temperatures, as the disturbances are local and take only a very short period of time. This can be shown as the average focus of the SCAs is increased from 97.6 % to approximately 99 %.

As expected, the performance drops for longer delay times as the flow does not correspond to the actual irradiation condition. This is especially prominent for the ThkH case,

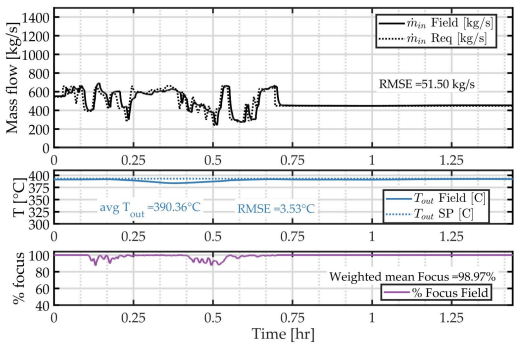

(a) Flow, outlet temperature and field focus.

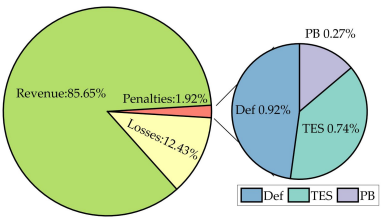

(b) Penalties and losses.

Figure 5.16. Case ThkL4 with time delay of 30 s.

as the total flow is typically very low and the time constant and dead times for the temperature FB controller are too long, which limits its ability to correct the effect of the delayed controller response.

5.1.3 Solar energy dumping

During the operation of the power plant on high irradiation days, the solar field thermal energy output might exceed the capacity of both the PB and TES, or the TES could get full. The excess irradiance needs to be dumped through defocusing some collectors. This is traditionally achieved by manually reducing the inlet fluid flow in the solar field which results in overheating of the collectors, thus causing defocusing. In this section, the implementation of the dumping feature in the automatic flow controller is explained and the plant performance for some test cases with energy dumping is illustrated.

The portion of solar energy that needs to be dumped, D, is input to the mass flow FF block and the required mass flow is weighted by $(1 - D)$. Also the set-point for the field focus FB loop is computed, such that the allowed defocusing in the solar field is given by:

$$f_{dump} = D \cdot \left(1 - \frac{\dot{Q}_{loss}}{\dot{Q}_{sol}}\right), \tag{5.1}$$

where $\dot{Q}_{loss}$ and $\dot{Q}_{sol}$ are the total thermal energy loss and collected solar energy in the field, respectively. This takes into account the amount of thermal energy lost and sets the set-point to achieve the needed energy dumping level. $\dot{Q}_{loss}$ is computed as the sum of the thermal energy dissipated from all loops and absorber pipes.

The dumping controller is applied for the test cases CS2 and ThkS1 and demonstrated below. The dumping set-point is set to 10 % and 30 % and the results are shown in Figures 5.17, 5.18 and 5.19. For the clear-sky case with 10 % energy dumping, the resulting revenue is exactly 90 % of the revenue without dumping as shown in Figure F.2. The field

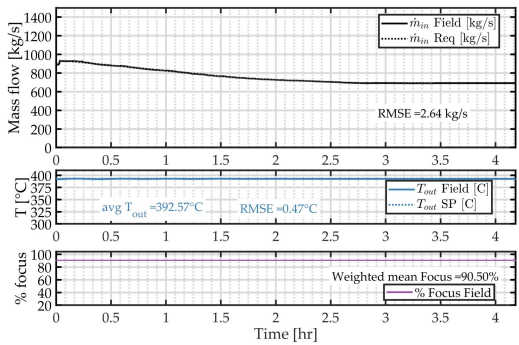

(a) Flow, outlet temperature and field focus.

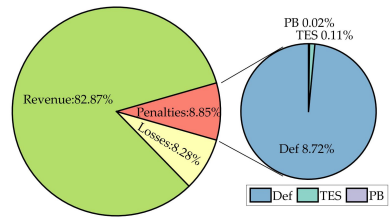

(b) Penalties and losses.

Figure 5.17. Case CS2 results with 10 % solar energy dumping.

outlet temperatures are kept within the set-point and the mean focus value is very close to the required portion of the solar energy to be collected. As for the 30 % case, the revenue represents approximately 72 % of the case without dumping while the mean field outlet temperature is 395.8 °C, which is already more than the temperature set-point of 393 °C. The controller is not able to further reduce the focusing by lowering the flow, as the temperature error correction exceeds the controller bounds, making the temperature FB controller take-over the mass flow control. Thus, a steady-state error in the defocusing is maintained as the FB PI-controllers output is bounded. The loop temperatures in Figure 5.18b show that the emergency controllers in the SCAs are able to maintain the loop temperatures below the maximum allowed temperature of 398 °C, and the emergency controller in the loop outlet ensures safe operation below 400 °C.

More transient behaviour is shown in case ThkS1 in Figure 5.19. The dumping signal is given at t $\approx$ 0.02hrs, where the required mass flow drops accordingly as shown in Figures 5.19a and 5.19c. For both cases, the mean field focus approximately reflects the required dumping and both controllers maintain stable field outlet temperatures despite the strong transients. The penalties represent 10.7 % and 25.2 % of the theoretical revenues for the 10 % and 30 % dumping cases, respectively as shown in Figures 5.19b and 5.19d. For the 30 % dumping case, the losses are also increased by approximately 3.5 % due to the excessive heat losses in the defocussed collectors and reduced flow rate. This is already taken into account when setting the focus set-point as shown in Equation (5.1). Table 5.2 summarizes the percentage revenues for the test case without any dumping and with 10 % and 30 % dumping. The relative revenues with respect to the non-dumping case. It is shown that the dumping controller achieves the desired reduction in collected energy.

To conclude, with the help of the focus FB loop, the automatic controller is able to operate the solar field during overload operations when less energy is needed from the field. The controllers exhibit very stable operation and are able to maintain the field outlet temperatures within the set-point even during transient conditions. Nevertheless, more

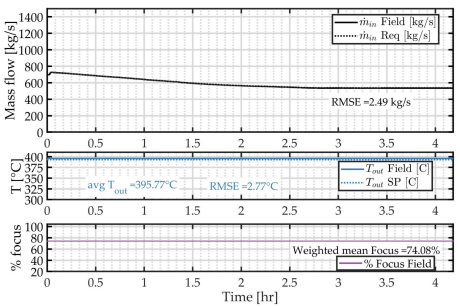

(a) Flow, outlet temperature and field focus.

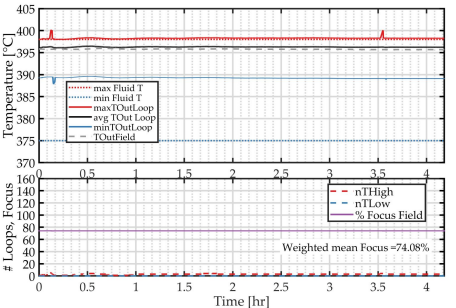

(b) Range of loop temperatures.

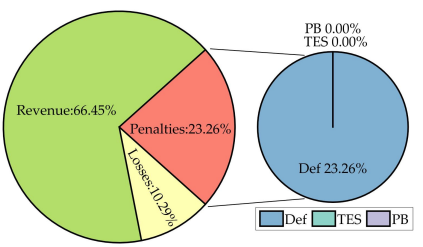

(c) Penalties and losses.

Figure 5.18. Case CS2 with 30 % solar energy dumping.

Table 5.2. Revenues with the dumping controller in case ThkS1.

D [%]	Rev. [%]	Rel.rev. [%]
0	86.8	100
10	80.2	92.4
30	63.64	73.3

tuning of the controller bounds and temperature set-points is needed to effectively achieve higher values of solar energy dumping.

5.2 CONTROL USING NOWCASTING DATA

As described in Section 2.3.2, technologies using cloud and shadow cameras are able to provide highly spatially-resolved DNI maps with short-term forecasts. These maps not only serve as accurate input of the weather situation to the VSF, they can also be used by the controller to improve the field operation and increase its energy yield. To demonstrate this, improvements to the control concept described in this chapter are implemented and the results are presented in this section.

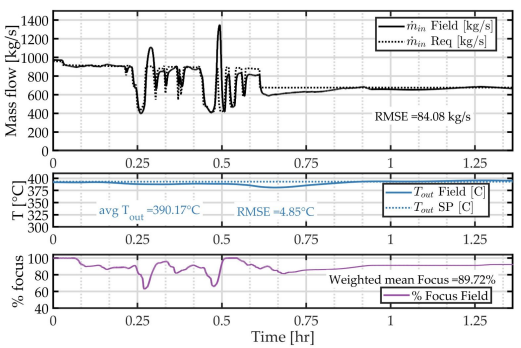

(a) Dumping 10 %.

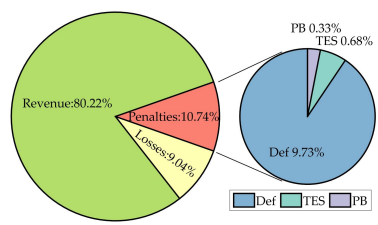

(b) Penalties for 10% dumping.

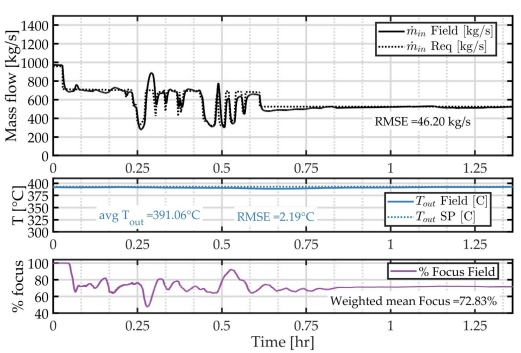

(c) Dumping 30 %.

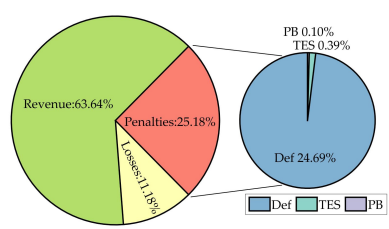

(d) Penalties for 30% dumping.

Figure 5.19. Case ThkS1 with 10 % and 30 % dumping.

5.2.1 Using current DNI

As described in Equation (4.4), the mass flow FF controller uses the available DNI measurement points to estimate the required mass flow in the field according to the available solar resource. The controller in all test cases shown previously use DNI measurements from 2 weather stations illustrated in Figure 4.6b. It has also been discussed that only 2 measurement points are not sufficient to provide information about the current irradiance situation. We have seen cases where the irradiance is over-estimated, like in Figure 4.17, or underestimated, as in Figure 4.12b. The FB controllers do a good job to correct the effect of false input to the FF controller; however, their response is always delayed by the system deadtime and process time constants. This results in sub-optimal performance during transient conditions when the spatial variability of irradiance is high. Now with the availability of irradiance maps, the spatial variability is available to the controllers and the response delays could be significantly reduced.

The FF controller is slightly modified to act upon the average of the whole DNI map instead of only the average of the measurements from weather stations. The VSF makes it possible to quantify the benefit of the DNI nowcasting system on the field control in different situations. This contributes to investigating the feasibility of adding such systems, like cloud cameras, to a solar field and, by computing the expected revenues, it gives a good estimate of the return on investment.

To study this we used DNI maps to compute the revenue increase for each of the test cases listed in Table 5.1 in comparison to data from weather stations. Here it is important to note that we considered that DNI maps provide exact prediction of the irradiance falling on the collectors. The results are compiled and the average of the percentage revenue for each DNI category is normalized by the revenues from using data from weather stations only. Figure 5.20 shows the percentage increase in revenue for each category.

Obviously, the change in revenue for the CS and RQ is negligible as the weather stations already provide accurate estimates due to the absence of any noticeable spatial variation. The performance during random-quick cloud passages is minutely reduced by 0.03 % as some collectors defocus if the flow is reduced as the thin clouds pass. In this case, the improvement due to the slight increase in outlet temperature does not compensate the defocusing losses. The revenues increase by 1.84 % and 1.44 % for the ThkS and ThkL categories, respectively. The biggest performance boost is seen for ThkH category as the revenues are increased by approximately 4 %. From the plot, it can be inferred that the improvement in controller performance is highly dependent on the spatial variability of the DNI situation.

To gain more insight on how the system performs along a whole day, some exemplary days, listed in Table 5.3, are simulated with the controller using the actual DNI maps from the nowcasting system. The controller performance is then compared with the cases where measurements from 2 weather stations are used. The average, maximum and minimum effective irradiance for the 5 days are plotted in Figures 5.21 to 5.25. Solar field start-up is not considered in any of the 5 cases.

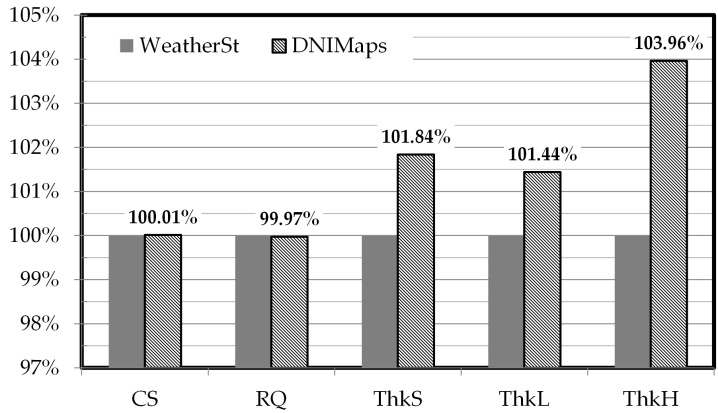

Figure 5.20. Comparison of normalized revenues for cases with using DNI data from 2 weather stations and from DNI maps for the 5 DNI categories.

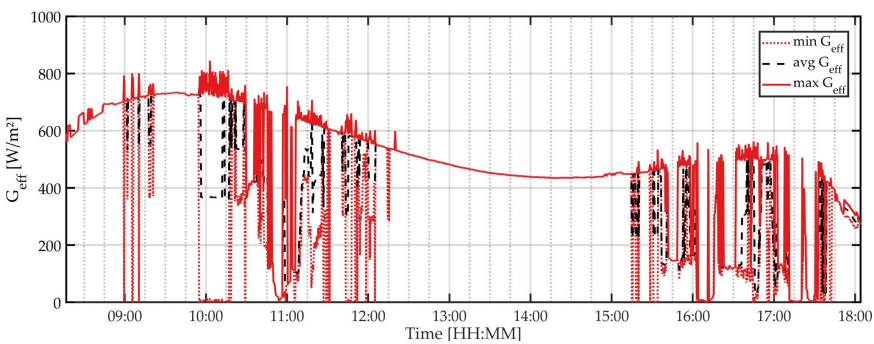

Figure 5.21. G_{eff} on 10.10.15 (WD1).

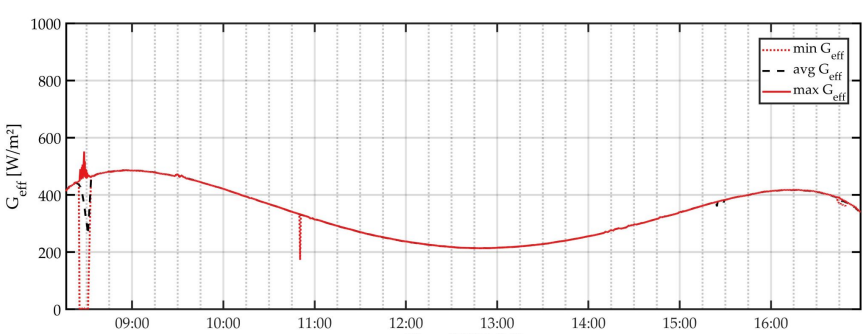

Figure 5.22. G_{eff} on 24.11.15 (WD2).

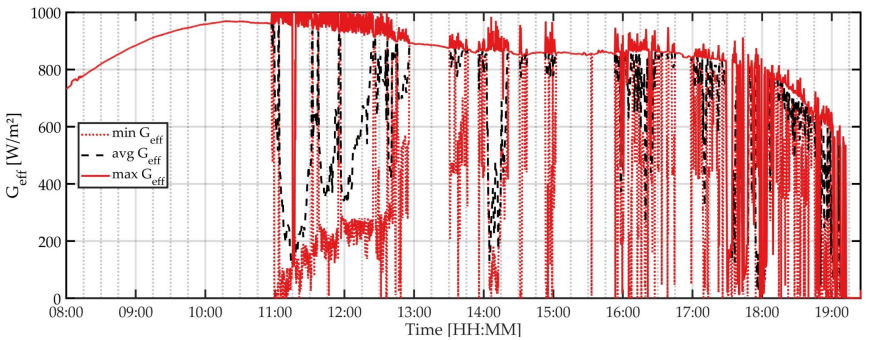

Figure 5.23. G_{eff} on 14.05.16 (WD3).

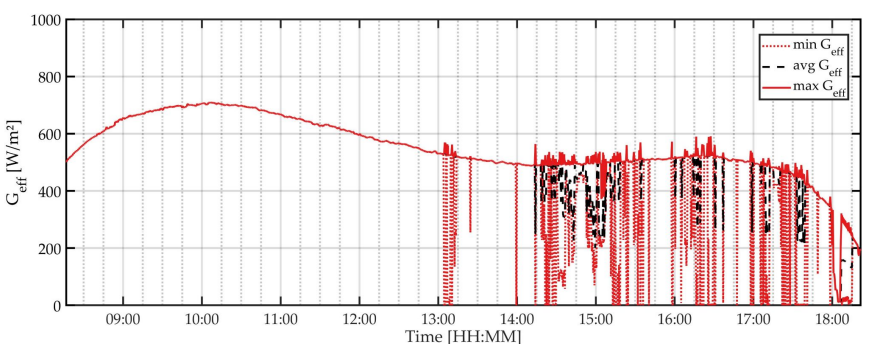

Figure 5.24. G_{eff} on 27.09.16 (WD4).

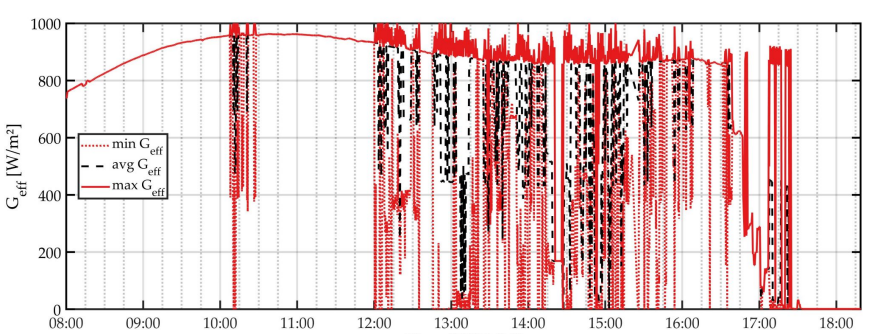

Figure 5.25. G_{eff} on 11.05.16 (WD5).

Table 5.3. Whole day simulations using the nowcasting system.

Case	Day	Main irradiance characteristics
WD1	10.10.2015	Mostly CS with thick clouds in the morning and evening
WD2	24.11.2015	CS at low DNI levels
WD3	14.05.2016	CS morning at high DNI level with thick cloud passage from the afternoon
WD4	27.09.2016	CS morning and noon with cloud passage late afternoon
WD5	11.05.2016	CS morning till noon strong transients in the afternoon and complete blockage in the evening

The simulation results and penalties are plotted in Appendix F.6, while the expected revenue for each day is compared in Figure 5.26 for the cases using weather stations and DNI maps. The RMSE between the average G_{eff} computed from the two weather stations and that from the maps for each test case is computed. It is then normalized by the average irradiance of the maps to provide comparable values for the various cases and plotted on the figure. The normalized RMSE (nRMSE) indicates how inaccurate the average of the measurement of the weather stations is as compared to the actual average DNI on the field. The nowcasting system improves the yield for all the 5 investigated days with highest gains during days with high DNI variability and nRMSE. For example, the highest gains are 2.24 % and 2.22 %, which correspond to approximately €1400 and €2500 more revenue per day, for cases WD1 and WD5, respectively. The nRMSE is approximately 14 % for both cases. The improvement is a little less for case WD3 making only 1.71 %, due to the increased thermal losses as average field outlet temperature is higher than cases WD1 and WD5. For cases with low nRMSE, the gain in revenue is less significant as shown in case WD4. However, there are merely any significant gain for CS cases as shown previously in Figure 5.20 and confirmed in case WD2, where the revenue gain is a mere 0.03 %.

Although absolute revenue strongly depends on the accuracy of the annual yield simulation results listed in Table 4.3, the comparison between the revenues in both cases indicates the expected order of magnitude for the benefit of using the nowcasting systems.

5.2.2 Using forecasted DNI

Nowcasting systems also provide short-term forecasts of 15 min for the DNI maps [62]. A weighted average of the forecasts is used to estimate the required mass flow in the FF controller, such that the effective irradiance fed to the FF controller is computed as

$$G_{eff,FF} = \sum_{n=0}^{15} w_n G_{eff,n} \,, \tag{5.2}$$

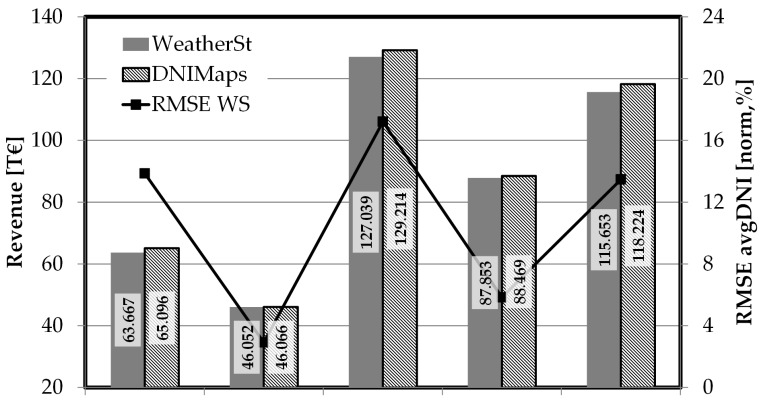

Figure 5.26. Comparison of revenues for cases with using DNI from 2 weather stations and DNI maps for whole days in Table 5.3. The black line represents the nRMSE of the average DNI of weather stations measurements.

where n is the forecast number. The current irradiance is given for $n = 0$ and the 15 min lead time forecast is for $n = 15$. Different averaging weights, w_n, have been tested and the weighting sets are depicted in Figure 5.27. Both shown weighting sets lay significantly higher weights on the current and near-future irradiance with weight set ws9 considering forecasts with lead times up to just 5 min.

Figure 5.28 shows the revenues of the same 5 whole days in Table 5.3 including using forecasts with weighting set ws9. When compared to using DNI maps of the actual observed value, the inclusion of additional forecast values with different weights does not show significant benefit in the current control concept. For cases that consider higher weights on future forecasts, for example ws3, the performance even drops in comparison to using the maps only. This is due to the lack of explicit use of any optimization procedures based on information of the futuristic state of the solar field. In addition, the forecast maps include some prediction errors of 20 % up to 30 % for spatial resolutions of approximately 50 m, where the magnitude of the error depends on the lead time of the forecast [46, 47]. This is already taken into account in the simulation since the forecast DNI maps are not the one that will finally hit the field. Here real nowcasts from the cloud camera system with all forecasting inaccuracies are used instead of just using the DNI values from the time series of the current DNI map which is used as the solar energy input to the system.

On the other hand, however, in case of system delays and the controller cannot be operated in real-time frequency, the knowledge of short term DNI forecasts will get more important. This is because the calculated control action will then consider the effects of

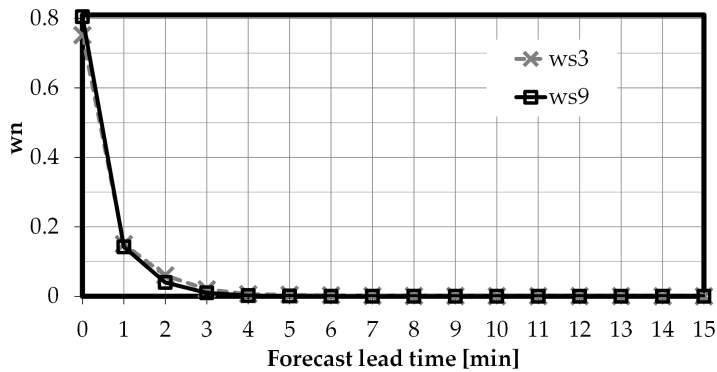

ws3	0.752	0.1501	0.06	0.02	0.006	0.0045	0.0027	0.0013	$8x10^{-4}$	$7x10^{-4}$	$6x10^{-4}$	$4x10^{-4}$	$3x10^{-4}$	$3x10^{-4}$	$2x10^{-4}$	$1x10^{-4}$
ws9	0.805	0.142	0.04	0.01	0.002	0.001	0	0	0	0	0	0	0	0	0	0

Figure 5.27. Nowcasting averaging weights sets.

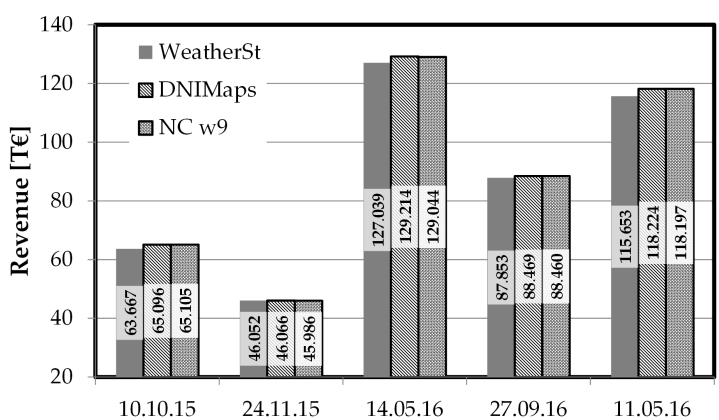

Figure 5.28. Comparison of revenues with using nowcasting data for the whole days in Table 5.3.

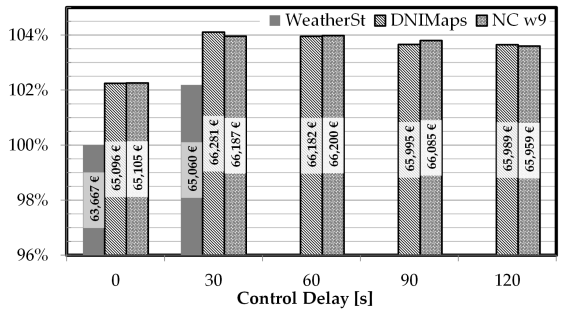

(a) Case WD1 (10.10.15).

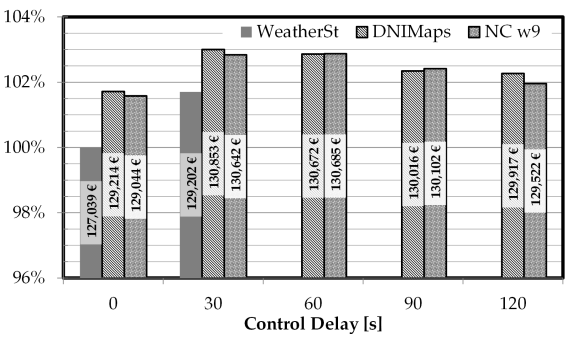

(b) Case WD3 (14.05.16).

Figure 5.29. Comparison of revenues with using nowcasting data with system time delay.

a longer time period in the future, for example the next 90 s instead of only the current DNI. Possible sources of controller and system delays are listed in Section 5.1.2. Hence, we investigated using the forecast nowcasting maps for system delays of up to 120 s and the revenue for cases WD1 and WD3 are plotted in Figure 5.29. For both cases, the addition of forecasts improved the revenue for system delays of 90 s. Nevertheless, the change is very minor yielding only 0.1-0.2 % more revenue. Accordingly, Figure 5.30 shows the normalized revenue for all 5 days using a weighted average of the nowcasting forecasts with ws3 and ws9 and a system delay of 90 s.

As it is expected, the performance with using ws3 is lower than ws9 for all investigated days, since it puts higher weight for future forecasts than in ws9 and the current control concept does not utilize such information effectively. Again, the best performance is achieved for WD1, WD3 and WD5, which are the days with the most transient conditions.

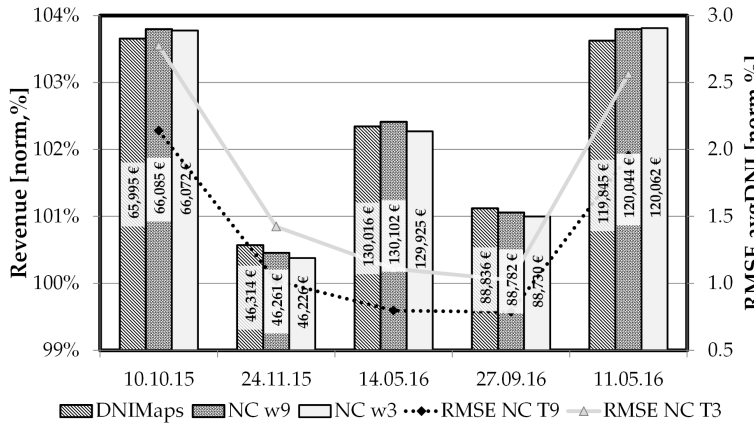

Figure 5.30. Comparison of revenues with using nowcasting data with 90 s system delay. The grey and dotted lines represent the nRMSE of the average irradiance based on ws3 and ws9, respectively.

5.3 LOOP VALVE CONTROLLER

There is growing interest in using controllable loop valves to manipulate the flow in the individual loops to react to local transients [1, 59]. For example, the flow could be reduced in a few loops if smaller clouds shade only a small portion of a subfield. This will result in smaller temperature drop in the loops and maintain more stable field outlet temperature. Similarly, defocusing of unshaded loops could be avoided through locally increasing the flow in the loops in cases when the total solar field flow is reduced. This usually occurs due to larger clouds that cover most of the power plant as has been shown in the previous section. Such cloud shading scenarios could only be captured through spatially-resolved DNI data provided by the cloud camera systems.

For this test case, a simple controller has been implemented to open or close the valves in response to loop outlet temperature variations. The main principle of the controller is that it is a single control element that controls all the SCAs in a loop, as well as the valve at the loop inlet. This is achieved by slightly opening the valve aperture when the loop outlet temperature exceeds a prescribed upper set point, T_{max}. Also slight defocusing of the SCAs to ensure safe operation takes place. If the loop valve could not be opened further, more defocusing in the SCAs will take place. Valve openings as well as the collector focus are given by percentages. As the temperature excessively drops below the minimum, `TMin`, the collectors get quickly back to focus and the valves are slightly closed. In the safe operation temperature range, the controller ensures that all the collectors are focused and slightly closes the valves to increase the temperature as close as possible to the maximum. The goal of the controller is to stabilize the loop and solar field outlet temperatures while ensuring

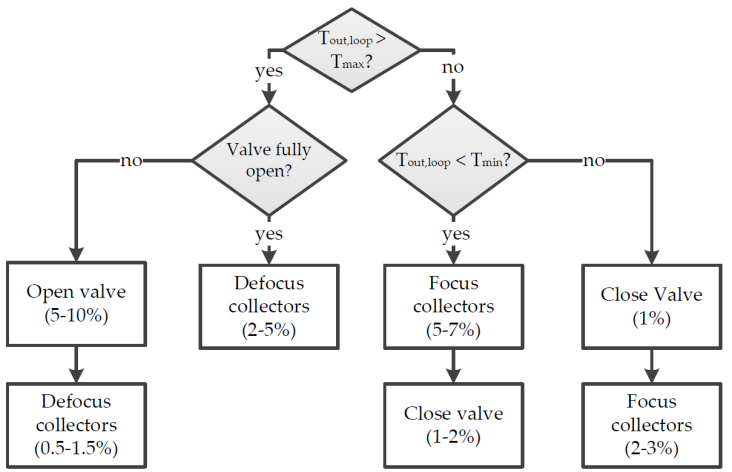

Figure 5.31. Valve and focus algorithm for local loop controllers.

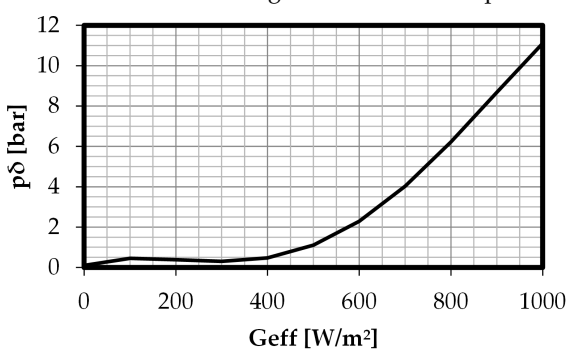

Figure 5.32. Pump differential pressure as a function of the average irradiance on Andasol-II power plant.

that the maximum temperature limit for the oil (400°C) is not exceeded. A pseudocode of the control algorithm for the collectors and loop valves is shown in Figure 5.31 below.

For the investigation of the benefit of loop valves control, simulations of Andasol-III power plant are performed and the thermal power output of the power plant is studied. To avoid interactions with the main flow controller, all three parts of the automatic flow controller are disabled and the flow is rather controlled as a function of the average effective irradiance, G_{eff}, on the field. The relation is determined from a polynomial fit of the differential pump pressure, p_δ, during plant operation as shown in Figure 5.32.

Figure 5.33 shows a comparison of the subfield and solar field outlet temperatures using the same control strategy as in Figure 5.31, once without manipulating the valves and the other including valve control. The dashed lines correspond to the temperatures for the case of collector focus control without loop valve manipulations, while the solid lines show the results of using controlled loop valves. The dotted lines show the mean DNI values

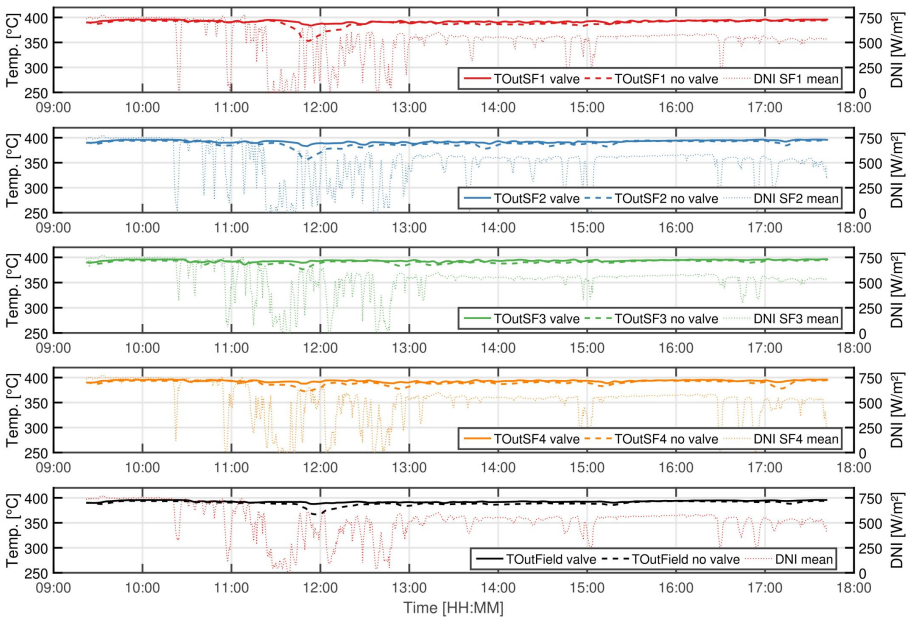

Figure 5.33. Subfields 1–4 and solar field outlet temperatures for control scenarios with (solid) and without (dashed) loop valve control in Andasol-III. The dotted lines show the mean DNI values of the DNI maps in each subfield and the mean over the whole solar field.

from the DNI maps in each subfield and the whole solar field. Both control scenarios have the same lower and upper temperature set-points of 394°C and 400°C, respectively. Stable outlet temperature during field operation is maintained when controlling the loop valves. This is specifically significant at strong cloud passages from 10:30 till 13:00 o'clock, such that strong temperature fluctuations have been completely avoided.

Figure 5.34 shows the thermal power gain for both scenarios. The thermal power gain of the HTF in the solar field is computed from the laws of thermodynamics according to [41] as

$$\dot{Q}_{th_{gain}} = \dot{m}\bar{c}_p \left(T_{out} - T_{in}\right). \tag{5.3}$$

$\dot{m}$ is the total mass flow rate, T_{out} and T_{in} are the fluid inlet and outlet temperatures, respectively, and $\bar{c}_p$ is the integral average specific heat capacity of the fluid between both temperatures. The value of $\dot{Q}$ is computed for each time step and integrated in time to compute the total energy output of the solar field. In Figure 5.34 the thermal power collected by the solar field with and without valve control and the power difference between both scenarios, as well as the total produced thermal energy, are shown. The proposed control strategy resulted in approximately 2 % increase in the total produced thermal energy. This increase is due to the reduced defocusing instances as a result of manipulating the flow rate

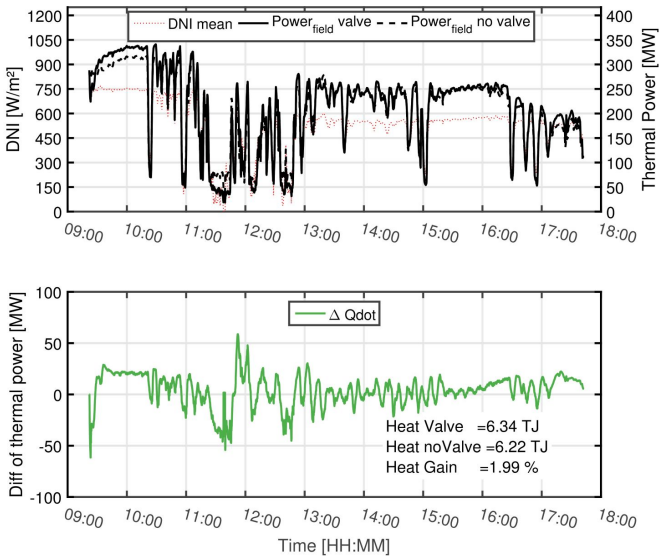

Figure 5.34. [Top]: Comparison of thermal power gain in the solar field between valve-controlled (solid) and no valve-controlled (dashed) control strategies. The dotted red line shows the mean DNI on the field. [Bottom] The difference in thermal power gain between both strategies. The heat energy from integrating the power curves is also stated.

during transient conditions. However, the exact value of the energy gain strongly depends on the parameters set to control the valves and the defocusing. Moreover, the proposed controller concept resulted in a notable drop in produced power during cloud passage that block the sun irradiation at around 11:30 and 12:40. The reason is that the main goal of the controller is to stabilize the outlet temperature during DNI drops and not maximize the produced power. This results in closing the loop valves and reducing the flow rate to maintain the temperature during passage of large clouds. Thus, detailed parametric and yield optimization studies need to be executed and the benefits could be evaluated using VSF.

In conclusion, a control strategy based on manipulating loop valves to alter the mass flow in the loops is implemented and used to control the virtual field modelled by VSF. This resulted in an improvement in outlet temperatures stability and increase in thermal power when compared to the standard control strategy without loop valves control. This can result in more robust and economical solar plant operation and control. Further investigations on improved control algorithms and refining the control parameters need yet to be conducted.

5.4 SUMMARY AND CONCLUSION

To summarize this chapter, an automatic flow controller is developed to overcome the excessive defocussing during transient conditions resulting from the basic one. The basic controller is supplemented by an overall focus feedback loop that manipulates the flow. The controller penalties are computed for different test cases belonging to different DNI categories using the performance assessment scheme described in Chapter 4 and compared for both controllers. The automatic controller is able to increase the revenue of the power plant for all transient situations by up to 13 %. However, for clear-sky and thin cloud conditions, the basic controller already does a good job to collect the incident solar energy.

Then a few challenges that such controllers encounter are discussed and their effects on the performance are studied. The controller is found to be robust to systematic errors of up to 10 % in the plant yield model in the FF controller. As for higher errors reaching 25 %, a drop in the controller performance of up to 4 % is observed due to the boundaries imposed to the controller output. In addition, the effect of different system delays on the controller performance is investigated. In general, the controller is able to cope up with system delays of up to 2 min without strongly affecting the plant performance. These test cases also showed that more investigation is needed for the controller tuning parameters to further increase the yield. After that, a small add-on is included to account for automatic solar energy dumping in case the PB is not able to consume all the available thermal energy.

Furthermore, two novel control concepts using nowcasting systems and loop valves are studied. Nowcasting systems provide spatially-discretized DNI maps for the whole area of the solar field. The system can also provide short-term forecasts that are accurate enough to be usable by the solar field controllers. Firstly, only the current irradiance map is used to provide the flow FF controller with more accurate information about the average DNI incident on the solar field. This overcomes the limitation of using local DNI measurements of only a few points, where most of the information about the spatial variation of DNI is lost. This helps the controller to provide more adequate flow to the field and avoid defocusing instances and excessive temperature drop during cloud passages. In particular, the expected increase in revenues are calculated for the different cloud categories, where a surplus of up to approximately 4 % is achieved for scenarios with high cloud traffic. However, no increase in revenues is expected during clear-sky and homogeneous irradiance situations, since the local measurements in weather stations provide sufficiently accurate information about the DNI on the whole field. To generalize this, simulations of whole days excluding start-up and shut-down are performed and the daily revenues are expected to increase by up to 2.2 % for cloudy days. For all the above investigations, the irradiance maps were assumed to be 100 % accurate, but it has been previously shown in Section 5.1.2 that the controller is able to cope with systematic errors in the flow FF controller without having large effect on the plant performance and yield.

Secondly, short-term forecasts of up to 15 min in the current control concept are used. Nevertheless, the performance of the controller dropped for cases where the controller and

system provide real-time action and response. This paves the way for investigations of more advanced control concepts that can better utilize the forecasts, like model predictive control. Alternatively, if the system has some delays of 90 s, the use of the short term nowcasts becomes minutely beneficial for the plant performance. In brief, the implemented control concept is not able to make significant use of the short term forecasts. Further use of forecasts from nowcasting systems during start-up operations is an interesting topic that will be investigated in future work.

In the end, a simple control strategy that considers controlling the flow in the single loops is adopted and tested. The results show tremendous potential for such controllers to overcome disturbances due to transient conditions in the field while stabilizing the field outlet temperature and increasing the thermal energy yield by 2 % for the investigated test case.

6 CONCLUSIONS AND OUTLOOK

Optimization of both components and processes could cut-down the costs and make CSP more economically attractive. The work in this thesis is a step towards providing the necessary tools for optimizing the process control and potentially increasing the yield of such power plants during transient processes. It can be divided into three streams. The main stream is the development and implementation of the simulation model that can efficiently represent the physical behaviour of parabolic trough power plants. The second stream is the implementation of control strategies to automatically operate the solar field in realistic weather conditions with cloud passage and solar field start-up. Finally, the tool is used to test various novel control concepts including the usage of nowcasting systems and control valves on every loop. In addition, a performance assessment scheme for comparing the different control concepts is defined.

This work presents the simulation tool developed to study the transient behaviour of line-focus solar thermal power plants with single-phase HTF, the Virtual Solar Field, VSF. A thorough literature review of available dynamic models reveals the lack of detailed solar field models that consider spatially-varying conditions on the field within reasonable computation times. For this, the model needs to simulate every loop in the field independently while coupling the thermal and flow conditions to get an accurate representation of the real physical system. The main focus of the work is on solar fields using parabolic trough collectors. The model equations, assumptions and implementation are described. The model is divided into two parts due to the different time scales between the thermal and the flow aspects. Therefore, a computationally efficient static hydraulic model is used to compute the flow distribution in the parallel pipes according to the pressure loss in each pipe. This saves computation time, as there is no need to solve the momentum balance equations for the finely-spatially discretized thermal model, which takes care of the heat transfer in the system.

The validation of the different model components shows good agreement with analytical and other simulation models. The model is validated against operational data from a full-scale commercial solar field, namely Andasol-III. The results show very good agreement in terms of reproducing the transient behaviour in the field, as well as the variation in temperatures and flow distribution between the different loops. The limitations of the tool are also discussed and the sensitivity to layout details and parameterization of component models in the actual solar field is investigated.

In conclusion, the physical and transient behaviour of parabolic trough power plants can be accurately simulated using correlations for heat transfer coefficients and flow friction factors. In addition a computationally efficient implementation is achievable by separating the flow distribution and heat transfer problems while making use of the different time scales between both effects. To be able to simulate solar fields in realistic situations, a complete control algorithm was also implemented.

Large full-scale solar fields are exposed to numerous transient situations that hinder the performance and reduce the energy yield. A convenient balance of flow and focus regulation is needed as skilled and experienced operators try to minimize the losses associated with passing clouds, especially in situations with high spatial variability of the DNI. The second part of this thesis focuses on the implementation of automatic solar field controllers. Firstly, state-of-the-art controllers composed of a feed-forward mass flow controller and a feed-back temperature controller have been implemented. The controllers are tested for different DNI categories ranging from clear-sky to large thick clouds with some gaps that result in high spatial variability of the DNI on the field and show good performance in some cases. However, the controller failed to achieve acceptable performance in cases with high spatial variability of irradiance. Significantly high defocusing of collectors is maintained for prolonged periods of time. This problem has been also reported by solar field operators, such that manual intervention is needed to compensate that effect.

As a result, the controller has been improved by adding a total field focus loop to impose higher flow mass flow in the field in case of excessive defocusing. A performance assessment scheme is developed to comprehensively compare different control concepts. Economic penalties are deducted from the theoretical revenue at off-design operation. The improvement in the controller resulted in a revenue increase of up-to 14 % for individual weather categories. The robustness of the controller to different modelling errors and inaccuracies of the input signals is tested. The controller can maintain the performance despite of systematic error in the measurement signals of up-to 25 %. Since solar fields are subject to a wide range of operation conditions, the controller parameters need to be adequately tuned. It has been found that adaptive parameters are needed for stable response of the field temperature controller as the wide operation range of the systems strongly affects the system time constant and gain.

The investigations in the second part of the thesis demonstrate that the VSF can efficiently be used to test and improve controller setup. The goal of the implemented automatic controller is to reduce defocus instances, then regulate the field outlet temperature providing stable field output. However, it has been shown for cases with very high spatial variability that this does not necessarily increase the revenue of the plant. Further improvement in response and the energy yield is expected when controllers are specifically tuned depending on the category of irradiation. The performance assessment scheme provides extensive and compact information about the field operation.

In the third stream, initial efforts are made in the direction of solar field control optimization through testing the feasibility and benefit of novel control concepts that have never been tested on real power plants. An estimate of the economical benefit of adding control features, such as nowcasting systems and loop valves is calculated. It has been found that the stretch of the solar field and the spatial variability of the DNI have a profound effect on the plant performance that cannot be substituted by single point measurements or by scaling average values. Then, DNI maps from nowcasting systems are used to improve the weather condition input to the flow feed-forward controller instead of only a few DNI measurements from weather stations. This resulted in an increase in the plant yield of up to 4 %, which is significant for the size of the plants.

To decrease the losses further, VSF enabled testing the benefit of adding controllable loop valves to manipulate the flow in the single loops depending on the local solar irradiance and temperatures. Initial studies have shown that the field outlet temperature can be kept constant, even during strong transient situations, and the daily energy yield of the solar field was increased by 2 % for the examined test case. Thus, it can be concluded that spatially-distributed disturbance requires spatially-distributed control action to eliminate its negative effects on the performance. However, a more extensive loop valve controller needs to be coupled with the main flow controller to avoid over-determination in the control system.

In conclusion, the existence of a detailed and validated transient simulation tool allows programming of different control concepts in various weather conditions. Also the performance assessment scheme provides comprehensive comparison by translating the yield gain into a monetary revenue while showing a distribution and weight of the different losses. The revenue value is to be considered as a comparative value only. The exact revenue stream depends on other economic factors such as O&M costs and electricity prices.

Future outlook

In this section follow-up work is recommended for the three streams mentioned above. Regarding the physical model, thermal inertia of the header walls and insulation material can be considered. This would more precisely represent the solar field during start-up and shutdown as the effect is expected to be more significant. Also higher order approximations can be implemented for cases of direction-reversing flows. To achieve this, the implementation of the hydraulic part of the solver will need to be accordingly adjusted. This is only relevant in case of overnight cool-down simulations or if solar field drainage is to be simulated for example in case of molten salt fields. In addition, more accurate valve models are required, as the characteristics of an orifice do not resemble those of the common globe or needle valves used in commercial power plants, especially for valve opening above 50 %.

The accuracy, robustness and little computation time taken by the field simulation model, VSF, allows for testing more advanced control concepts. More elaborate investigations on the spatial variability of DNI on the controller performance are expected to further

increase the revenue of a solar field. This can be achieved by tuning the controllers according to the current and future irradiation condition on the field. Furthermore, optimization of plant output could be performed through multiple runs and trials of different control parameters paving the way for model predictive control with DNI forecasts from nowcasting systems.

It would also be interesting for annual yield models to define expected loss values associated with the different weather categories and their occurrence during the year. Annual yield models rely mainly on simplified solar field models. A more detailed model will give better estimates of the actual yield. By associating corresponding loss factors, the annual yield and feasibility of CSP projects can be more accurately computed, securing more investments [25].

VSF could also be used during the design phase of the plant to test the performance of the different components or to study the plant behaviour and its feasibility under specific critical conditions. An interesting application is using the tool to identify critical low temperature or flow zones in the power plant. This is particularly important for molten salt applications to avoid freezing and reduced heat transfer due to laminar flow. Additionally, operation using new HTFs, such as silicon-based thermal oils, can be tested and evaluated before implementing in actual power plants.

Finally, during commissioning and operation of the plant, VSF could be used to facilitate day-to-day operation and monitoring. For example, VSF could calculate the valve settings needed to hydraulically balance the power plant according to the different seasons. In addition, it could be used as a reference for a plant performance monitoring system and report defective components or loops through comparing their expected and actual performances.

A FLUID PROPERTIES

Since the temperatures of the HTF vary significantly as it is heated or cooled, all fluid properties are computed as a function of the temperature using fitted data in literature. Figure A.1 shows the temperature dependence of density, viscousity, specific heat capacity, and heat conductivity according to [82] for Therminol®, [21] for DOWTHERM® A , [94] for Solar Salt, and [77] for HitecXL CaNaK molten salt (CaNaK Siegel).

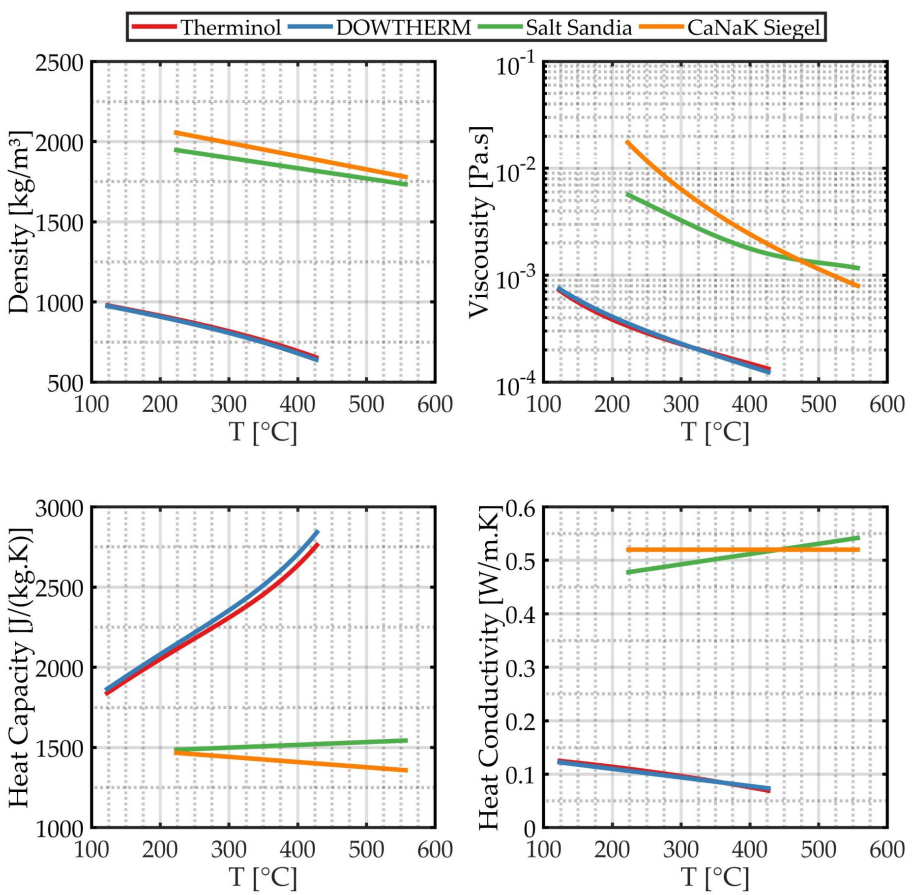

Figure A.1. Fluid properties function of temperature

B VISCOUS FLOW IN PIPES

An approximation of the head losses due to fluid shear stresses in pipe flow is expressed by a correlation relating the losses with the velocity of the fluid. This correlation is called the Weisbach equation and is given as

$$h_f = f\frac{L}{d}\frac{v^2}{2g} \tag{B.1}$$

where f is the Darcy friction factor which is computed using various empirical approximations to the Moody Chart depending on the Reynolds number of the flow as in [30, 86]. L, d, and v represent the pipe length and diameters and the fluid mean velocity, respectively. g is the coefficient of gravity.

The Darcy friction factor is computed using one of the following methods depicted in Figure B.1 and listed below according to the flow regime and approximation.

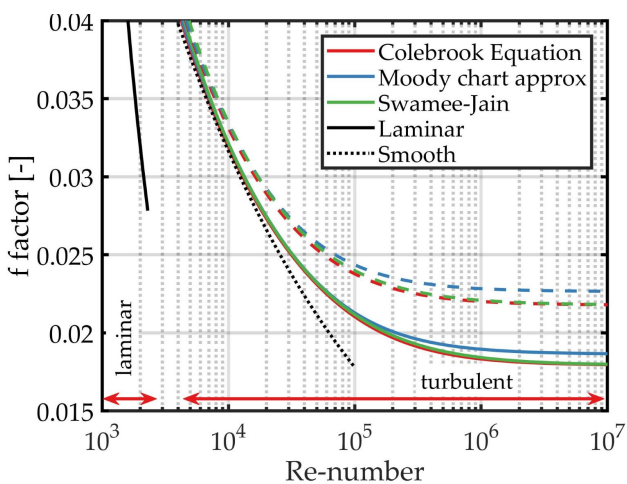

Figure B.1. Friction factor computations for $\epsilon/d = 6.8 \cdot 10^{-4}$ [solid] and $\epsilon/d = 1.5 \cdot 10^{-3}$ [dashed] as examples.

B.1 LAMINAR FLOW

For $Re < 2300$, the friction factor for laminar flow is calculated as a function of the Reynolds number in [80] as

$$f = \frac{64}{Re}. \tag{B.2}$$

B.2 TURBULENT FLOW IN SMOOTH PIPES

If the pipe is assumed to be smooth, the friction factor is computed according to the Blasius relation for $4000 < Re < 10^5$ as

$$f = \frac{0.3164}{Re^{0.25}} \tag{B.3}$$

B.3 TURBULENT FLOW IN ROUGH PIPES

For rough pipe walls, the friction factor computation becomes more complicated depending on the roughness of the pipe, ϵ, as well as the Re-number and dimensions of the pipe. The most accurate estimate of the friction factor is provided by the Colebrook equation.

Colebrook-White equation

The Colebrook-White equation is a nonlinear equation and needs to be solved iteratively. The equation is given by

$$\frac{1}{\sqrt{f}} = -2\log\left[\frac{(\epsilon/d)}{3.7} + \frac{2.51}{Re\sqrt{f}}\right]. \tag{B.4}$$

Moody Chart approximation

Due to the nonlinearity in the Colebrook equation, it was plotted for different values of roughness in the famous plot known as the Moody chart. To facilitate the numerical processing of such charts, numerous approximations have been derived. One approximation of the Moody chart is given by the following relation summarized in [28]

$$f = 0.0055 + 0.0055\left(2\times 10^4\frac{\epsilon}{d} + \frac{10^6}{Re}\right)^{1/3} \tag{B.5}$$

The relation is valid for $4000 < Re < 5\cdot 10^8$ and $0 < \frac{\epsilon}{d} < 0.01$.

Swamee-Jain approximation

Another approximation of the Colebrook-White equation is

$$f = \frac{0.25}{\left(\log\left[\frac{(\epsilon/d)}{0.37} + \frac{5.74}{Re^{0.9}}\right]\right)^2}. \tag{B.6}$$

This approximation is valid for $5000 < Re < 10^8$ and $10^{-6} < \frac{\epsilon}{d} < 0.05$.

C VALVE CHARACTERISTIC CURVES

As discussed in Section 2.1, in the initial implementations of VSF, valves are represented by orifices to facilitate the computation of the pressure losses as function of valve opening and vice-versa. However, it was also necessary to implement more realistic valve models that accurately describe installed valves according to the manufacturers' data sheets.

By rearranging Equation (2.3) in the form $\Delta p_{or} = K_{orifice}\dot{m}^2$ as in Equation (2.2) and substituting for Δp_{or}, we compute the hydraulic resistance of the orifice, $K_{orifice}$, as:

$$K_{orifice} = \frac{\left(1-\beta^{1.9}\right)\left(1-\beta^{4}\right)}{2\left(c_D A_{or}\right)^2 \rho}. \tag{C.1}$$

Industrial valves are characterized by the valve flow coefficient, K_v, as mentioned in [84, 86]. K_v is defined as the volume flow rate of water that flows through the valve with 1 bar differential pressure across the valve. It can be calculated as

$$K_v = \dot{V}\left[\frac{m^3}{h}\right]\sqrt{\frac{1\,[bar]}{\Delta p_v\,[bar]}\frac{\rho}{\rho_w}}, \tag{C.2}$$

where ρ_w is the reference density of water equal to $1000\,kg\,m^{-3}$. The units of each term in the above equation are written in square brackets.

To transform this form to the common form used in VSF, as $\Delta p_v = K_{v,SI}\dot{m}^2$ with SI-units, we reach the form

$$K_{v,SI} = \frac{10^5 \cdot 3600^2}{\rho\rho_w K_v^2}. \tag{C.3}$$

Similarly, the K_v value can be computed from the mass flow rate and required pressure loss in the valve as

$$K_v = \frac{3600\cdot\sqrt{10^5}}{\sqrt{\rho_w}}\dot{m}\left[\frac{kg}{s}\right]\sqrt{\frac{1}{\Delta p\,[bar]\,\rho}} \tag{C.4}$$

To compute the K_v value of an orifice to produce Figure 2.4, Equations 2.3 and C.2 are combined and the K_v value is given as

$$K_v = \frac{3.6\cdot 10^4}{\sqrt{\rho K_{orifice}}}. \tag{C.5}$$

D COEFFICIENT OF CONVECTIVE HEAT TRANSFER

The heat transfer mode is considered a mixture of forced and free convection. Hence, the heat convection coefficient, as described in Equation (2.29), is computed as

$$\alpha_f = \frac{\lambda}{d_i}\left(Nu_{forced}^n + Nu_{free}^n\right)^{1/n} . \tag{D.1}$$

The Nusselt number for forced convection is given in terms of the Reynolds and Prandtl numbers according to the Dittus-Boelter equation[37] as

$$Nu_{forced} = 0.0235 \cdot Re^{0.8} \cdot Pr^n \tag{D.2}$$

for turbulent flows, where $n = 0.4$ if the fluid is being heated up or $n = 0.3$ if it is being cooled down. For laminar flows the Nusselt number is computed as

$$Nu_{forced} = 0.32 \cdot Re^{0.61} \cdot Pr^{0.31} . \tag{D.3}$$

The Pr-number is the ratio of the viscous diffusion rate to the thermal diffusion rate given by

$$Pr = \frac{\mu \cdot c_p}{\lambda_f} . \tag{D.4}$$

Another more accurate method for computing the Nu-number for forced convection is the Gnielinski correlation given by [37]

$$Nu_{forced} = \frac{(f/8)(Re - 1000)Pr}{1 + 12.7(f/8)^{0.5}\left(Pr^{2/3} - 1\right)} , \tag{D.5}$$

where f is the Darcy friction factor.

The Nu-number for free convection is given according to [44]

$$Nu_{free} = \frac{2}{-\ln\left[1 - \frac{2}{\left[\left(\left[\left(\frac{2}{1-\exp^{-0.25}}\right)^{5/3} + \left(0.587Ra_d^{0.25}\right)^{5/3}\right]^{3/5}\right)^{15} + \left(0.1Ra_d^{1/3}\right)^{15}\right]^{1/15}}\right]} \tag{D.6}$$

Ra_d is the Rayleigh number representing the significance of free convection. Rayleigh number is defined as the product of Prandtl and Grashof numbers, $Ra_d = Gr_d Pr$. The Grashof number the ratio of buoyancy forces to viscous forces and is given by

$$Gr_d = \frac{g\beta_v \, abs(T_w - T_f) D_{in}^3}{\nu^2} , \tag{D.7}$$

where β_v is the volumetric coefficient of thermal expansion given by

$$\beta_v = -\frac{1}{\rho}\frac{\partial \rho}{\partial T}\,. \tag{D.8}$$

E SOLAR THERMAL ENERGY POWER PLANT COMPONENTS

Common insulation materials for header pipes used are MinWool-1260® and THERMO-12 Gold® for the cold and hot headers, respectively [30]. The thermal conductivities as listed in [54, 83] are

$$\lambda_{\text{minWool}} = 1.96367 \times 10^{-7} \cdot T_m^2 + 1.02156 \times 10^{-4} \cdot T_m + 0.0291031 \quad \text{(E.1)}$$

$$\lambda_{\text{thermoGold}} = 4.53117 \times 10^{-8} \cdot T_m^2 + 1.11288 \times 10^{-4} \cdot T_m + 0.0455104 \quad \text{(E.2)}$$

where T_m is the mean temperature in the insulation material. To compute the the outer temperature of the insulation material, T_{insul} as illustrated in Figure E.1, the conducted heat within the insulation walls can be written as

$$\dot{q}_{cond} = \frac{2\pi}{\ln\left[\frac{D_{out}+2t_{ins}}{D_{out}}\right]} \lambda_{ins} \left(T_w - T_{ins}\right) , \quad \text{(E.3)}$$

where D_{out} is the outlet pipe diameter and $\dot{q}_{cond}$ is equated to the sum of radiated and convected heat to the ambient, such that

$$\dot{q}_{loss,h} = \dot{q}_{rad} + \dot{q}_{conv} , \quad \text{(E.4)}$$

$$\dot{q}_{rad} = \varepsilon \sigma \pi \left(D_{out} + 2t_{ins}\right) \left(T_{ins}^4 - T_{amb}^4\right) , \quad \text{(E.5)}$$

$$\dot{q}_{conv} = \alpha_a \pi \left(D_{out} + 2t_{ins}\right) \left(T_{ins} - T_{amb}\right) . \quad \text{(E.6)}$$

ε is the emissivity of the external shell of the insulation material and σ is the Stefan-Boltzmann constant equal to $5.6703 \times 10^{-8}\, W\, m^{-2}\, K^{-4}$. α_a is the convective heat transfer coefficient due to external flow of air on the pipes. It is computed using same methods listed in Appendix D.

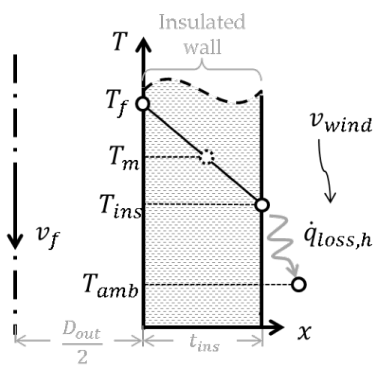

Figure E.1. Sketch of the temperature distribution within the header insulation.

F DETAILED SIMULATION RESULTS

In this appendix, more simulation results are shown.

F.1 CLEAR-SKY (CS)

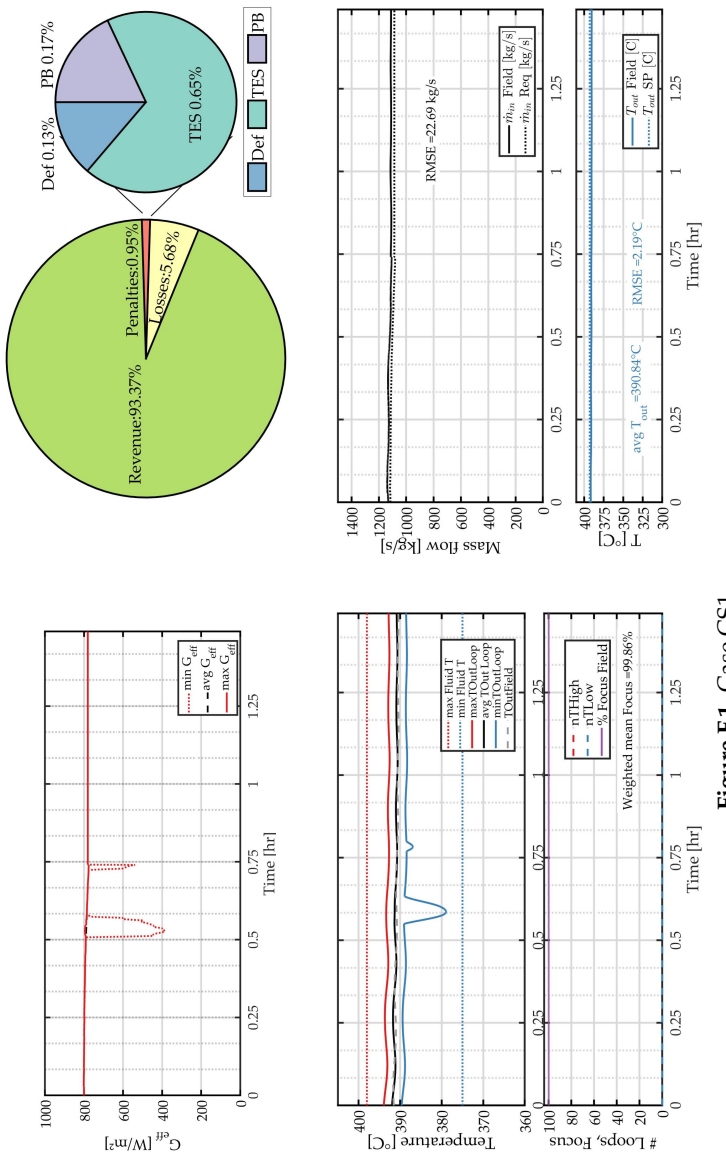

Figure F.1. Case CS1.

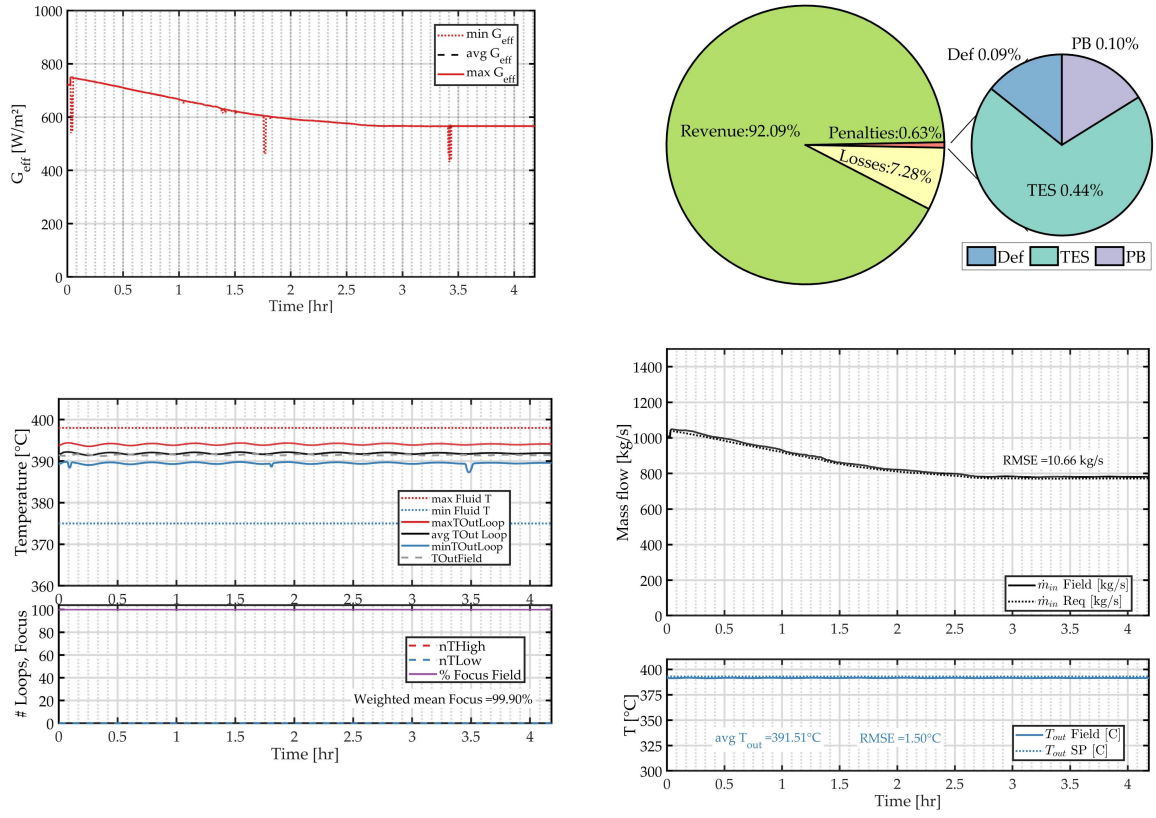

Figure F.2. Case CS2.

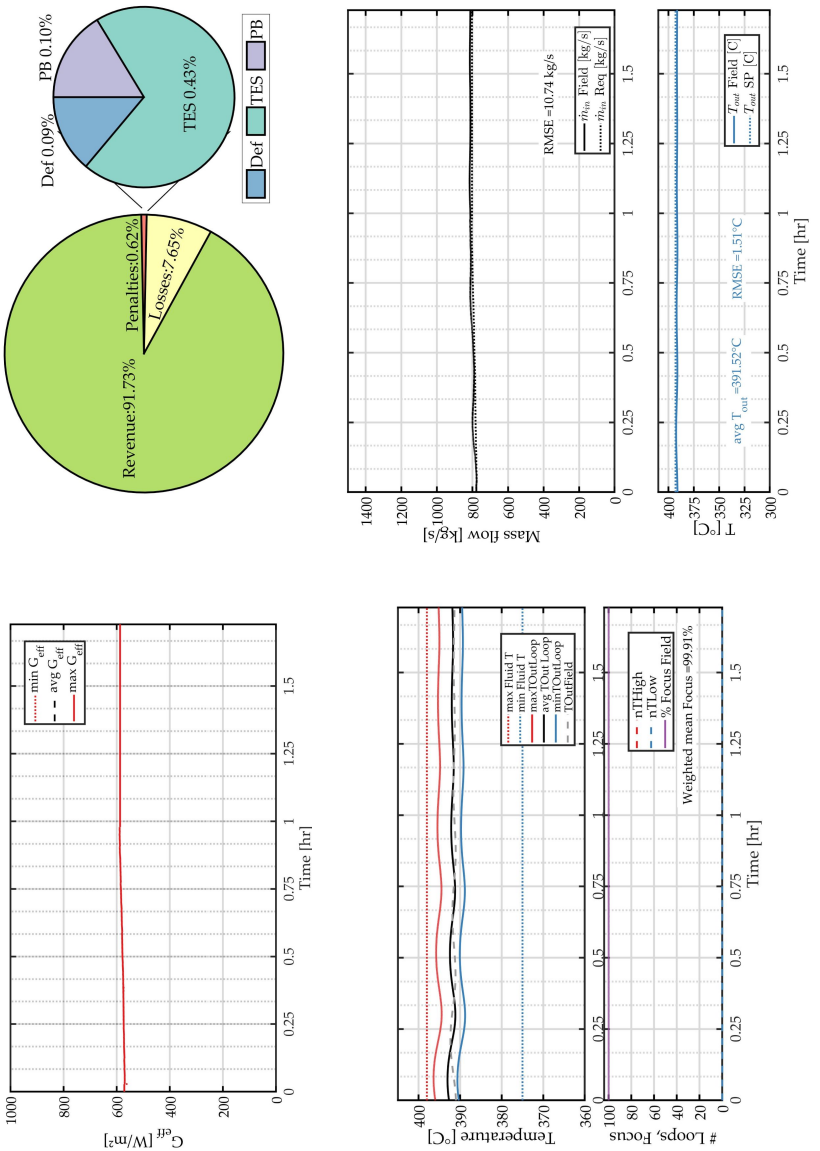

Figure F.3. Case CS3.

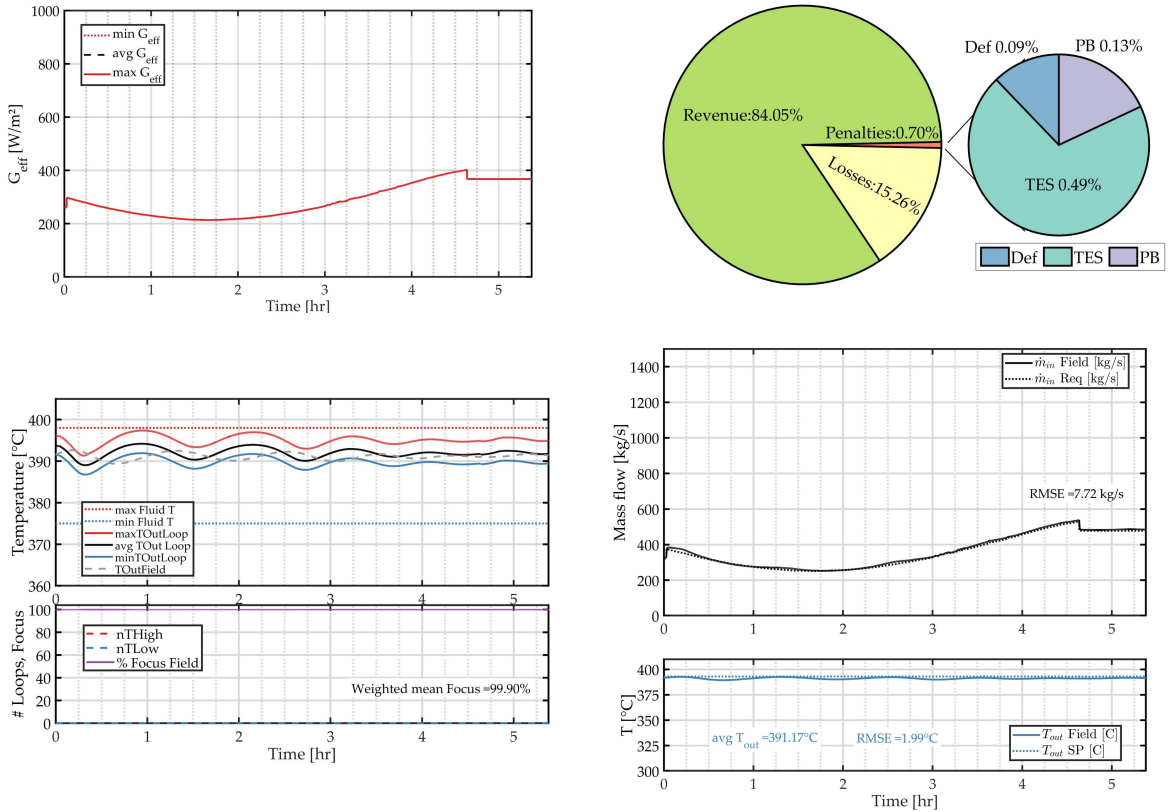

Figure F.4. Case CS4.

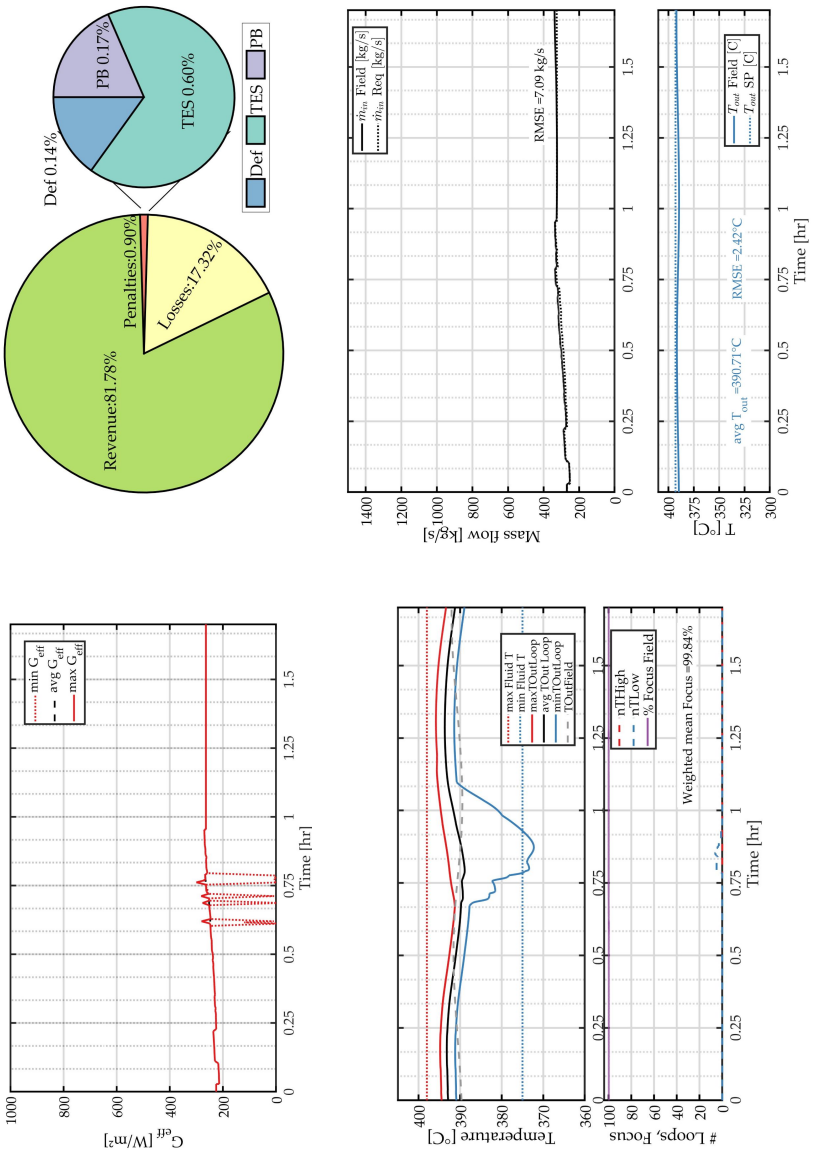

Figure F.5. Case CS5.

F.2 RANDOM-QUICK CLOUDS (RQ)

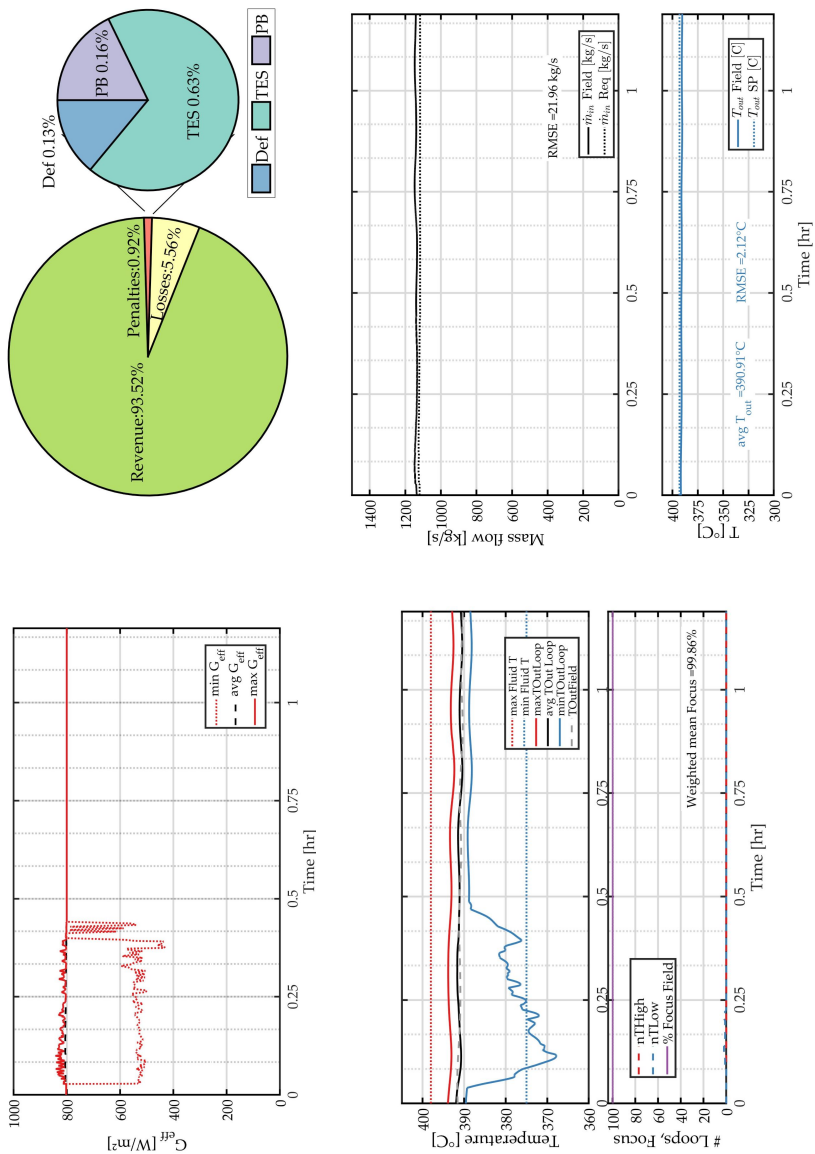

Figure F.6. Case RQ1.

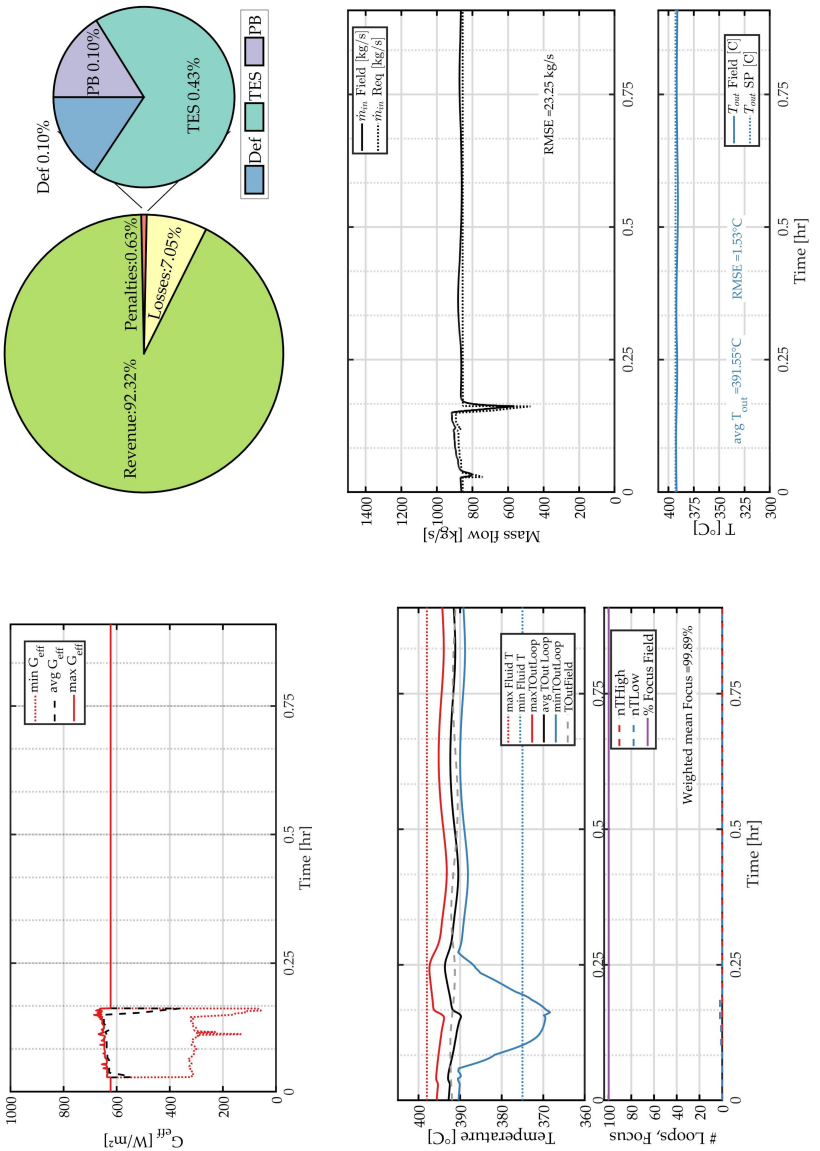

Figure F.7. Case RQ2.

F.3 THICK SMALL CLOUDS (THKS)

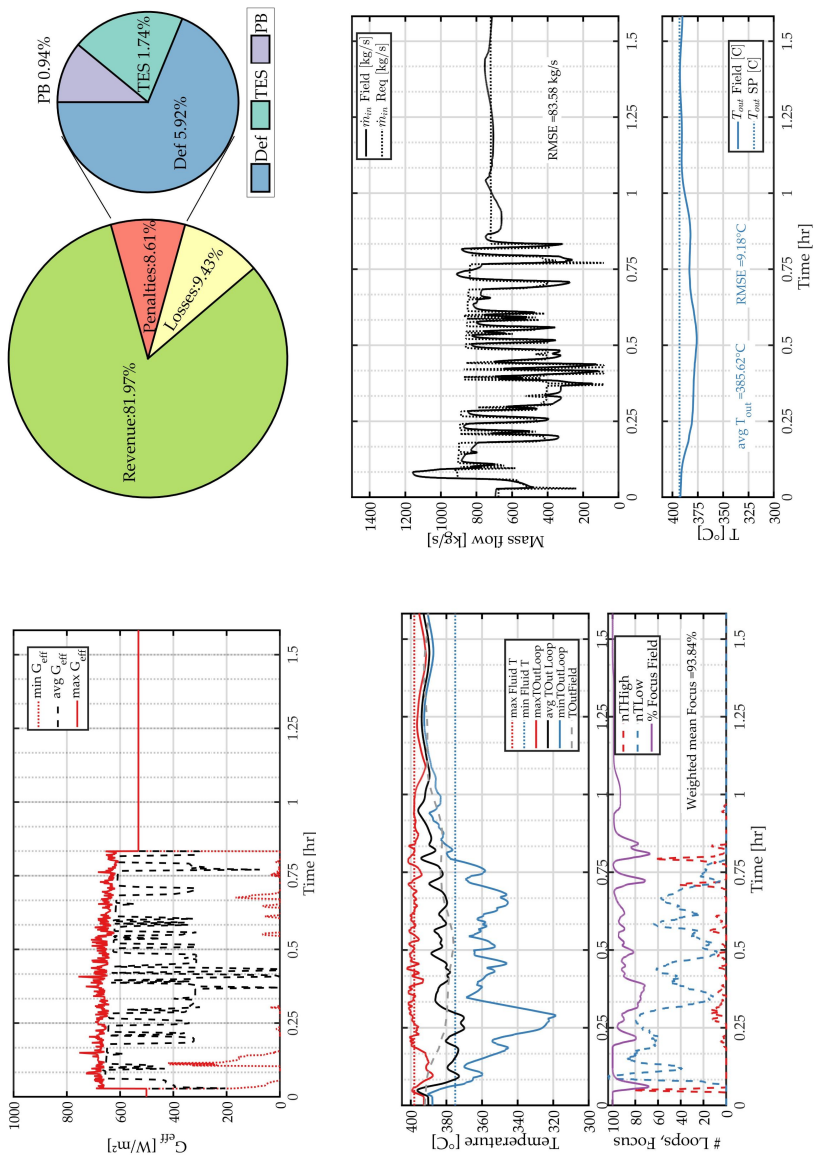

Figure F.8. Case ThkS2.

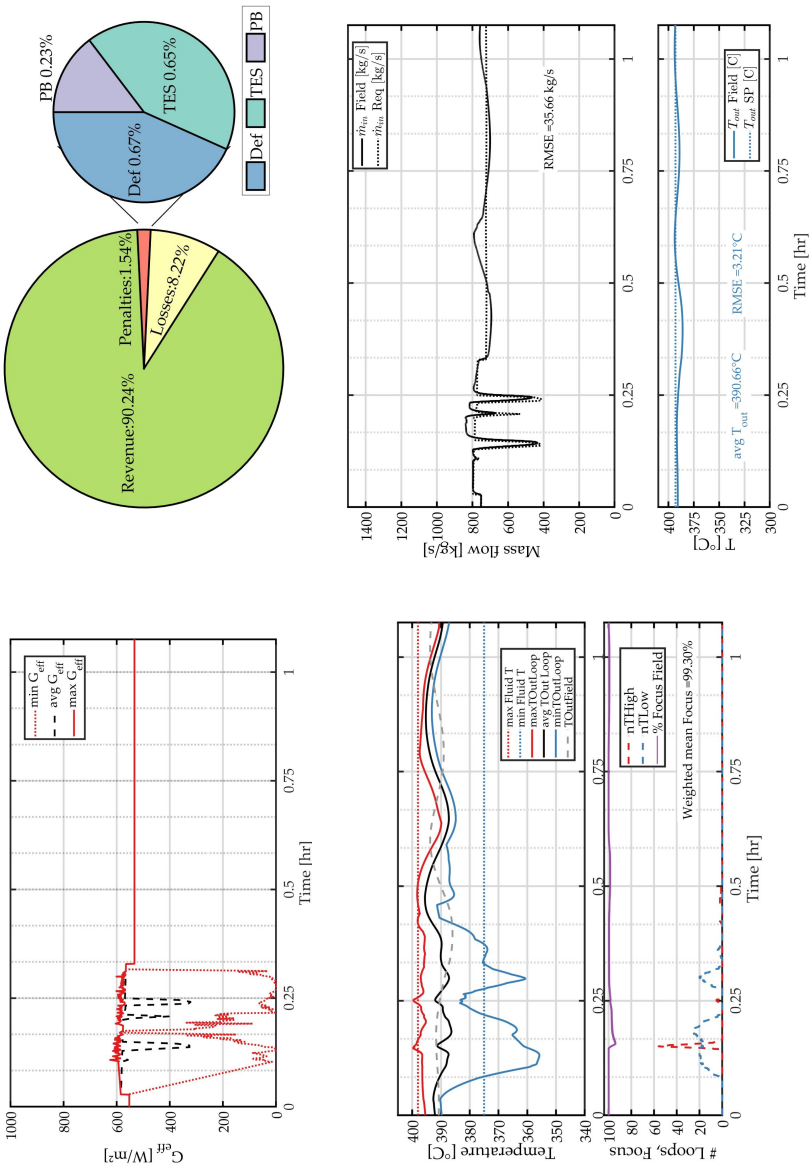

Figure F.9. Case ThkS3.

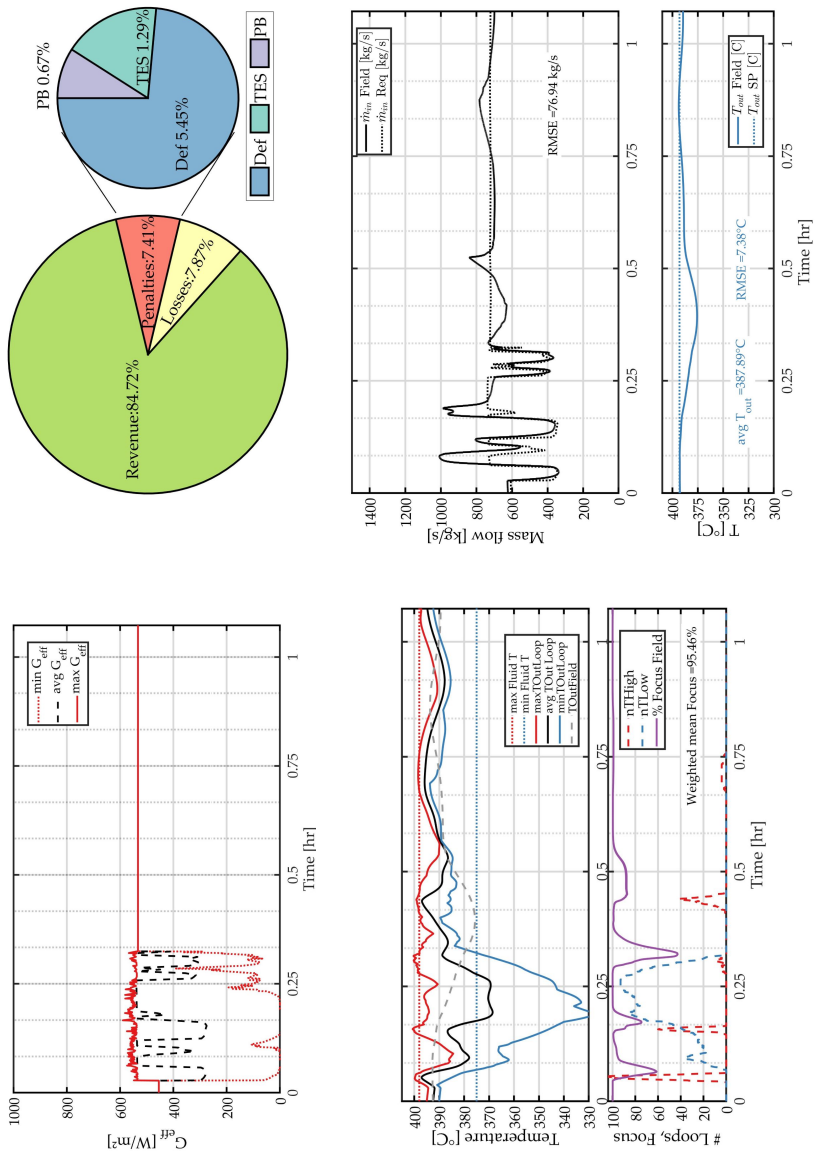

Figure F.10. Case ThkS4.

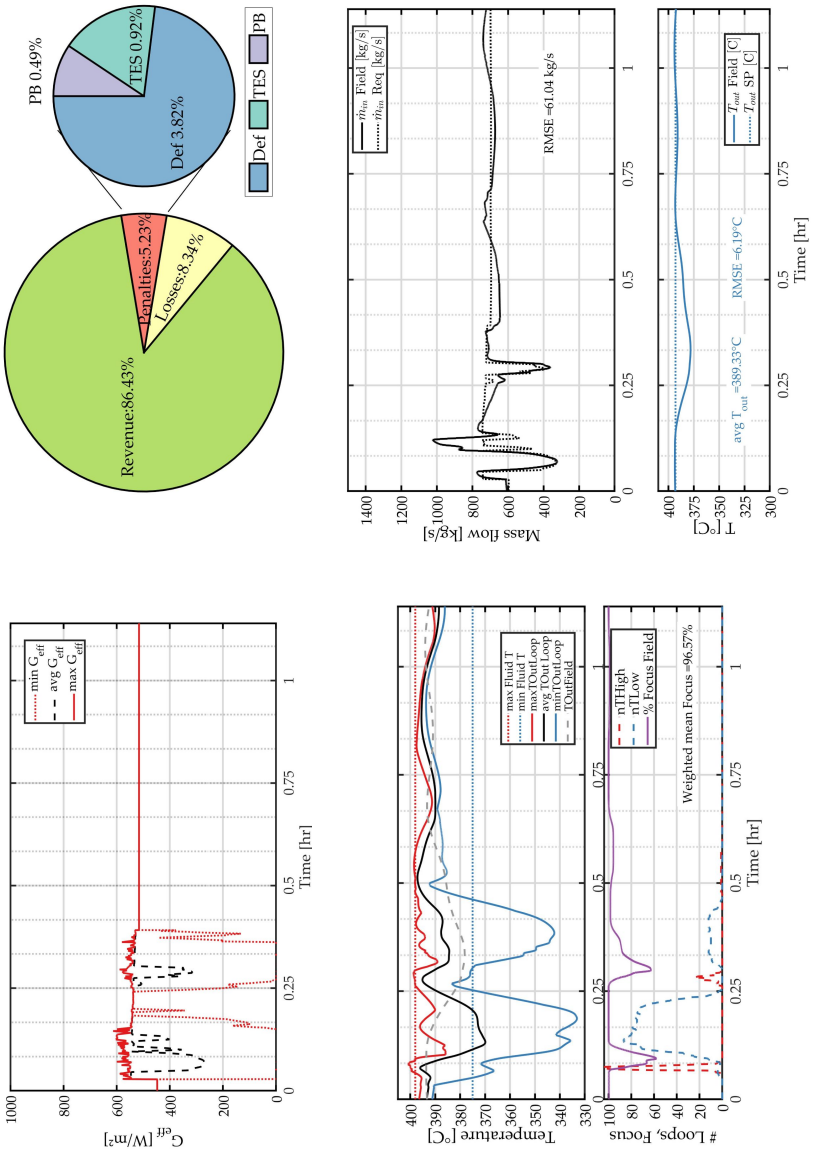

Figure F.11. Case ThkS5.

F.4 THICK LARGE CLOUDS (THKL)

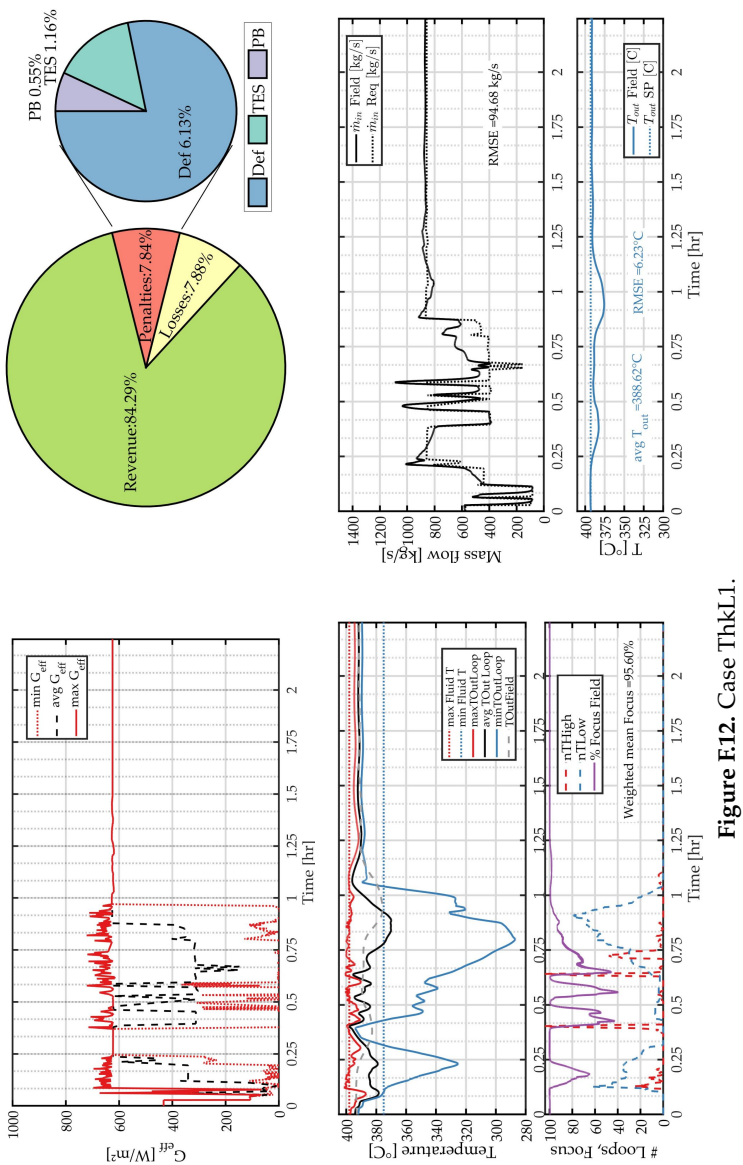

Figure F.12. Case ThkL1.

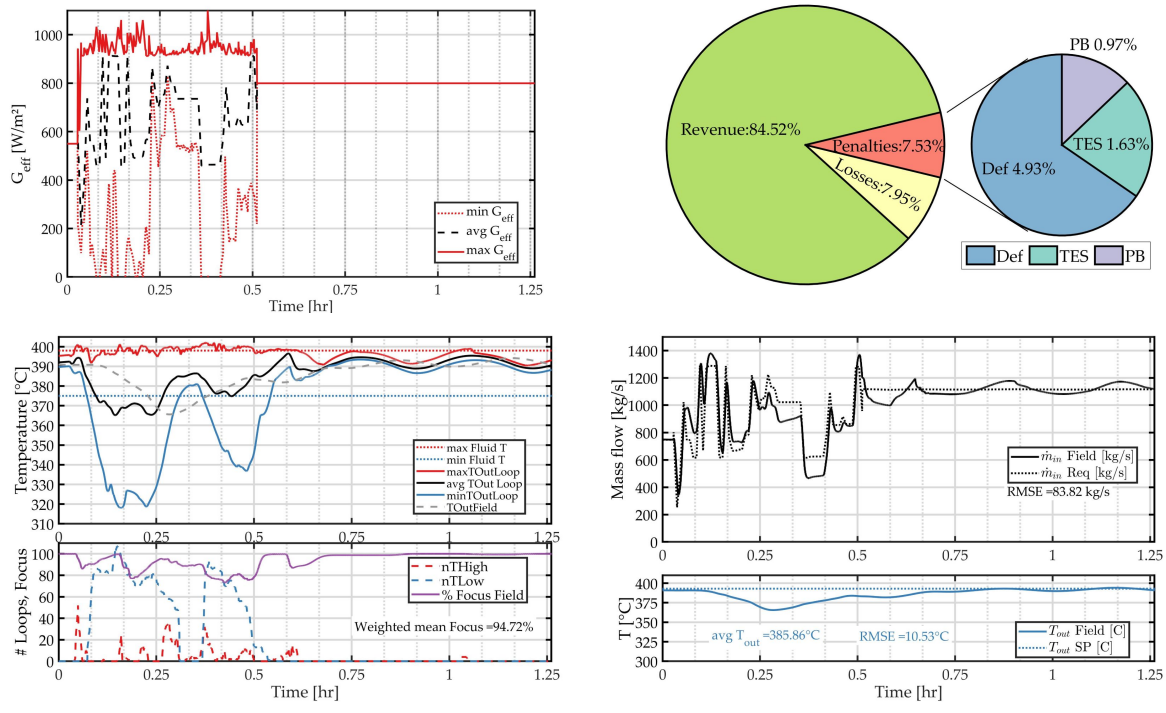

Figure F.13. Case ThkL2.

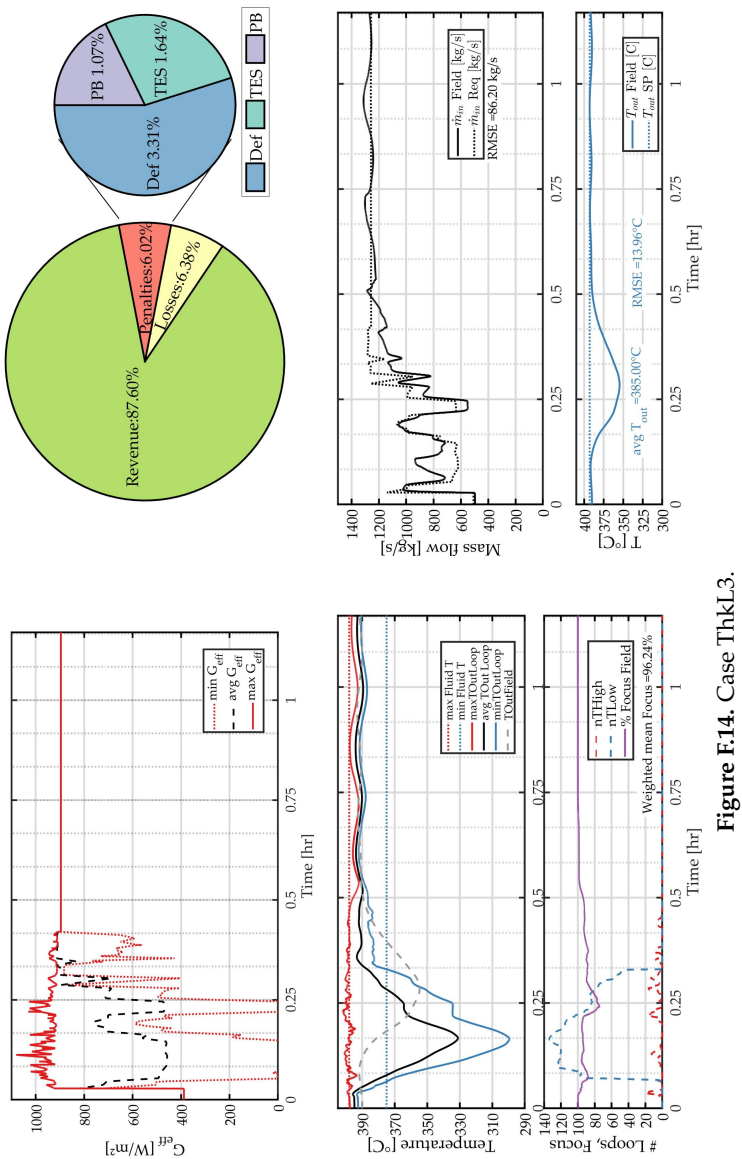

Figure F.14. Case ThkL3.

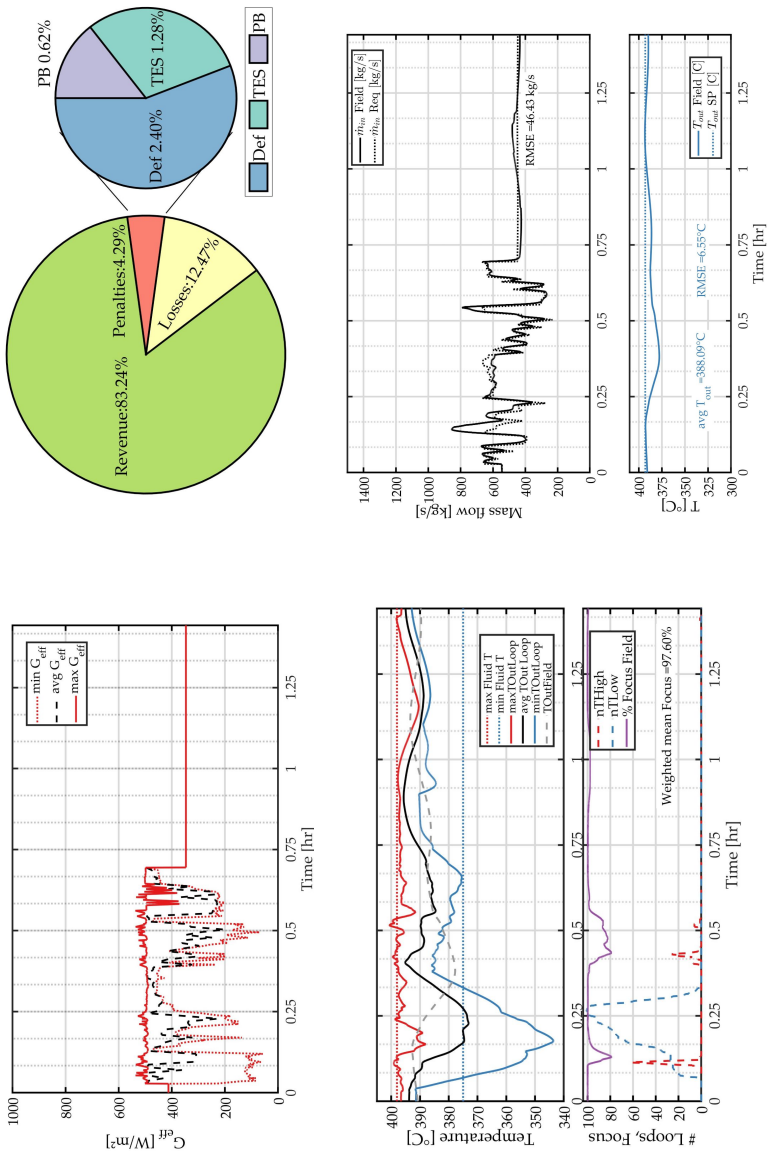

Figure F.15. Case ThkL4.

F.5 THICK CLOUDS WITH GAPS (THKH)

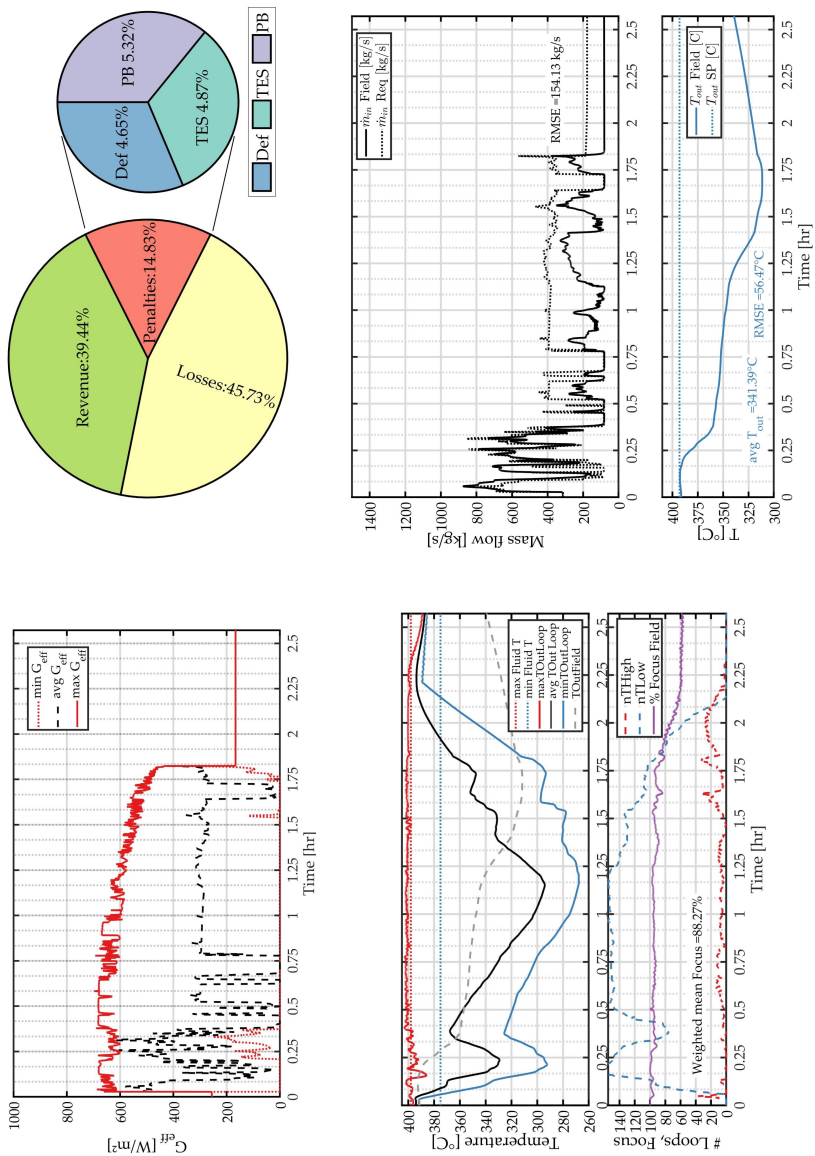

Figure F.16. Case ThkH1.

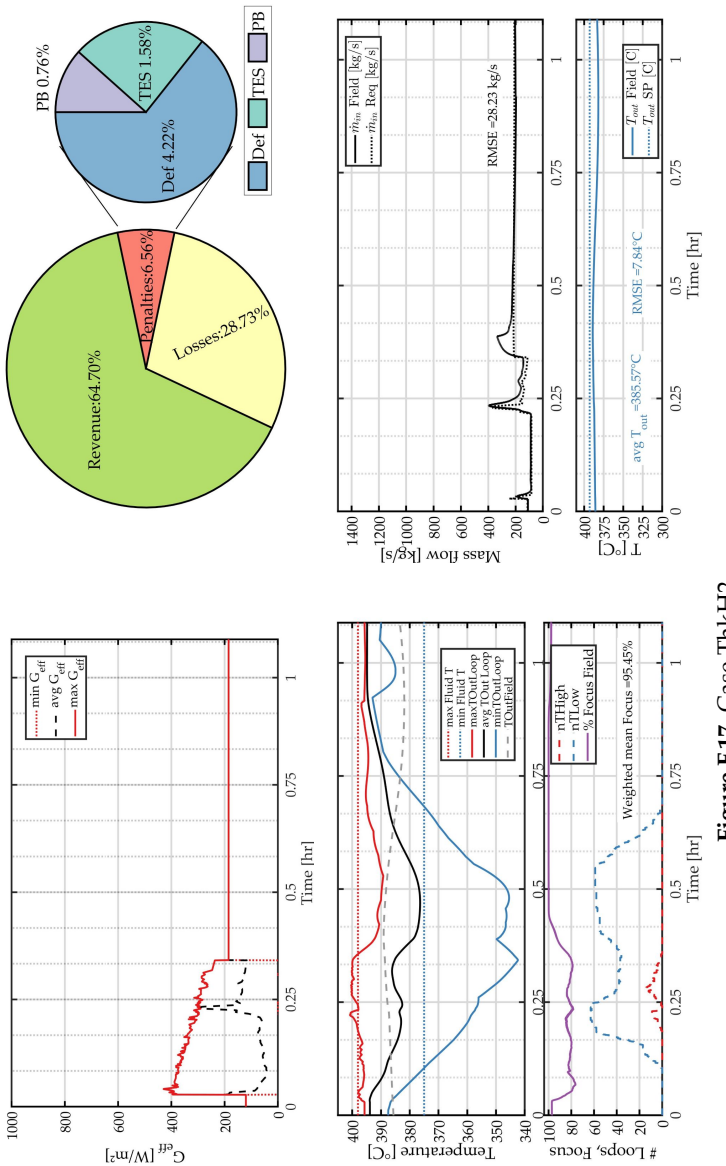

Figure F.17. Case ThkH2.

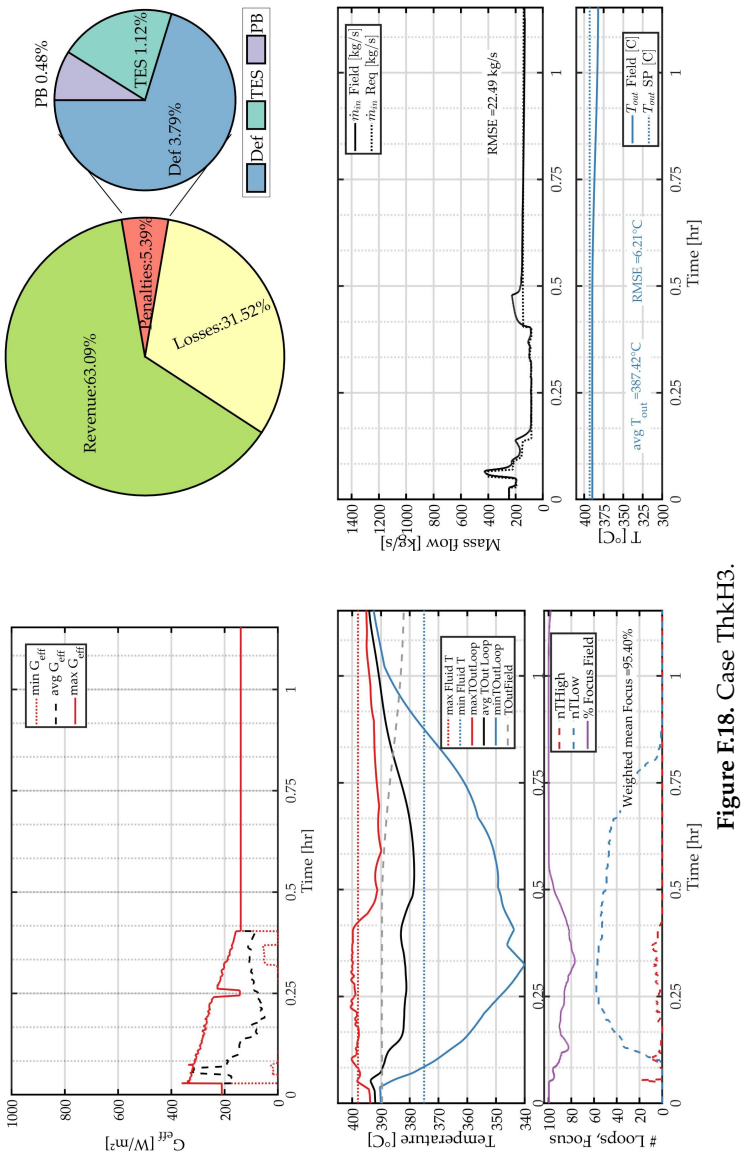

Figure F.18. Case ThkH3.

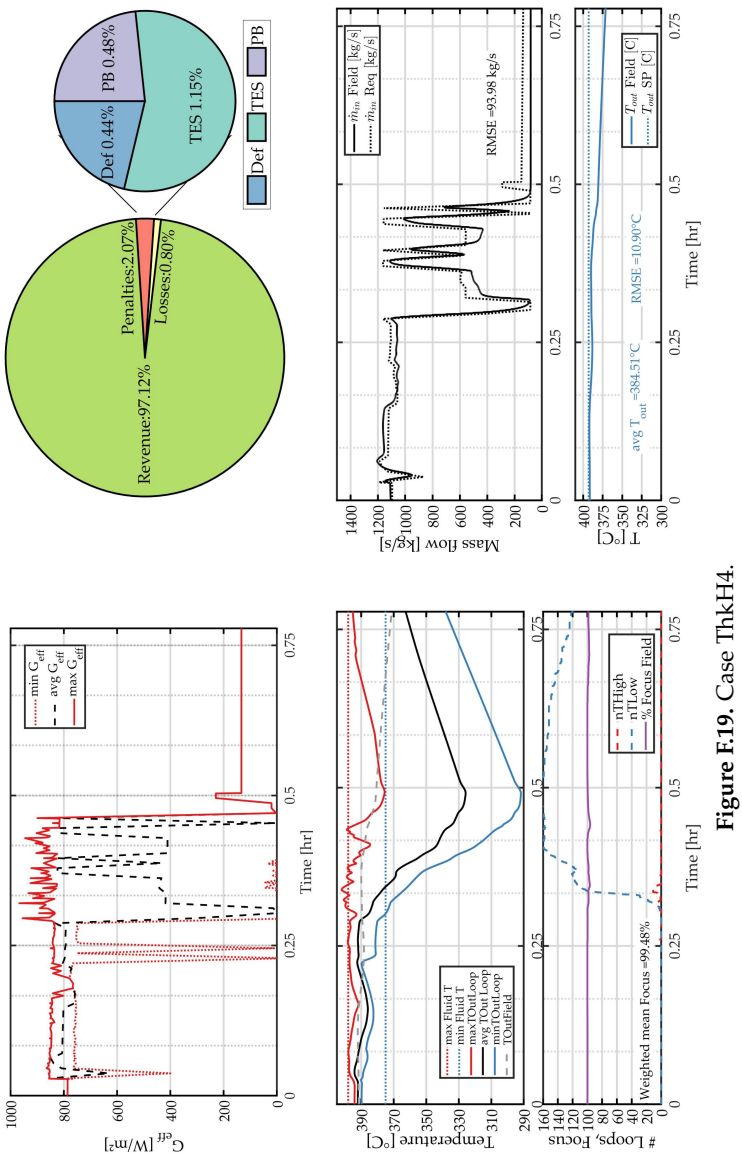

Figure F.19. Case ThkH4.

F.6 WHOLE DAY SIMULATIONS

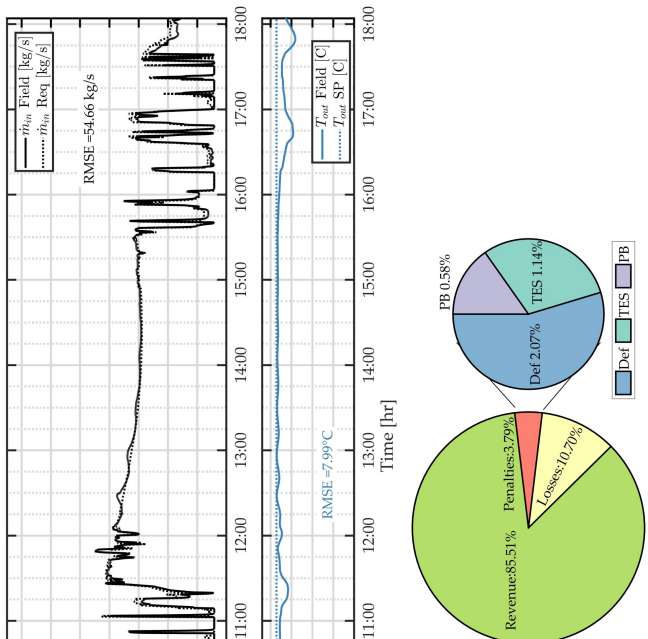

Figure F.20. Case WD1.

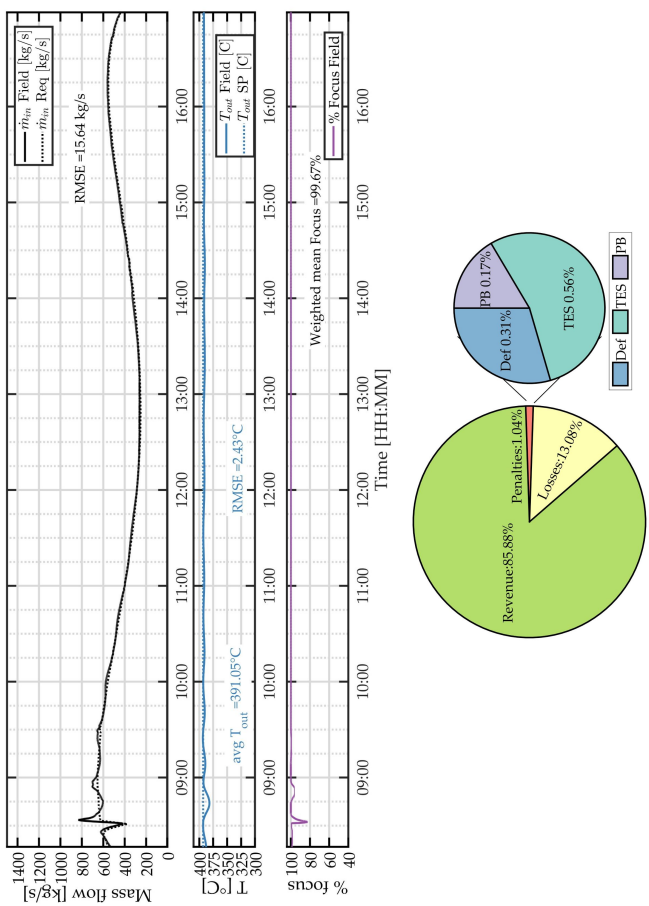

Figure F.21. Case WD2.

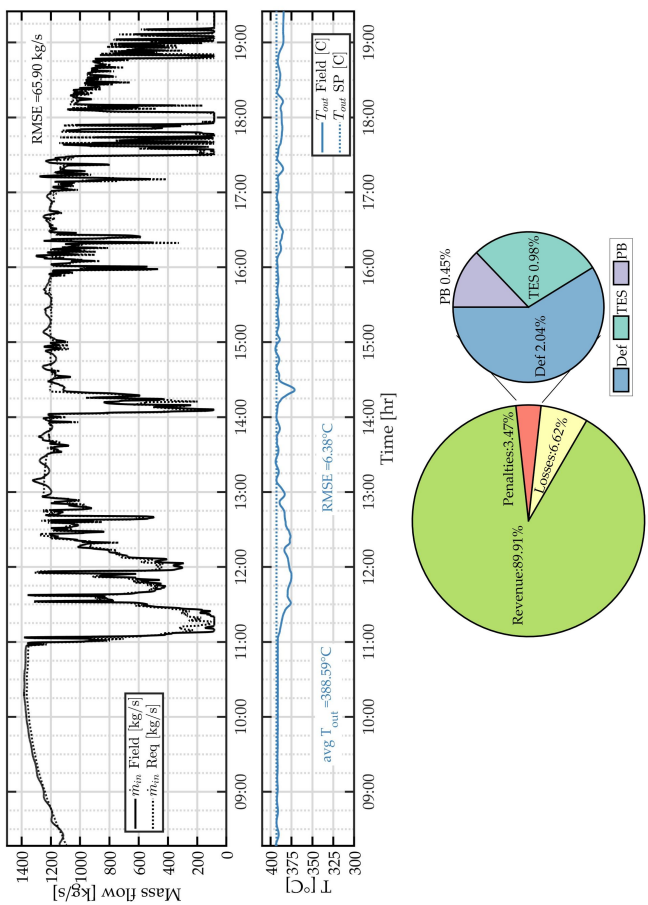

Figure F.22. Case WD3.

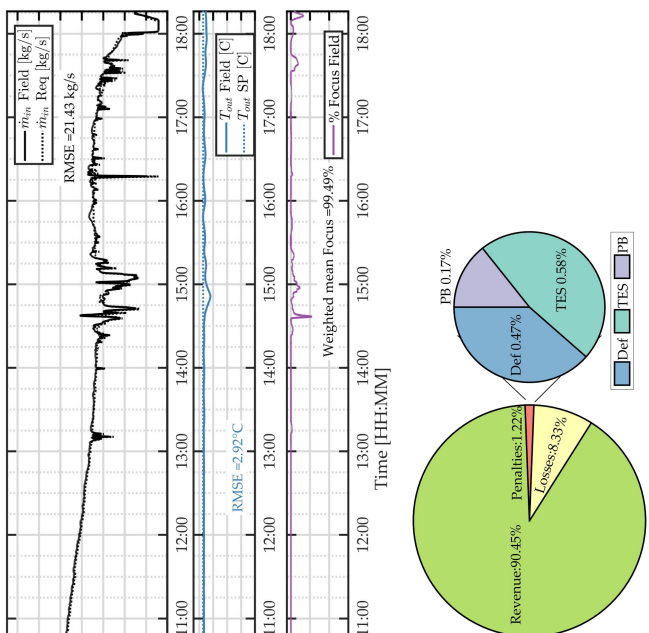

Figure F.23. Case WD4.

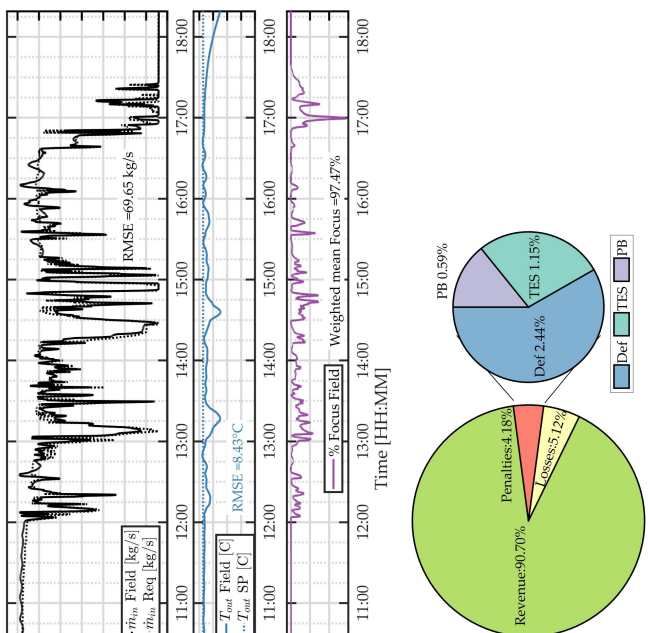

Figure F.24. Case WD5.

BIBLIOGRAPHY

[1] Abutayeh, M., Alazzam, A., and El-Khasawneh, B. "Balancing heat transfer fluid flow in solar fields". In: *Solar Energy* 105 (2014), pp. 381–389.

[2] *ACWA Power / Shanghai Power Win Dubai Solar Auction with 7.3 Cents CSP*. 2017. URL: http://www.solarpaces.org/acwa-power-shanghai-power-win-dubai-solar-auction-7-3-cents-csp/.

[3] Amaral Burghi, A. C. do. "Transient Simulation of Line-Focus Solar Thermal Power Plants". MSc thesis. European Joint Masters in Management, Engineering of Environment, and Energy (ME3), 2016.

[4] Amaral Burghi, A. C. do, Hirsch, T., and Pitz-Paal, R. "CSP Dispatch Optimization Considering Forecast Uncertainties". In: *SolarPACES*. Santiago, Chile, 2017.

[5] Anderson, J., Grundmann, R., Degrez, G., Dick, E., and Vierendeels, J. e. a. *Computational Fluid Dynamics, An Introduction*. Ed. by Wendt, J. Third Ed. Springer, 2009. ISBN: 3540850554.

[6] Barcia, L. A., Peón Menéndez, R., Martínez Esteban, J. A., José Prieto, M. A., Martín Ramos, J. A., Cos Juez, F. J. de, and Nevado Reviriego, A. "Dynamic Modeling of the Solar Field in Parabolic Trough Solar Power Plants". In: *Energies* 8.12 (2015), pp. 13361–13377. ISSN: 1996-1073. URL: http://www.mdpi.com/1996-1073/8/12/12373.

[7] Bava, F., Dragsted, J., and Furbo, S. "A numerical model to evaluate the flow distribution in a large solar collector field". In: *Solar Energy* 143 (2017), pp. 31–42. ISSN: 0038-092X. DOI: http://dx.doi.org/10.1016/j.solener.2016.12.029.

[8] Benz, N., Schulte-Fischedick, J., Dauk, J., Lüpfert, E., and Graf, W. *PARFOR - Parabolrinnenkollektoren: Feldtest, Optimierung und Weiterentwicklung von Receivern*. Tech. rep. Schott Rohrglas GmbH, 2008. DOI: 10.2314/GBV:566320517.

[9] Borutzky, W., Barnard, B., and Thoma, J. "Describing bond graph models of hydraulic components in Modelica". In: *Mathematics and Computers in Simulation* 53.4–6 (2000), pp. 381 –387. ISSN: 0378-4754. DOI: 10.1016/S0378-4754(00)00230-5. URL: http://www.sciencedirect.com/science/article/pii/S0378475400002305.

[10] Brkić, D. "Iterative Methods for Looped Network Pipeline Calculation". In: *Water Resources Management* 25.12 (2011), pp. 2951–2987. ISSN: 1573-1650. DOI: 10.1007/s11269-011-9784-3. URL: https://doi.org/10.1007/s11269-011-9784-3.

[11] Bubolz, K. “Systeme hyperbolischer partieller Differentialgleichungen: Temperaturstabilisierung in Parabolrinnensolarkraftwerken”. Diploma thesis. Department of Mathematics and Computer Science Freie Universität Berlin, 2014.

[12] Burkholder, F. and Kutscher, C. *Heat-Loss Testing of Solel's UVAC3 Parabolic Trough Receiver*. Tech. rep. NREL, 2008.

[13] Burkholder, F. and Kutscher, C. *Heat Loss Testing of Schott's 2008 PTR70 Parabolic Trough Receiver*. Tech. rep. NREL, 2009.

[14] Caldés, N. and Rodriguez-Serrano, I. “Potential Contribution of Concentrated Solar Power in Meeting the Sustainable Development Goals”. In: *SolarPACES*. Santiago, Chile, 2017.

[15] Camacho, E., Rubio, F., Berenguel, M., and Valenzuela, L. “A survey on control schemes for distributed solar collector fields. Part I: Modeling and basic control approaches”. In: *Solar Energy* 81.10 (2007), pp. 1240 –1251. ISSN: 0038-092X. DOI: https://doi.org/10.1016/j.solener.2007.01.002. URL: http://www.sciencedirect.com/science/article/pii/S0038092X07000047.

[16] Camacho, E., Rubio, F., Berenguel, M., and Valenzuela, L. “A survey on control schemes for distributed solar collector fields. Part II: Advanced control approaches”. In: *Solar Energy* 81.10 (2007), pp. 1252 –1272. ISSN: 0038-092X. DOI: https://doi.org/10.1016/j.solener.2007.01.001. URL: http://www.sciencedirect.com/science/article/pii/S0038092X07000023.

[17] Cirre, C. M., Moreno, J. C., Berenguel, M., and Guzmán, J. L. “Robust control of solar plants with distributed collectors”. In: *Proceedings of the 9th International Symposium on Dynamics and Control of Process Systems (DYCOPS 2010)*. Leuven, Belgium, 2010.

[18] Cross, H. “Analysis of Flow in Networks of Conduits or Conductors”. In: *University of Illinois Experiment Station Bulletin No. 286* (1936).

[19] Denholm, P. and Hand, M. “Grid flexibility and storage required to achieve very high penetration of variable renewable electricity”. In: *Energy Policy* 39 (2011), pp. 1817–1830. URL: https://econpapers.repec.org/article/eeeenepol/v_3a39_3ay_3a2011_3ai_3a3_3ap_3a1817-1830.htm.

[20] Dieckmann, S. *DLR - Institut of Solar Research - greenius - The Green Energy System Analysis Tool*. 2017. URL: http://www.dlr.de/sf/desktopdefault.aspx/tabid-11688/20442_read-44865/.

[21] *DOWTHERM A, Heat Transfer Fluid*. 176-1337-397 AMS. Dow. 1997. URL: http://msdssearch.dow.com/PublishedLiteratureDOWCOM/dh_0030/0901b803800303cd.pdf.

[22] Eck, M. and Hennecke, K. "Heat Transfer Fluids for Future Parabolic Trough Solar Thermal Power Plants". In: *Proceedings of ISES World Congress 2007 (Vol. I – Vol. V): Solar Energy and Human Settlement*. Ed. by Goswami, D. Y. and Zhao, Y. Berlin, Heidelberg: Springer Berlin Heidelberg, 2009, pp. 1806–1812. ISBN: 978-3-540-75997-3. DOI: 10.1007/978-3-540-75997-3_369. URL: https://doi.org/10.1007/978-3-540-75997-3_369.

[23] ESTELA. *The Value of Solar Thermal Electricity: Cost vs. Value Approach*. Tech. rep. European Solar Thermal Electricity Association, 2016. URL: http://www.estelasolar.org/Docs/2016_ESTELA_STE-CSP_Value_Final.pdf.

[24] Feldhoff, J. F. "Analysis of Once-Through Boiler Concepts in Parabolic Troughs". PhD thesis. Mechanical Engineering Department, RWTH Aachen, 2015. ISBN: 978-3-8440-4247-4.

[25] Feldhoff, J. F. and Hirsch, T. "An Approach to DNI Transients Characterization for System Evaluation". In: *AIP Conference Proceedings* 1850 (2017), p. 160007. DOI: 10.1063/1.4984541. URL: http://aip.scitation.org/doi/pdf/10.1063/1.4984541.

[26] Ferziger, J. and Perić, M. *Computational Methods for Fluid Dynamics*. Third Ed. Springer, 2002.

[27] García, I., Álvarez, J., and Blanco, D. "Performance model for parabolic trough solar thermal power plants with thermal storage: Comparison to operating plant data". In: *Solar Energy* 95 (2011), pp. 2443–2460.

[28] Genić, S., Arandjelović, I., Kolendić, P., Jarić, M., Budimir, N., and Genić, V. "A Review of Explicit Approximations of Colebrook's Equation". In: *FME Transactions* 39 (2011), pp. 67–71. URL: http://www.mas.bg.ac.rs/istrazivanje/fme/vol39.

[29] Gielen, H. Personal communication in July, 2017. Control Systems Engineer, TSK-Flagsol GmbH.

[30] Giostri, A. "Transient effects in linear concentrating solar thermal power plant". PhD thesis. Energy Department, Politecnico Di Milano, 2012.

[31] Herrán-González, A., Cruz, J. D. L., Andrés-Toro, B. D., and Risco-Martín, J. "Modeling and simulation of a gas distribution pipeline network". In: *Applied Mathematical Modelling* 33.3 (2009), pp. 1584 –1600. ISSN: 0307-904X. DOI: https://doi.org/10.1016/j.apm.2008.02.012. URL: http://www.sciencedirect.com/science/article/pii/S0307904X08000607.

[32] Herty, M. and Seaïd, M. "Simulation of transient gas flow at pipe-to-pipe intersections". In: *Int. J. Numer. Meth. Fluids* 56 (2008), pp. 485–506. DOI: 10.1002/fld.1531.

[33] Hirsch, T. "Dynamische Systemsimulation und Auslegung des Abscheidesystems für die solare Direktverdampfung in Parabolrinnenkollektoren". PhD thesis. Institut für Thermodynamik und Wärmetechnik, Universität Stuttgart, 2005. ISBN: 3-18-353506-8.

[34] Hirsch, T. *SolarPACES Guideline for Bankable STE Yield Assessment*. Tech. rep. SolarPACES, 2017. URL: http://www.solarpaces.org/csp-research-tasks/task-annexes-iea/task-i-solar-thermal-electric-systems/solarpaces-guideline-for-bankable-ste-yield-assessment/.

[35] Hirsch, T. and Schenk, H. "Dynamics of oil-based parabolic trough plants – A detailed transient simulation model". In: *SolarPACES*. Perpignan, France, 2010.

[36] Hirsch, T., Janicka, J., Löw, T., Metzger, C., and Pawellek, R. "Annual Simulations with the Ebsilon Professional time series calculation module". In: *SolarPACES*. Perpignan, France, 2010.

[37] Incorpera, F. and DeWitt, D. *Fundamentals of Heat and Mass Transfer*. Fourth Ed. John Wiley & Sons, 1996. ISBN: 0471304603.

[38] IRENA. *Adapting market design to high shares of variable renewable energy*. Tech. rep. International Renewable Energy Agency, Abu Dhabi, 2017. URL: http://www.irena.org/-/media/Files/IRENA/Agency/Publication/2017/May/IRENA_Adapting_Market_Design_VRE_2017.pdf.

[39] Janotte, N. "Requirements for Representative Acceptance Tests for the Prediction of the Annual Yield of Parabolic Trough Solar Fields". PhD thesis. Mechanical Engineering Department, RWTH Aachen, 2012. ISBN: 978-3-8440-1565-2.

[40] Jung, C., Dersch, J., Nietsch, A., and Senholdt, M. "Technological Perspectives of Silicone Heat Transfer Fluids for Concentrated Solar Power". In: *Energy Procedia* 69.Supplement C (2015). International Conference on Concentrating Solar Power and Chemical Energy Systems, SolarPACES 2014, pp. 663 –671. ISSN: 1876-6102. DOI: https://doi.org/10.1016/j.egypro.2015.03.076. URL: http://www.sciencedirect.com/science/article/pii/S1876610215003823.

[41] Kalogirou, S. *Solar Energy Engineering: Processes and Systems*. Second Ed. Academic Press, 2013. ISBN: 9780123972569.

[42] Kays, W., Crawford, M., and Weigand, B. *Convective Heat and Mass Transfer*. Fourth Ed. McGraw-Hill, 2005.

[43] Koch, S., Hirsch, T., and Eck, M. "Modelling and control of a solar-thermal parabolic trough DSG superheater with several parallel rows and central steam separation". In: *Energy Sustainability (ES2007)*. Ed. by ASME. 2007. URL: http://elib.dlr.de/51034/.

[44] Kuehn, T. and Goldstein, R. "Correlating Equations for Natural Convection Heat Transfer Between Horizontal Circular Cylinders". In: *International Journal of Heat Mass Transfer* 19 (1976), pp. 1127–1134.

[45] Kuhn, P. et al. "Shadow camera system for the generation of solar irradiance maps". In: *Solar Energy* 157.Supplement C (2017), pp. 157 –170. ISSN: 0038-092X. DOI: https://doi.org/10.1016/j.solener.2017.05.074. URL: http://www.sciencedirect.com/science/article/pii/S0038092X17304814.

[46] Kuhn, P., Wilbert, S., Prahl, C., Kazantzidis, A., Ramirez, L., Zarzalejo, L., Vuilleumier, L., Blanc, P., and Pitz-Paal, R. "Validation of nowcasted spatial DNI maps". In: *DNICast Direct Normal Irradiance Nowcasting methods for optimized operation of concentrating solar technologies*. 2017. URL: http://www.sidosoft.com/dnicast/www/documents/D4.1%20Validation%20of%20nowcasted%20spatial%20DNI%20maps.pdf.

[47] Kuhn, P. et al. "Validation of an all-sky imager based nowcasting system for industrial PV plants". In: *EUPVSEC conference proceedings* (2017). Accepted for publication.

[48] Kuhn, P. et al. "Validation of spatially resolved all sky imager derived DNI nowcasts". In: *AIP Conference Proceedings* 1850.1 (2017), p. 140014. DOI: 10.1063/1.4984522. eprint: http://aip.scitation.org/doi/pdf/10.1063/1.4984522. URL: http://aip.scitation.org/doi/abs/10.1063/1.4984522.

[49] Kurup, P. and Turchi, C. "Potential for solar industrial process heat in the United States: A look at California". In: *AIP Conference Proceedings* 1734 (2016), p. 110001. DOI: https://doi.org/10.1063/1.4949198. URL: http://aip.scitation.org/doi/pdf/10.1063/1.4949198.

[50] Lilliestam, J. et al. "Policies to Keep and Expand the Option of Concentrating Solar Power for Dispatchable Renewable Electricity". In: *SolarPACES*. Santiago, Chile, 2017.

[51] Lüpfert, E. *PARFOR - Testreport PTR Parabolic Trough Receiver 2005 - Modelling Parameters from Test Results*. Tech. rep. German Aerospace Centre (DLR), 2005.

[52] Maranzana, G., Perry, I., and Maillet, D. "Mini- and micro-channels: influence of axial conduction in the walls". In: *International Journal of Heat and Mass Transfer* 47 (2004), pp. 3993–4004.

[53] Mikami, M., Odawara, O., and Kawamura, K. "Sound velocity in heat transfer salt (mixture of molten sodium nitrate-potassium nitrate-sodium nitrite, 7/44/49 mol %) studied by an ultrasonic pulse-echo method". In: *Journal of Chemical & Engineering Data* 26.4 (1981), pp. 411–413. DOI: 10.1021/je00026a019. eprint: http://dx.doi.org/10.1021/je00026a019. URL: http://dx.doi.org/10.1021/je00026a019.

[54] *MinWool-1200®*. IND-401 02-17. JohnsManville. 2017. URL: http://www.jm.com/content/dam/jm/global/en/industrial-insulation/Industrial\%20Documents/IND-401-MinWool-1200-Pipe.pdf.

[55] Moreno-Tejera, S., Silva-Pérez, M., Ramírez-Santigosa, L., and Lillo-Bravo, I. "Classification of days according to DNI profiles using clustering techniques". In: *Solar Energy* 146.Supplement C (2017), pp. 319 –333. ISSN: 0038-092X. DOI: https://doi.org/10.1016/j.solener.2017.02.031. URL: http://www.sciencedirect.com/science/article/pii/S0038092X1730124X.

[56] Müller, S., Sirch, T., and Schroedter-Homscheidt, M. "Report on comparison of satellite-based nowcasting methods". In: *DNICast Direct Normal Irradiance Nowcasting methods for optimized operation of concentrating solar technologies*. 2017. URL: http://www.dnicast-project.net/documents/D3.8%20Report%20on%20comparison%20of%20satellite-based%20nowcasting%20methods.pdf.

[57] Noureldin, K., Hirsch, T., and Pitz-Paal, R. "Virtual Solar Field - Validation of a detailed transient simulation tool for line focus STE fields with single phase heat transfer fluid". In: *Solar Energy* 146 (2017), pp. 131 –140. ISSN: 0038-092X. DOI: http://dx.doi.org/10.1016/j.solener.2017.02.028. URL: http://www.sciencedirect.com/science/article/pii/S0038092X17301226.

[58] Noureldin, K., González-Escalada, L. M., Hirsch, T., Nouri, B., and Pitz-Paal, R. "Modelling and optimization of transient processes in line focusing power plants with single-phase heat transfer medium". In: *AIP Conference Proceedings* 1734.1, 070022 (2016). DOI: 10.1063/1.4949169. URL: http://scitation.aip.org/content/aip/proceeding/aipcp/10.1063/1.4949169.

[59] Noureldin, K., Hirsch, T., and Pitz-Paal, R. "Virtual solar field - An opportunity to optimize transient processes in line-focus CSP power plants". In: *AIP Conference Proceedings* 1850.1 (2017), p. 160019. DOI: 10.1063/1.4984553. eprint: http://aip.scitation.org/doi/pdf/10.1063/1.4984553. URL: http://aip.scitation.org/doi/abs/10.1063/1.4984553.

[60] Noureldin, K., Hirsch, T., Kuhn, P., Nouri, B., Yasser, Z., and Pitz-Paal, R. "Modelling an Automatic Controller for Parabolic Trough Solar Fields under Realistic Weather Conditions". In: *SolarPACES*. Santiago, Chile, 2017.

[61] Noureldin, K., Hirsch, T., Nouri, B., Yasser, Z., and Pitz-Paal, R. "Evaluating the potential benefit of using nowcasting systems to improve the yield of parabolic trough power plants with single-phase HTF". In: *submitted for publication* (2019).

[62] Nouri, B., Kuhn, P., Wilbert, S., Prahl, C., Pitz-Paal, R., Blanc, P., Schmidt, T., Yasser, Z., Santigosa, L. R., and Heineman, D. "Nowcasting of DNI maps for the solar field based on voxel carving and individual 3D cloud objects from all sky images". In: *SolarPACES*. Santiago, Chile, 2017.

[63] NREL, ed. *Concentrating Solar Power Projects, La Africana*. 2012. URL: https://www.nrel.gov/csp/solarpaces/project_detail.cfm/projectID=236.

[64] NREL, ed. *Concentrating Solar Power Projects, Andasol 3*. 2013. URL: http://www.nrel.gov/csp/solarpaces/project_detail.cfm/projectID=117.

[65] Olano, X., Jalón, A. G. de, Pérez, D., Barberena, J. G., López, J., and Gastón, M. "Outcomes and Features of the Inspection of Receiver Tubes (ITR) System for Improved O&M in Parabolic Trough Plants". In: *SolarPACES*. Santiago, Chile, 2017.

[66] Padilla, R. V., Demirkaya, G., Goswami, D. Y., Stefanakos, E., and Rahman, M. M. "Heat transfer analysis of parabolic trough solar receiver". In: *Applied Energy* 88 (2011), pp. 5097–5110. DOI: 10.1016/j.apenergy.2011.07.012.

[67] Parte, M. P. del la, Cirre, C. M., Camacho, E. F., and Berenguel, M. "Application of Predictive Sliding Mode Controllers to a Solar Plant". In: *IEEE TRANSACTIONS ON CONTROL SYSTEMS TECHNOLOGY* 16.4 (2008), pp. 819–825.

[68] Pitz-Paal, R. "Concentrating solar power: Still small but learning fast". In: *Nature Energy* 2.17095 (2017). ISSN: 2058-7546. DOI: 10.1038/nenergy.2017.95.

[69] Platzer, W. J. "Combined solar thermal and photovoltaic power plants – An approach to 24h solar electricity?" In: *AIP Conference Proceedings* 1734.1, 070026 (2016). DOI: 10.1063/1.4949173. URL: http://scitation.aip.org/content/aip/proceeding/aipcp/10.1063/1.4949173.

[70] Profos, P. *Die Regelung von Dampfanlagen*. First Ed. Springer-Verlag Berlin Heidelberg, 1962. ISBN: 978-3-642-50977-3. DOI: 10.1007/978-3-642-50976-6.

[71] Reader-Harris, M. *Orifice Plates and Venturi Tubes*. First Ed. Experimental Fluid Mechanics. Springer International Publishing, 2015. ISBN: 978-3-319-35943-4. DOI: 10.1007/978-3-319-16880-7.

[72] REN21. *Renewables 2017 Global Status Report*. Tech. rep. Paris: REN21 Secretariat, 2017. URL: http://www.ren21.net/gsr-2017/.

[73] Sanderson, C. and Curtin, R. "Armadillo: a template-based C++ library for linear algebra". In: *Journal of Open Source Software* 1 (2016), p. 26.

[74] SCHOTT. *SCHOTT PTR®70 Receiver*. 2013. URL: http://www.schott.com/d/csp/2ad9cb93-5b86-4a51-aead-a49b4e869ef8/1.0/schott_ptr70_4th_generation_datasheet.pdf.

[75] Schwarzbözl, P., Gross, V., Quaschnig, V., and Ahlbrink, N. "a low-cost dynamic shadow detection system for site evaluation". In: *17th SolarPACES 2011 Conference*. 2011. URL: http://elib.dlr.de/83596/.

[76] Shinskey, F. *Process Control Systems: Application, Design, and Tuning*. Chemical engineering books. McGraw-Hill, 1996. ISBN: 9780070571013. URL: https://books.google.de/books?id=EqdTAAAAMAAJ.

[77] Siegel, N. P., Bradshaw, R. W., Cordaro, J. B., and Kruizenga, A. M. "Thermophysical Property Measurement of Nitrate Salt Heat Transfer Fluids". In: *International Conference on Energy Sustainability, Parts A, B, and C*. Vol. 54686. ASME, 2011. URL: http://dx.doi.org/10.1115/ES2011-54058.

[78] SolarPACES, ed. *Bokpoort Breaks A Solar Thermal Energy Production Record*. 2017. URL: http://www.solarpaces.org/bokpoort-breaks-solar-thermal-energy-production-record/.

[79] Struttura Informatica, ed. *Dynamic Process Modelling*. 2016. URL: http://www.strutturainformatica.it/dpm/.

[80] Swamee, P. K. and Sharma, A. K. *Design of Water Supply Pipe Networks*. First Ed. Wiley-Interscience, 2008.

[81] Tannehill, J., Anderson, D., and Pletcher, R. *Computational Fluid Mechanics and Heat Transfer*. Second Ed. Series in Computational and Physical Processes in Mechanics and Thermal Sciences. Taylor & Francis, 1997. ISBN: 9781560320463.

[82] *Therminol VP-1*. Technical Bulletin 7239115B. Solutia. 1999. URL: https://www.sintelub.com/files/therminol_vp1.pdf.

[83] *Thermo-12®Gold*. IND-300 12-16. JohnsManville. 2016. URL: http://www.jm.com/content/dam/jm/global/en/industrial-insulation/Industrial\%20Documents/IND-300-Thermo-12-Gold.pdf.

[84] VDI. *VDI Heat Atlas*. Second Ed. Berlin Heidelberg: Springer, 2010.

[85] Wagner, P. H. and Wittmann, M. "Influence of different operation strategies on transient solar thermal power plant simulation models with molten salt as heat transfer fluid". In: *SolarPACES*. Las Vegas, USA, 2013.

[86] White, F. *Fluid Mechanics*. Sixth Ed. McGraw-Hill, 2009.

[87] Wilbert, S. et al. "Wolkenkamera-basierte Kürzestfristvorhersage der Direktstrahlung". In: *19. Kölner Sonnenkolloquium*. Cologne, Germany, 2016.

[88] Winterbone, D. E. and Turan, A. *Advanced Thermodynamics for Engineers*. Second Ed. Butterworth-Heinemann, 2015. ISBN: 978-0-444-63373-6. DOI: 10.1016/B978-0-444-63373-6.01001-7.

[89] Wittmann, M., Hirsch, T., and Eck, M. "Some Aspects of Parabolic Trough Field Operation with Oil as a Heat Transfer Fluid". In: *SolarPACES*. Berlin, Germany, 2009.

[90] *World Energy System Not On Track to Meet Paris Agreement Goals*. 2017. URL: http://newsroom.unfccc.int/unfccc-newsroom/world-energy-system-not-on-track-to-meet-paris-agreement-goals/.

[91] Xactex Corporation. *Accoustic Properties for Liquids*. 2017. URL: https://www.nde-ed.org/GeneralResources/MaterialProperties/UT/ut_matlprop_liquids.htm.

[92] Zaversky, F. "Object-oriented modeling for the transient performance simulation of solar thermal power plants using parabolic trough collectors - A review and proposal of modeling approaches for thermal energy storage". PhD thesis. Mechanical Engineering Department, Public University of Navarre, 2014.

[93] Zaversky, F., Medina, R., García-Barberena, J., Sánchez, M., and Astrain, D. "Object-oriented modelling for transient performance simulation of parabolic trough collectors using molten salt as heat transfer fluid". In: *Solar Energy* 95 (2013), pp. 192–215.

[94] Zavoico, A. *Solar Power Tower Design Basis Document*. Tech. rep. Sandia, 2001.

[95] Zunft, S. "Temperature control of a distributed collector field". In: *Solar Energy* 55.4 (1995), pp. 321 –325. ISSN: 0038-092X. DOI: http://dx.doi.org/10.1016/0038-092X(95)00055-V. URL: http://www.sciencedirect.com/science/article/pii/0038092X9500055V.

[96] Zunft, S. *Dynamik und Regelung von Solarkollektorfeldern zur Prozeßwärme- und Stromerzeugung*. Fortschritt Berichte Energieerzeugung. VDI-Verlag Stuttgart, 2003. ISBN: 978-3-18-350506-7.